A study on the Atmospheric Boundary Layer in the High Arctic during winter

Author:
Andreas Frøyland

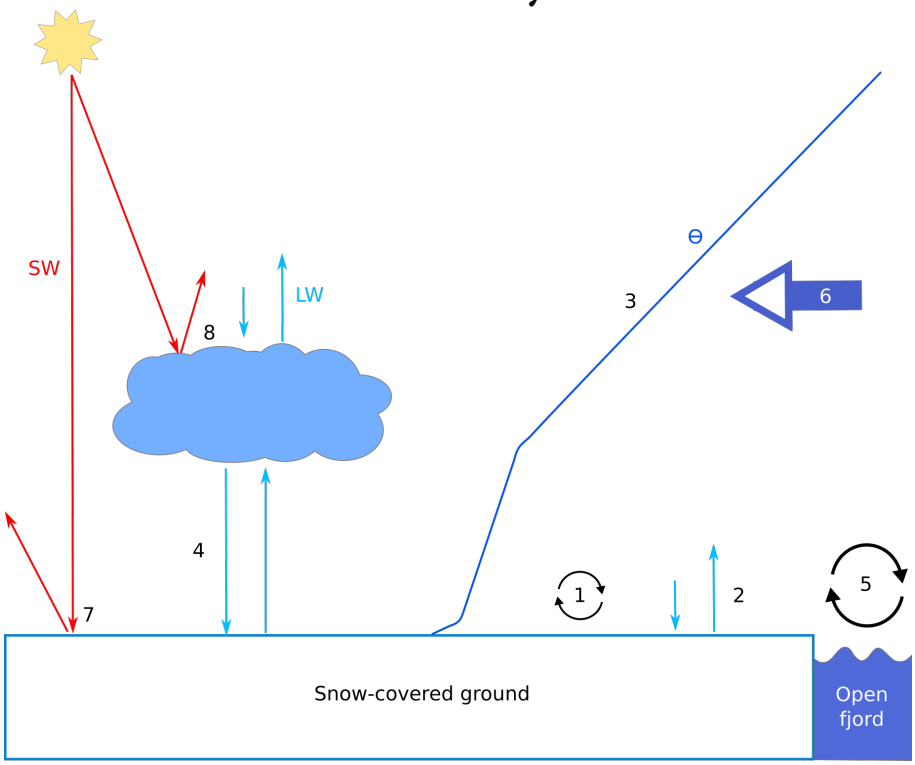

Master thesis in Meteorology
Supervised by:
Dr. Joachim Reuder
Stephan Kral

UNIVERSITY OF BERGEN
GEOPHYSICAL INSTITUTE

August 2016

Abstract

We investigated the stable boundary layer in Adventdalen by measuring meteorological parameters with Sonic anemometers at two heights, as well as slow response measurements, during a 7 week measurement campaign from February to April 2014. The main drivers of the stability in Adventdalen was found to be the wind speed, the wind direction and the net radiation. Calm conditions with weak SE wind and strong negative net radiations were favorable to get very stable conditions. Such very stable conditions, however, very rarely occurred as the measurement period was characterized by exceptionally mild conditions.

Classic MOST represented the fluxes better than MOST using local scales, at least up to $\zeta \approx 0.3$. The downward heat flux maxima is found at $\zeta \approx 0.01$, but it is not found to be a good threshold for the transition regime. This could be caused by the lack of observations at higher levels. We found that the Coriolis force had an insignificant influence to the turbulence.

The non-dimensional profiles were highly influenced by the choice of vertical gradients, but we found the wind profile to be estimated best using a logarithmic fit to the data. The universal function ϕ_h^{G07} represented the calculated non-dimensional temperature profile well, at all stabilities, while ϕ_m^{G07} only represented our calculated non-dimensional momentum profile adequately up to $\zeta \approx 0.2$.

Acknowledgements

I would like to thank my supervisor Dr. Joachim Reuder for the guidance and feedback in writing this thesis, and my co-supervisor Stephan Kral for a lot of help and feedback throughout the last year.

I would like to give a special thanks to the experimental meteorology group at the Geophysical Institute for helpful feedback and discussions, with a special thanks to Valerie Kumer in the help of the development of an averaging routine used in this thesis.

A thanks to my family for their love and support during this year, and a special thanks to my father Lars Andreas Frøyland, for proof reading towards the end.

And last, but not least, I would like to thank my fellow students at GFI for five amazing years, that I will never forget!

Contents

1 Introduction

Stable boundary layer (SBL) turbulence processes are still not well known, particularly under very stable conditions, resulting in e.g. inappropriately poor parameterizations in numerical weather prediction (NWP) and climate models. (e.g. *Walesby and Beare*, 2016; *Atlaskin and Vihma*, 2012; *Vihma et al.*, 2014; *Svensson and Rutgersson*, 2016). As the Arctic atmospheric boundary layer (ABL) typically has a stable stratification for the whole winter, and parts of the autumn and spring season (*Persson*, 2002), SBL research is of huge importance for the improvement with respect to the corresponding modeling capabilities.

Because of the importance of the smaller scales of turbulence, in particular for stable conditions, turbulence is not satisfactory resolved in the models, and needs to be parameterized. This causes climate and NWP models to have considerable uncertainties in the description of turbulent exchange (e.g. *Vihma et al.*, 2014). *Tjernström et al.* (2005) found heat fluxes from climate models to be unreliable with insignificant correlations to the measurements from the SHEBA campaign, and *Esau and Zilitinkevich* (2010) found that climate models overestimate the height of the Arctic ABL, and therefore also the turbulent mixing. The poor representation of turbulence in the ABL causes a warm temperature bias in models (*Holtslag et al.*, 2013), which can have a huge impact on the prediction of future climate scenarios. Little is know about the quality of operational weather forecast in the central Arctic (*Vihma et al.*, 2014), but *Mayer et al.* (2012) also found a temperature bias at times exceeding 10°C for Adventdalen using the the Weather Reasearch and Forecast model (WRF). The parameterizations typically used in the models are often based on observations from low- and mid latitude (*Vihma et al.*, 2014). Arctic observations and analysis of available data sets is therefore essential in order to improve prediction skills in Arctic regions (e.g. *Tastula et al.*, 2015; *Vihma et al.*, 2014).

Monin Obukhov similarity theory (MOST) is still the most commonly used theoretical framework for the description of turbulent exchange close to the ground, developed by *Monin and Obukhov* (1954). It relates the different turbulent fluxes to their respective vertical non-dimensional profiles. Its applicability is limited to the surface layer (lowest 10% of the ABL), as it assumes constant fluxes with height. MOST works good for a wide range of stabilities, but fails for very stable conditions. *Nieuwstadt*

(1984) extended MOST for more stable conditions by the use of local scales. For very stable conditions it will still fail, as e.g. the Coriolis force becomes significant, creating flow patterns resembling an Ekman spiral. Sporadic and intermittent turbulence can still exist even for extremely stable conditions, and the layer will not be laminar on the average (*Grachev et al.*, 2005). *Mahrt et al.* (1998) and *Grachev et al.* (2005) have divided into different stability regimes, with defined limits of the applicability of MOST, both in the classical sense and for local scales, based on observations from the SHEBA campaign. Empirical predictions of the non-dimensional profiles have been developed, but previous versions were not based on Arctic observations (e.g. *Högström*, 1988, 1996). *Grachev et al.* (2007) derived new empirical non-dimensional profiles based on the SHEBA data, better suited for stable conditions.

Zilitinkevich and Calanca (2000) proposed an advanced non-local stability theory for the surface layer, taking into account the effect of the static stability in the SBL. It was extended by classifying for different wind and temperature gradients by *Sodemann and Foken* (2004), but they found that different weather conditions significantly altered the gradients, and that this later needed to be taken into account. *Zilitinkevich and Esau* (2007) developed it further by taking into account non-local effects, and effects of Coriolis.

Sorbjan and Grachev (2010) have also proposed an alternative similarity approach, which is equivalent to MOST, but using gradients as the basis for the scaling parameters instead of the fluxes. These similarity functions are unaffected by self-correlation, which is the case for MOST. Common for both is that the similarities are based on idealized and homogeneous surfaces (sea-ice, etc), and orographic effects in inhomogeneous terrain may limit the applicability of similarity theories (*Mäkiranta et al.*, 2011).

In this thesis we will try to find the main drivers of the stability in Adventdalen, and find which conditions are causing the most stable and unstable stratification. As SHEBA is one of the biggest and most comprehensive campaigns on stable boundary layers, we will compare our results with some of their findings. We will check the validity of classic MOST, and the extension of the local stability parameter z Λ^{-1}, and compare with articles based on the SHEBA data (e.g *Grachev et al.*, 2005, 2013), and other SBL research.

In Chapter 2 we take a look at the background, Chapter 3 describes the study site, the data collected and the instruments used. Chapter 4 describes the methods applied. The results and discussion are then presented in the following chapters: Chapter 5 introduces the stability distribution during the campaign, and the main mechanisms influencing the stability. Chapter 6 presents the impact of scaling in MOST on the heat and momentum flux, and Chapter 7 does the same for the non-dimensional gradients. A summary and outlook is given in Chapter 8.

2 Background

In this chapter we will briefly go trough the basics of turbulence (Section 2.1), the atmospheric boundary layer (Section 2.2) including the stably stratified ABL, and the SHEBA-campaign is presented (Section 2.4).

2.1 Atmospheric turbulence

Turbulence consists of irregular swirls of motion, called eddies. They are generated by heating, and the following rising air (thermals), and by wind shear. In the atmospheric boundary layer, this wind shear is mainly caused by friction at the surface, but other processes creating differences in wind with height will also generate wind shear.

We can describe the turbulence as motion around a mean state, that is both irregular and stochastic (e.g. *Foken*, 2008). These eddies cover a wide range of temporal and spatial scales; from seconds to days, and from centimeters to thousands of kilometers, respectively (e.g. *Foken*, 2008). The energy is transported in a cascade from the energy containing larger eddies to smaller eddies, until the energy is dissipated by molecular diffusion. This is a process that can be described as highly chaotic. The largest eddies have the size of the atmospheric boundary layer in case of buoyancy driven turbulence, and have a size corresponding to the depth of the shear layer for mechanically driven turbulence.

Because these eddies can occur on very small scales, it is virtually impossible to deterministically describe and forecast a single eddy (*Stull*, 1988). To deal with this, we can introduce stochastic methods, that are based on the average statistical behavior of the eddies. This method uses covariances to explain the relationship between different variables, in the form of $\overline{w'T'}$, $\overline{w'q'}$ or $\overline{u'w'}$, for temperature, humidity and momentum, respectively, where the bar denotes a time average and the prime the turbulent deviation from its average. These covariances are representing the kinematic fluxes of heat (sensible heat), moisture (latent heat) and momentum. During summer, the surface will be warmed by radiative heating from the sun, which again warms air close to the surface. Warm air rises, and will bring relatively warm air up, meaning that w' and T' are positive. At the same time as relatively cold air sinks, meaning w' and T' are negative. When averaged, the covariance will always be positive, which means that heat

is transported upwards, and there is a positive kinematic heat flux. These properties are used when defining the governing equations for the sensible heat flux (H_s) and the latent heat flux (H_L) are (e.g. *Foken*, 2008):

$$H_s = \rho c_p \overline{w'T'} \tag{2.1}$$

$$H_L = \rho \lambda \overline{w'q'} \tag{2.2}$$

where ρ is the density of air, c_p is the specific heat of air at constant pressure, λ is the evaporation heat of water, and $\overline{w'T'}$ and $\overline{w'q'}$ the kinematic flux for heat and moisture, respectively (e.g. *Foken*, 2008). The momentum flux, which is called the Reynolds stress is (e.g *Stull*, 1988):

$$\tau_{\text{Reynolds, xz}} = -\rho \overline{u'w'_s} \tag{2.3}$$

$$\tau_{\text{Reynolds, yz}} = -\rho \overline{v'w'_s} \tag{2.4}$$

where $\overline{u'w'_s}$ and $\overline{v'w'_s}$ are the covariances of the horizontal and vertical wind where the subscript s denotes surface values. This gives the total Reynolds stress as:

$$\left|\tau_{\text{Reynolds}}\right| = \left[\tau^2_{\text{Reynolds, xz}} + \tau^2_{\text{Reynolds, yz}}\right]^{1/2} \tag{2.5}$$

The friction velocity, which is the common scaling parameter for turbulence generated by wind shear near the ground (e.g. *Stull*, 1988) is defined as:

$$u_*^2 = \left[\overline{u'w'_s}^2 + \overline{v'w'_s}^2\right]^{1/2} \tag{2.6}$$

giving the relationship

$$|\tau_{\text{Reynolds}}| = \rho u_*^2 \tag{2.7}$$

where ρ denotes the mean density of the surrounding air. These different kinematic fluxes can be measured directly with a sonic anemometer, as long as the averaging intervals are long enough. This measurement principle is called the eddy-covariance method. For sensors mounted at 2-5 meters, which is our case, an averaging interval of 30-minutes is often sufficient (e.g. *Foken*, 2008).

An other approach is to use different similarity theories, that takes advantage of the common behavior of empirically observed phenomena (e.g. *Stull*, 1988), e.g. Monin-Obukhov similarity theory which will be described in section 2.3. The use of numerical solutions to the equation of motion could be an approach to determine and forecast the turbulence in the atmosphere, like we do on larger scales. Unfortunately, when dealing with the turbulent parameters, it is not a closed system, meaning we have

more unknowns than equations (e.g *Stull*, 1988). Turbulence closure is applied in order to close the system, and be able to approximate the turbulence. One of the simplest methods, which is a first order closure technique, is K-theory. Here the kinematic fluxes ($\overline{w'T'}$, $\overline{w'q'}$ and $\overline{w'v'}$) are described by the gradient at one point, and an eddy diffusivity parameter:

$$\overline{w'T'} = -K_H \frac{\partial T}{\partial z} \tag{2.8}$$

$$\overline{w'q'} = -K_E \frac{\partial q}{\partial z} \tag{2.9}$$

$$\overline{w'v'} = K_m \frac{\partial v}{\partial z} \tag{2.10}$$

where K_H and K_E are eddy diffusivity parameters for heat and moisture and K_m the one for moisture, often called eddy viscosity. These coefficients depend on wind speed, stratification and surface properties (e.g. *Foken*, 2008). Equation 2.8-2.10 can approximate the heat, moisture and momentum fluxes in Equation 2.1-2.6.

The reason why turbulence is important is because it transports heat, momentum, moisture, and other quantities, through turbulent mixing. It is a magnitude of 10^5 more effective in the transport of different quantities like heat and momentum compared to molecular diffusion, meaning turbulence is an important transport (mixing) process, particularly in the atmospheric boundary layer (e.g. *Foken*, 2008), which will be described in the following section.

2.2 The atmospheric boundary layer

The atmospheric boundary layer (ABL), or the planetary boundary layer which it is sometimes referred to, is the lowest part of the troposphere. In this region the wind speed is typically significantly lower than its correspondent geostrophic value, including a counter-clockwise directional change of up to 30-40° (e.g. *Stull*, 1988). This happens because the ABL is directly influenced by surface forcing, on a timescale of one hour (e.g. *Stull*, 1988). Surface forcing includes frictional drag, transport of heat and moisture, and changes on the wind flow due to the terrain. The surface drag reduces the wind towards the surface, until the roughness length z_0 where there is no longer any wind, causing a near-logarithmic wind profile in the surface layer (e.g. *Stull*, 1988). Over the ABL there is a layer of strong statical stability. Figure 2.1 illustrate the processes influencing the Arctic ABL, which is our focus in this thesis.

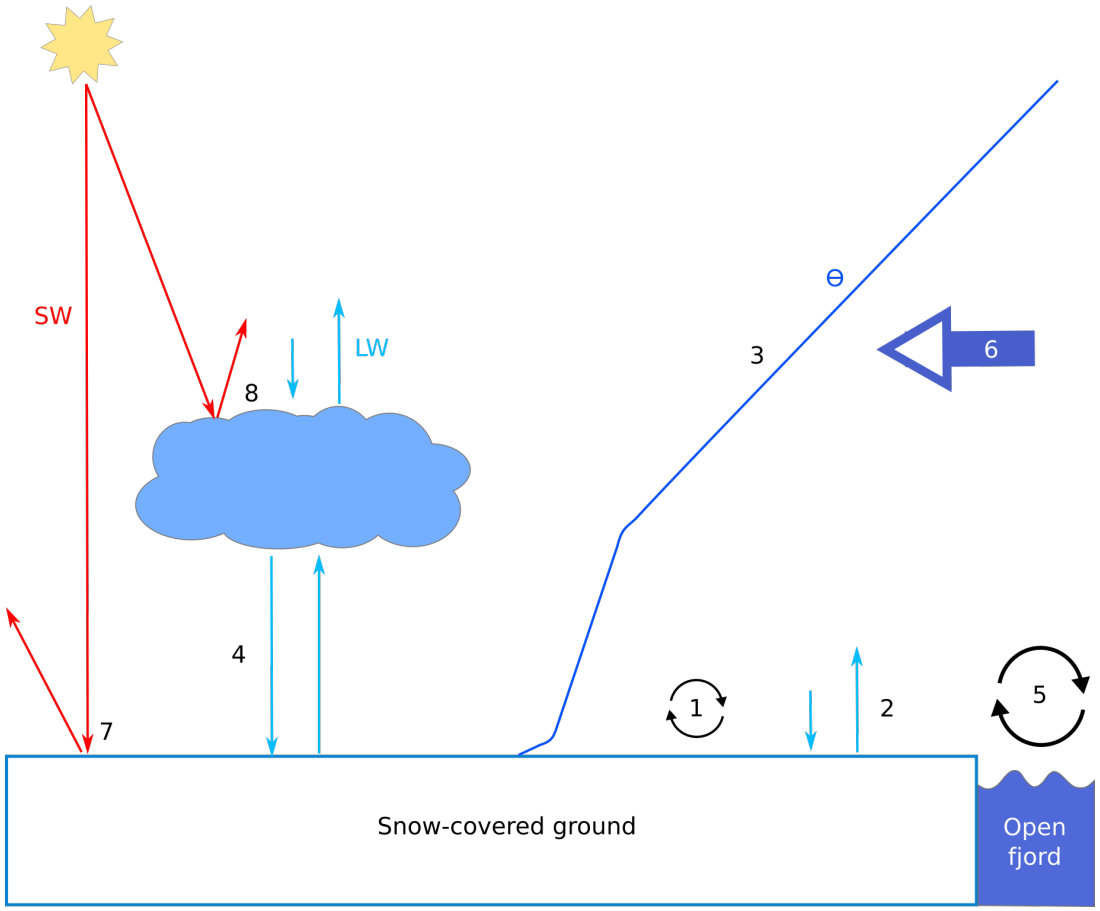

Figure 2.1: Illustration of the processes influencing the arctic atmospheric boundary layer: (1) Stable boundary layer turbulence in a cloud free environment; (2) Absorbed and emitted longwave radiation in a cloud free environment; (3) Vertical structure of potential temperature under cloud-free and statically stable conditions. (The shape of the profile resembles measurements from Adventdalen made in 2009 by *Mayer et al.*, 2012); (4) Absorbed and emitted longwave radiation in the presence of cloud; (5) Convection of heat and moisture over open water; (6) Advection of heat and moisture from lower latitudes; (7) Absorbed and reflected solar radiation, dependent on the surface albedo and terrain heteorogeneieties; (8) Reflection of solar radiation and emission of longwave radiation caused by clouds.

Stable boundary layer

A distinct feature of the Arctic ABL is that for most of the winter and spring it is stably stratified, hereby called a stable boundary layer (SBL). In lower latitudes the SBL is mostly connected to diurnal variations in the net radiation budget. A positive radiation balance leads to an unstable atmosphere during the day, while at night a negative radiation balance causes a SBL to develop (*Foken*, 2008). This negative radiation balance most often happen at a near-cloudless night, since there is no clouds to absorb and emit the outgoing longwave radiation (Figure 2.1 [2]), causing temperature inversions (Figure 2.1 [3]). In Arctic regions, this negative radiation balance can persist for longer periods of time, especially during winter and spring. This leads the Arctic SBL to last for a long time period, and not only during night as in lower latitudes. Clouds are particularly important, since during the presence of clouds longwave radiation is absorbed by the cloud and then emitted from the cloud base towards the surface,

which counteracts the negative radiation balance (Figure 2.1[4]).

A SBL will strongly dampen turbulence (e.g. *Foken*, 2008), since vertical motion is suppressed by the stability (Figure 2.1 [1]). This leaves mechanically induced shear to be the main source of mixing during stable conditions. On top of stable boundary layers a low level jet frequently occurs. Depending on the vertical extension of the SBL, the corresponding wind maximum is, for the Arctic, typically located at heights between 10 and 300 meters above ground (e.g. *Foken*, 2008). The vertical wind shear induced by the low level jet generates turbulence which leads to vertical mixing from the low level jet and down to the SBL underneath (*Jakobson et al.*, 2013), which periodically can mix the whole SBL, and therefore lead to a neutrally stratified ABL.

Constant-flux layer

The Prandtl layer, or the constant-flux layer, is assumed to cover approximately the lowest 10% of the ABL. This is a layer where the fluxes are assumed to be constant with height. It is typically several of tens to a few hundred meters deep under unstable conditions, while under stable conditions it could be as shallow as a couple of meters (e.g. *Foken*, 2008).

2.3 Monin-Obukhov similarity theory

Monin-Obukhov similarity theory (MOST), or surface based similarity assumes that the fluxes vary with less than 10% of their magnitude with height (e.g. *Stull*, 1988), which means we have a constant-flux layer (Section 2.2). This means that we can use the quantities at one height to describe the surface layer. It is based on the assumption that the boundary layer has a logarithmic wind profile. Before *Monin and Obukhov* (1954) defined MOST you only had similarity theories for neutral conditions. MOST was created to be used for non-neutral conditions as well.

The non-dimensional stability parameter ζ is defined as:

$$\zeta \equiv \frac{z}{L} \tag{2.11}$$

where z is the height and

$$L = -\frac{u_*^3 T_0}{\kappa g \overline{w'T_v'}} \tag{2.12}$$

is as the Obukhov length introduced by *Monin and Obukhov* (1954), u_* is the friction velocity (Equation 2.6), T_0 is the mean temperature, $\kappa \approx 0.4$ is the von-Karman constant, $g \approx 9.81$ m s^{-2} is the gravitational acceleration and $\overline{w'T_v'}$ is the kinematic heat flux (from Equation 2.1). For stable stratification ζ is positive, and the heat flux has a

downward direction ($H_s < 0$) and $L > 0$. It is the opposite for unstable stratification, and it should go towards zero for neutral stratification ($H_s \approx \zeta \approx 0$).

The non-dimensional gradients for momentum and heat are defined by *Monin and Obukhov* (1954) as:

$$\phi_m(\zeta) = \frac{\kappa \cdot z}{u_*} \frac{dU}{dz} \tag{2.13}$$

$$\phi_h(\zeta) = \frac{\kappa \cdot z}{T_*} \frac{d\Theta}{dz} \tag{2.14}$$

where dU/dz is the wind gradient (Equation 4.17) and T_* is the temperature scale:

$$T_* = -\frac{\overline{w'T'}}{\kappa u_*} \tag{2.15}$$

$T_* > 0$ for stable stratification, $T_* < 0$ for unstable stratification and $T_* \approx 0$ for neutral stratification. If we integrate Equation 2.13 we get the wind speed as a function of height (*Monin and Obukhov*, 1954)

$$u(z) = \frac{u_*}{\kappa}\left[\ln \frac{z}{z_0} - \psi_m\left(\frac{z}{L}\right)\right] \tag{2.16}$$

where ψ_m is the integral of the universal function ϕ_m, giving the derivative:

$$\frac{du}{dz} = \frac{u_*}{\kappa}\left[\frac{1}{z} + \phi_m(\zeta)\right] \tag{2.17}$$

which is the gradient of the wind. The Flux Richardson number, which is another stability parameter, is defined as(e.g. *Foken*, 2008; *Grachev et al.*, 2005):

$$Rf = \frac{g}{\overline{T}} \frac{\overline{w'T'}}{\overline{w'u'}\left(\frac{du}{dz}\right)} \equiv \frac{z/L}{\phi_m} \tag{2.18}$$

The critical Flux Richardson number is $Rf_c = 1.0$, where the flow changes to a quasi-laminar flow (e.g *Foken*, 2008).

Local scaling

The validity of classic MOST is found to be good for weakly stable conditions (*Grachev et al.*, 2005). For the very stable cases, however, classical MOST breaks down. The surface layer can no longer be described by only the surface values. This is because the scales are assumed to be independent of the height, and local scaling therefore often goes by the name z-less scaling. In order for z L^{-1} to not vary with height, L can no longer be the same for different heights. We account for this by replacing the Obukhov length, L, with the local Obukhov length, Λ, (e.g. *Nieuwstadt*, 1984) which uses local

values for the different heights instead of the surface values.

$$\Lambda = -\frac{\tau^{3/2} T_0}{\kappa g \overline{w'T_v'}} \tag{2.19}$$

where $\tau = [(\overline{u'w'})^2 + (\overline{v'w'})^2]^{1/2}$ which is the same as u_*^2 but for the measurement height z as opposed to the surface.

The stability parameter now becomes:

$$\zeta \equiv \frac{z}{\Lambda} \tag{2.20}$$

From the analysis of data from the SHEBA campaign (section 2.4) *Grachev et al.* (2005) found that classic MOST is valid for $\zeta \leq 0.1$, and local scaling will take over for $\zeta > 0.1$ as long as the Ekman number $\mathrm{Ek} \geq \mathrm{Ek_c} \approx 1$, which is defined as (e.g. *Grachev et al.*, 2005):

$$Ek = -\frac{\overline{u'w'}}{2\Omega \sin(\varphi) z U} = \frac{u_*^2}{2\Omega \sin(\varphi) z U} \tag{2.21}$$

where $\overline{u'w'}$ is the covariance of vertical and horizontal wind, Ω is the angular velocity of the earth, φ is the latitude, and z is the measurement height. The Ekman number defines the ratio of the frictional force and the Coriolis force (e.g. *Grachev et al.*, 2005).

Based on these findings *Grachev et al.* (2005) divides different scaling regimes:

1. **Surface layer scaling regime:**
   This is a scaling regime for weakly stable conditions ($0 < \zeta \leq 0.1$), where the fluxes are approximately constant with height, and therefore classic MOST are applicable, as long as $\mathrm{Ek} >> 1$ and $\mathrm{Ri_B} << \mathrm{Ri_{B,\,cr}}$.
2. **Transition regime:**
   This is the scaling regime for fairly stable conditions ($\zeta > 0.1$) where MOST is adequate as long as local scaling is applied, given that $\mathrm{Ek} \geq \mathrm{Ek_{cr}} \approx 1$, which approximately corresponds to $0.1 < \zeta < O(1)$. The flow is not effected by the Coriolis force.
3. **Turbulent Ekman layer:**
   The scaling regime for very stable conditions when $\mathrm{Ek} \leq \mathrm{Ek_{cr}} \approx 1$ (typically $O(1) < \zeta < O(10)$) is represented by small fluxes, and with wind influenced by the Coriolis force. The surface layer is very shallow.
4. **Intermittently turbulent Ekman layer:**
   Here the turbulence has collapsed, and the effect by Coriolis is significant. Features from an Ekman spiral can be seen even near the surface. Surface stress is no longer important, and u_* is no longer a valid scaling parameter. It is typically in the order $\zeta > O(10)$.

2.4 The SHEBA campaign

The Surface Heat Budget of the Arctic Ocean (SHEBA) campaign was conducted on the sea ice north of Alaska from October 1997 to October 1998 (*Uttal et al.*, 2002). They froze in with the ship *Des Groseilliers* from the Canadian Coast Guard, and drifted with the sea ice for more than 2800 km (e.g. *Grachev et al.*, 2005), which can be seen in Figure 2.2a. A 20 meter high meteorological tower was deployed, measuring turbulent and mean meteorological parameters at 5 different levels (2.2, 3.2, 5.1, 8.9 and 18.2 m). A photo of the SHEBA camp is seen in Figure 2.2b. Among others, *Grachev et al.* (2005) and *Grachev et al.* (2013) have analyzed the SHEBA data, and in particular the applicability of classical MOST and MOST using local scales (section 2.3), and some of their results will be compared with the results from our dataset.

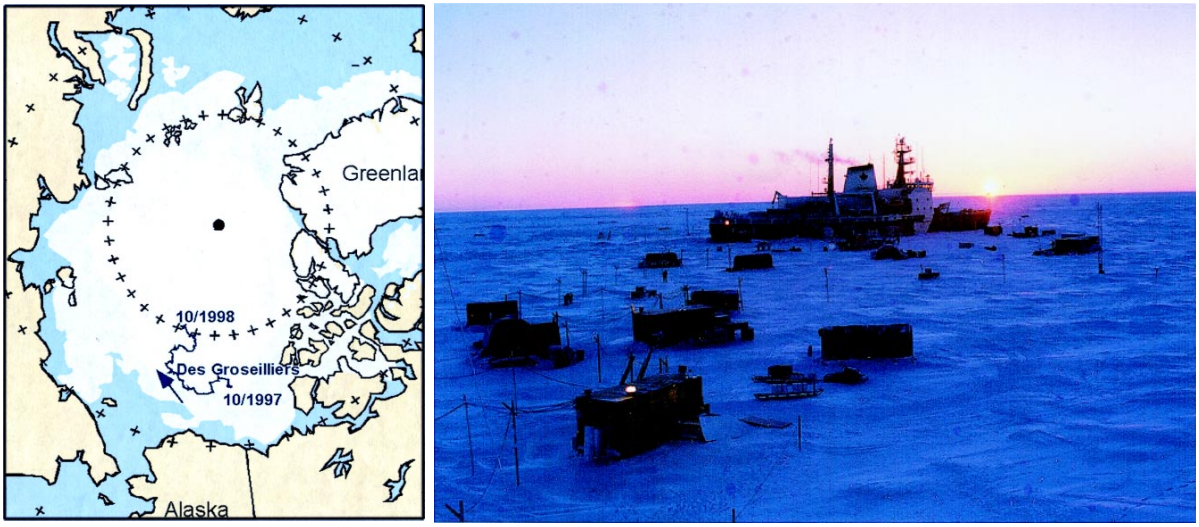

(**a**) (**b**)

Figure 2.2: Map of the ice drift of the SHEBA campaign (**a**) and a photo of the camp from October 1997 (**b**). (**a**) and (**b**) are reprinted from *Uttal et al.* (2002).

3 Measurement campaign

In the following chapter we will describe the study site (Section 3.1), the different instruments used in the campaign (Section 3.3) and present the data collected (Section 3.2).

3.1 Study site

Students participating in the AGF-350/850 course at the University Centre in Svalbard carried out measurements in Adventdalen between the 14th of February 2014 and the 5th of March 2014. Some of the deployed stations were kept running for another month, until the 4th of April 2014.

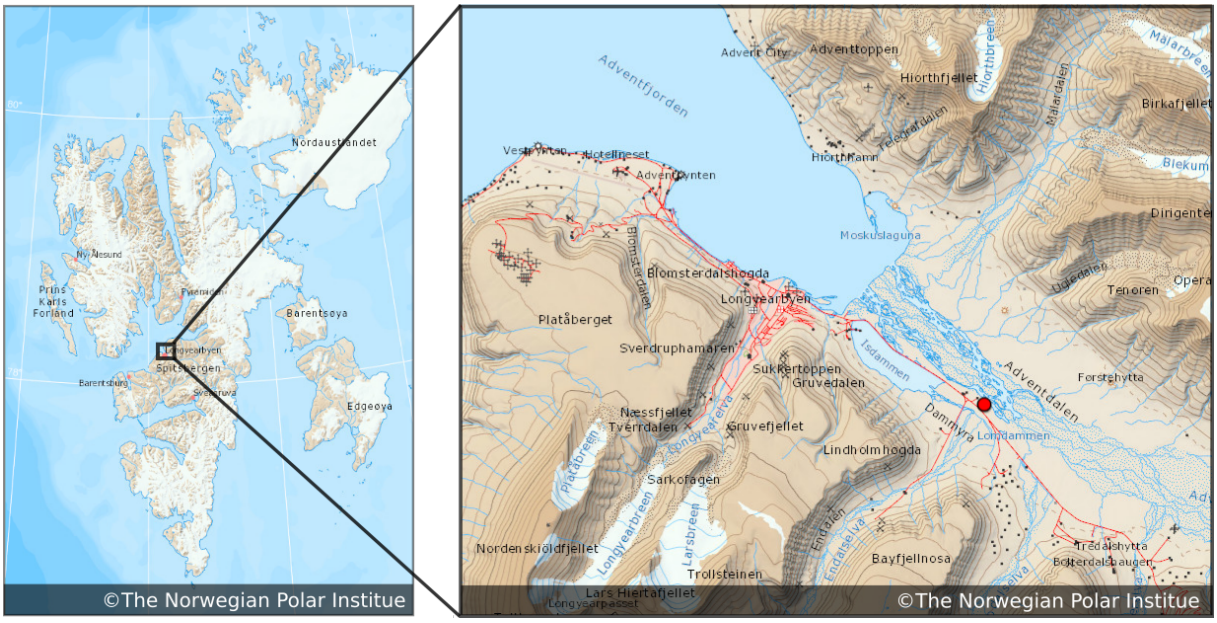

Figure 3.1: Map of Svalbard (left), and Adventdalen with the surrounding mountains (right). The red circle marks the location of the study site. Maps are from the Norwegian Polar Institue[1].

The Adventdalen valley is a NW-SE[2] oriented valley on Svalbard. The valley is an extension of Adventfjorden, a side fjord of the SW-NE[3] oriented Isfjorden, which can

[1] `toposvalbard.npolar.no` Accessed June 21, 2016.
[2] NW - North west; SE - South east
[3] SW - South west; NE - North east

be seen in Figure 3.1. It is approximately 20 km long and 4 km wide, with mountains on the sides in the range of around 1000 meter height. The terrain in the bottom of the valley is relatively flat and homogeneous, while the surrounding terrain is highly heterogenous.

Since Adventdalen ends up in Adventfjorden the sea-ice conditions play an important role (*Mayer et al.*, 2012). Isfjorden, and Adventfjorden, were ice-free for the whole winter in 2014. This means that Adventdalen could be influenced by advection from the relatively warm water, in the ice-free fjord.

The position of our measurement site is shown with the marker in Figure 3.1. It is located on the south side of the valley, close to the road. We would expect the wind to be orographically forced along the main valley axis, but the Endalen valley to the SW of the station could also lead to an orographically induced flow from that direction.

3.2 Measurements

The dataset collected during the campaign is the following:

- 3D wind vector and sonic temperature from Sonic anemometers at 2 levels (1.97 m and 4.06 m) at a 20 Hz resolution.
- Wind, temperature and humidity at a 1 Hz resolution at 2 levels (2 m and 10 m).
- 4 component radiation balance at 1.5 m with 5 minute resolution.
- 25 tethered balloon soundings measuring temperature, humidity and wind during 7 days.
- 24 SUMO flight measurements during 8 days.

An example of the basic data set is shown as time series for one week in Figure 3.2 and 3.3. The corresponding plots of all seven campaign weeks can be found in Appendix A.1. The instruments used in the campaign and of importance to this thesis, are described in the following section.

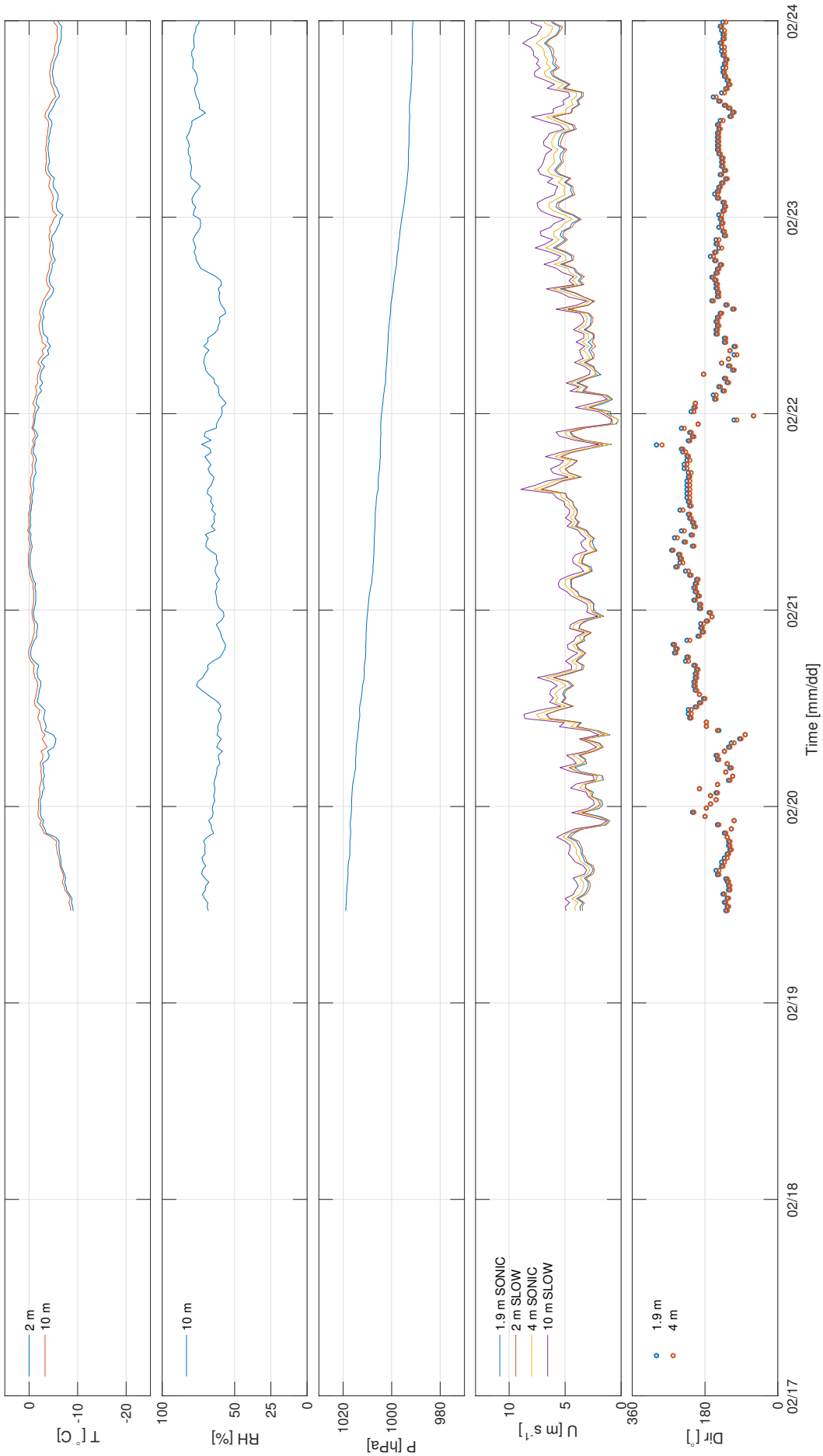

Figure 3.2: Meteorological parameters measured in Adventdalen from the 18th to the 24th of February 2014. It shows, from top to bottom, temperature at 2 m and 10 m, relative humidity at 10 m, pressure, wind speed and wind direction at different heights and from to types of sensors.

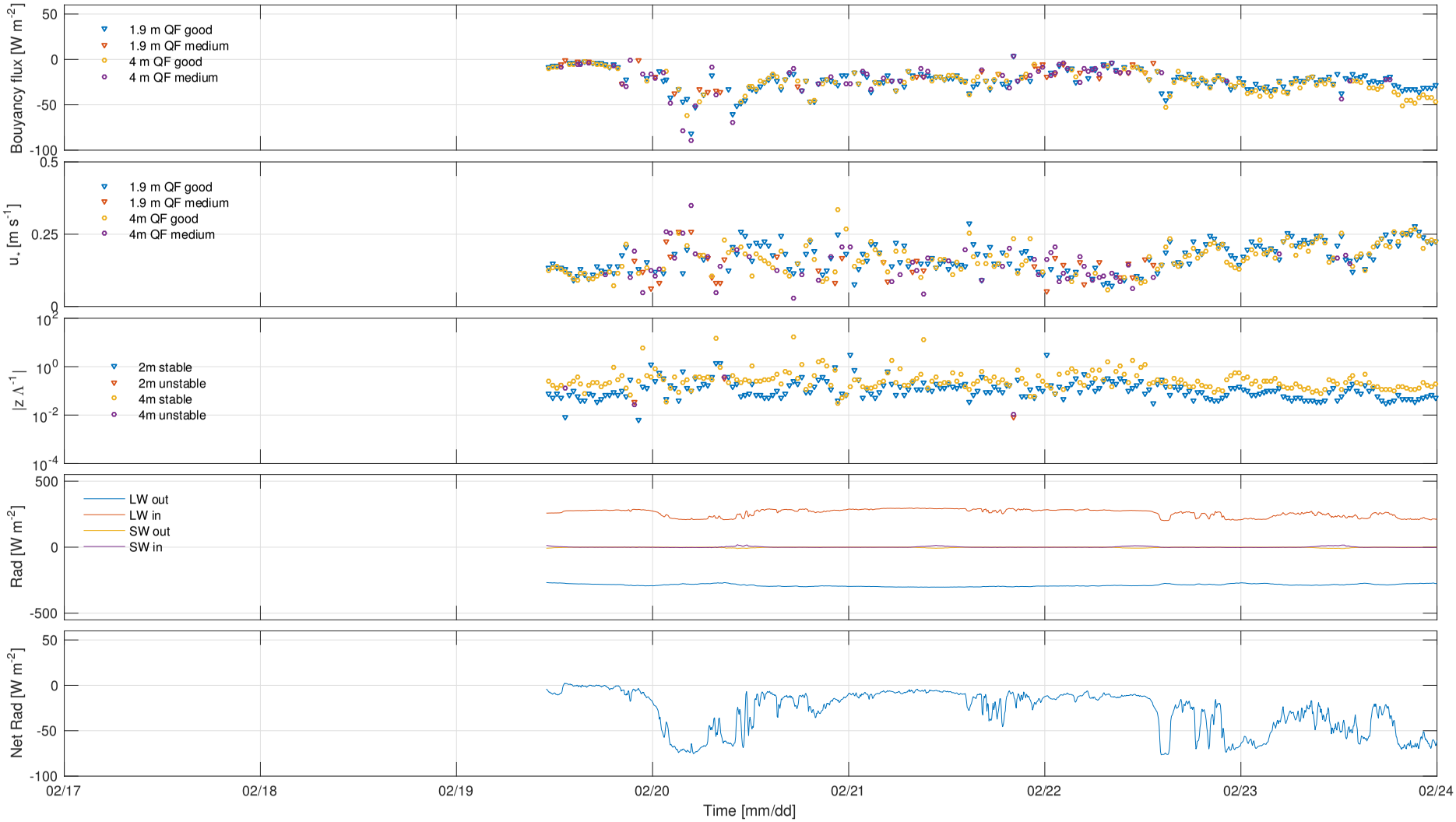

Figure 3.3: Derived meteorological parameters based on the measurements in Adventdalen from the 18th to the 24th of February 2014. It shows, from top to bottom, the buoyancy flux at 1.9 and 4 m, the friction velocity u_* at 1.9 and 4 m, the local stability parameter $z\ \Lambda^{-1}$ at 1.9 and 4 m, incoming and outgoing longwave and shortwave radiation, and the net radiation. The first three plots also include the information on the data quality as color code (see Section 4.1.5).

3.3 Instrumentation

For the high frequency measurements we used a set up with two CSAT3 Sonic anemometers at two levels (Section 3.3.1) of around 2 and 4 meter height. For the slow response measurements we mounted a 10-meter mast featuring temperature, humidity, wind speed and wind direction at 2 levels (Section 3.3.2) of around 2 and 10 meter height. We also had one radiometer to measure shortwave and longwave radiation(Section 3.3.3). Measurements with tethersondes and the SUMO airplane were also conducted. More detailed descriptions of the different set ups will be given in the following sections.

3.3.1 Fast response sensors

For the high frequency measurements we mounted two Sonic anemometers at two different heights, 1.97 and 4.06 meters. They measured the wind speed, wind direction and sonic temperature at both levels. The Sonic anemometers used in the setup where two CSAT3 from Campbell Scientific, which will be described next.

CSAT3

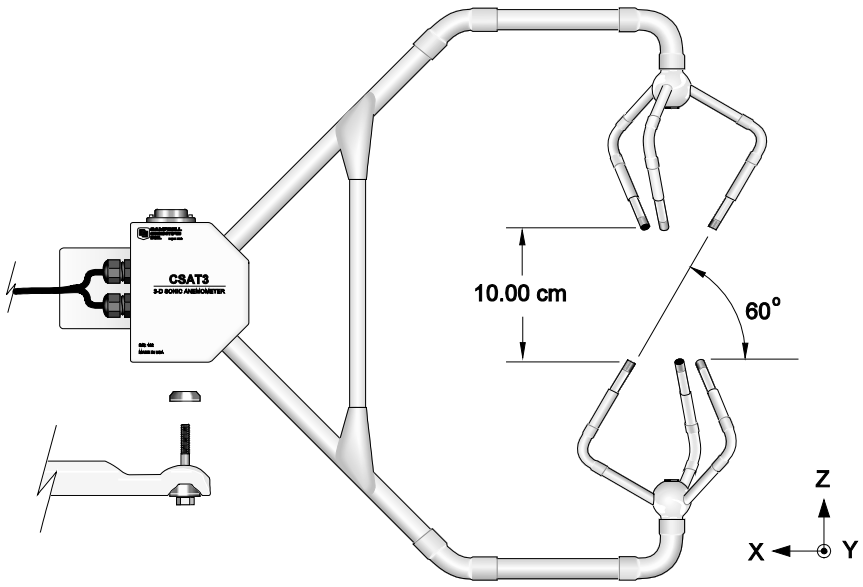

Figure 3.4: Illustration of the CSAT3 Sonic Anemometer. Reprinted from *Campbell Scientific* (2015).

CSAT3 is an ultrasonic anemometer used to measure the wind speed in three dimensions. The wind is measured by using three pairs of non-orthogonally oriented transducers, sensing the horizontal and vertical wind. The wind speed is directly related to the time of flight for each signal, between the different pairs of transducers,

while the temperature is related to the speed of sound, which depends on the air density, directly related to temperature and humidity.

The CSAT3 Sonic anemometer gives the wind component in 3 directions, and and the sonic temperature T_s, which is almost identical to the vertical temperature T_v (e.g. *Foken*, 2008):

$$T_v = T(1 + 0.38\frac{e}{p}) \tag{3.1}$$

$$T_s = T(1 + 0.32(\frac{e}{p}) \tag{3.2}$$

where T is the temperature, p is the pressure and e is the water vapor pressure. The sonic temperature can easily be used to calculate the buoyancy flux. *Liu et al.* (2001) found the buoyancy flux to be around 10% and 30% larger than the sensible heat flux for stable and unstable conditions, respectively, when using the CSAT3 Sonic anemometer.

Figure 3.4 (*Campbell Scientific*, 2015) shows the CSAT3, and the specifications for the instrument are shown in Table 3.1 and the errors are shown in Table 3.2.

Table 3.1: Specifications for the CSAT3 Sonic anemometer (*Campbell Scientific*, 2015).

	Range	**LSB**
Operating temperature:	-30° to 50°C (cold shifted: -40° to 40°C)	
$\mathbf{u}_x$	±30 m s^{-1}, ±60 m s^{-1}	15 mm s^{-1}, 30 mm s^{-1}
$\mathbf{u}_y$	±30 m s^{-1}, ±60 m s^{-1}	15 mm s^{-1}, 30 mm s^{-1}
$\mathbf{u}_z$	±8 m s^{-1}	4 mm s^{-1}
c	±300 to 366 m s^{-1} (-50° to 60°C)	16 mm s^{-1} (0.026°C)

Table 3.2: Error estimates for the CSAT3 Sonic anemometer (*Campbell Scientific*, 2015). All error estimates are calculated for the range of -30 to 50°C, wind speeds < 30 m s^{-1} and wind direction ±170°.

	Wind error	
Gain error	< ±2% of reading	Wind vector ±5° of horizontal
	< ±3% of reading	Wind vector ±10° of horizontal
	< ±6% of reading	Wind vector ±20° of horizontal
Offset error	< ±8 cm s^{-1}	for u_x and u_y
	< ±4 cm s^{-1}	for u_z

3.3.2 Slow response sensors

To measure slow meteorological parameters we mounted a 10-meter mast, with measurements of wind speed, wind direction, temperature and humidity at two heights of 2 and 10 meters. The relative humidity sensor at 2 meters did not work during the whole campaign. The rest of the sensors were operational during the whole campaign. They are listed in Table 3.3, and further described below.

Table 3.3: Sensors mounted on the 10-m mast and their respective heights and parameters is shown. The parameters measured are temperature (T), relative humidity (RH), wind speed (WS), wind direction (WD), and atmospheric pressure (P).

Sensor:	**2 m**	**10 m**	**T**	**RH**	**WS**	**WD**	**P**	**Remarks**
Young 41342	X	X	X	-	-	-	-	
HygroClip	(X)	X	X	X	-	-	-	RH not working at 2 m
R.M. Young's 05103	X	X	-	-	X	X	-	
CS100	X	-	-	-	-	-	X	

Young model 41342 Temperature Probe

To measure the temperature on the 10-meter mast, a Young model 41342 Temperature Probe is used (*Young*, 2004). The measurement is based on the resistance dependency of a platinum based sensing element. The specifications are shown in Table 3.4.

Table 3.4: Young model 41342 Temperature Probe specifications (*Young*, 2004).

	Temperature
Measurement range:	-50° to 50°C
Accuracy at 0°C:	±0.3°C
Response time:	10 s
Sensor type:	Platinum RTD

HygroClip

We used the HygroClip sensor, which is a high accuracy probe (*Rotronic*, 2002), to measure relative humidity and temperature. We only use the humidity measurement in our data analysis, since the temperature sensor on the Young Temperature Probe (Section 3.3.2) is assumed to be faster and more reliable. Unfortunately, the humidity sensor at 2 meters did not work for the whole campaign. The specifications for the HygroClip are shown i Table 3.5.

Table 3.5: HygroClip sensor specifications (*Rotronic*, 2002).

	Humidity:	**Temperature:**
Measurement range:	0 - 100% RH	-20° to 85°C
Accuracy at 23°C:	±0.2% RH	±0.2°C
Sensor type:	HYGROMER®-C94	PT100 1/3 DIN
Sampling time:	< 0.7 s (min excitation time 3 s)	

R.M. Young's 05103

We measured the wind using the R.M Young's 05103 Wind Monitor, cabled by Campbell Scientific. It uses a four bladed, helicoid-shaped, propeller to measure the wind speed, while a potentiometer measures the wind direction (*Campbell Scientific*, 2010b). The specifications for the R.M Young wind monitor are shown in Table 3.6.

Table 3.6: Specifications for the R.M. Young's 05103 Wind Monitor (*Campbell Scientific*, 2010b).

	Wind Speed:	**Wind direction:**
Range:	0 - 100 m s^{-1}	0° - 360° mechanical
Starting treshold:	1 m s^{-1}	1.1 m s^{-1} (@ 10° displacement)
Accuracy:	± 0.3 m s^{-1} or 1% of reading	± 3°
Operating temperature:	-50° to 50°C (non-riming conditions)	

CS100 barometric sensor

The CS100 Barometric pressure sensor (*Campbell Scientific*, 2010a) is used to measure the atmospheric pressure. The sensor specifications are shown in Table 3.7.

Table 3.7: Specifications for the CS100 Barometric Pressure sensor (*Campbell Scientific*, 2010a).

	Pressure:
Measurement range:	600mb to 1100 mb (hPa)
Operating temperature:	-40°C to 69°C
Humidity range:	non-condensing up to 95% RH
Resolution:	0.01 mb
Accuracy:	±1.5 mb at -20°C to 50°C

3.3.3 Radiation sensors

The Kipp & Zonen CNR-1 net radiometer measured both longwave and shortwave radiation, both incoming and outgoing in 4 separate channels. It consists of two CM3 pyranometers and two CG1 pyrgeometers, measuring shortwave and far infrared radiation, respectively. A PT-100 platinum element is used to measure the instrument temperature. The instrument is heated to avoid dew and frost from covering the sensors. An illustration of the Kipp & Zonen setup is shown in Figure 3.5, and the specifications of the instrument are shown in Table 3.8.

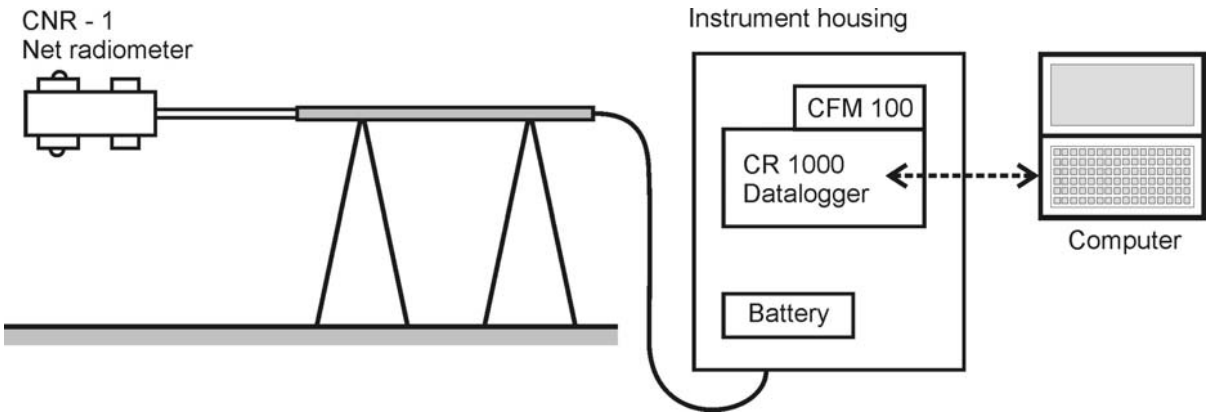

Figure 3.5: Illustration of the CNR-1 net radiometer made by *Lange* (2011).

Table 3.8: CNR-1 net radiometer range and accuracy (*Campbell Scientific*, 2011).

	Range:	**Spectral range:**	**Accuracy:**
CM3:	0 - ~1500 W m^{-2}	305-2800 nm	±10 % for daily totals
CG3:	-250 - 250 W m^{-2}	5 - 50 μm	±10 % for daily totals
Instrument temperature:	-40° to 80°C		±2°C
Operating temperature:	-40° to 70°C		

3.4 Synoptic conditions

We will now go trough the meteorological conditions during the period of our measurement campaign. Figure 3.6 shows the main meteorological parameters for the whole campaign. A more detailed weekly overview of all meteorological parameters are shown in Appendix A.1. In the following sections we will present and discuss the different parameters, starting with temperature.

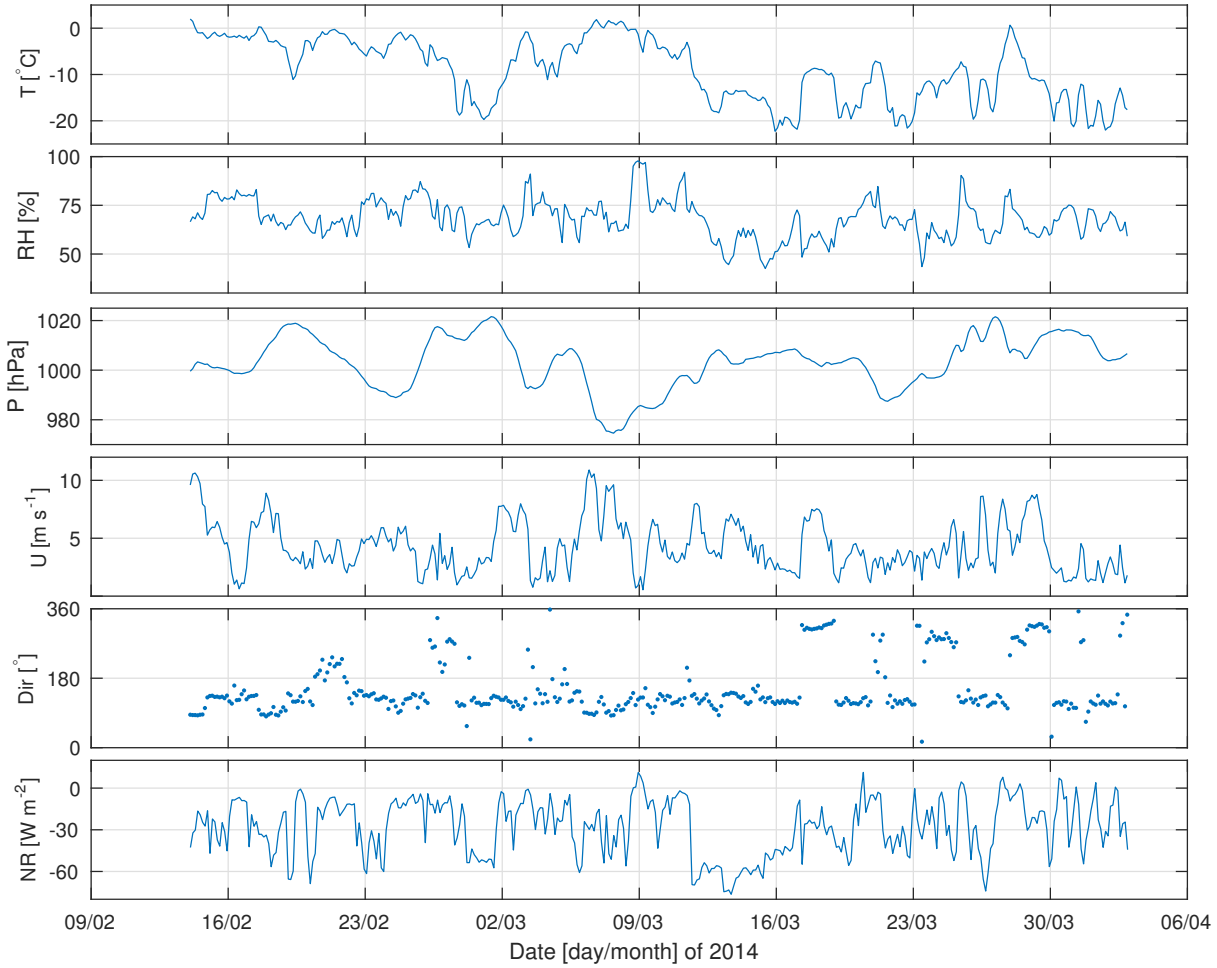

Figure 3.6: Overview of different meteorological parameters during the campaign. The parameters shown are temperature (T), pressure (P), relative humidity (RH), net radiation (NR), wind direction (Dir) and wind speed (U). All values are 3 hour means taken from sensors mounted on the 10-meter mast, except for the net radiation which is at a radiometer next to the 10-m mast.

Temperature

The temperature starts relatively mild in February before dropping towards the end of the month. During first week of March is then relatively mild again, reaching even positive temperatures during March 6-8. The following week the temperatures are continually dropping, and reaching the campaign minimum of -22°C on March 16. From the middle of March it alternates between cold and medium cold conditions

due to the changing synoptic forcing, as the wind is coming from the NW during the most of the periods with medium cold conditions. NW wind corresponds to air masses coming from Adventfjorden, which could be the source for the higher temperatures. Towards the end of the campaign the temperature starts also to show an annual variation.

Table 3.9 is an overview of the monthly normal temperature, the monthly mean temperature, and the deviation from the normal, using data from the Norwegian Meteorological Institute[4]. For February, March and April we see that the mean temperatures are 14.5°C, 7.1°C and 2.5°C warmer than the normal values, respectively. The deviations for February and March can be described as dramatic. It is far more mild than the climatology, meaning we would expect the stratification to be less stable than normal. The period before the middle of March seems to be the main source for the positive temperature anomaly, while the period after seems to be more in touch with the climatology.

Table 3.9: The monthly mean temperature ($\overline{T}$), the normal temperature (T_{normal}) and the temperature deviation from the normal ($T_{deviation}$) for the measuring station at Svalbard Airport. The normal is the average for the period 1961 to 1990 for each month. Data is from the Norwegian Meteorological Institute.

Month:	$\overline{\mathbf{T}}$**:**	$\mathbf{T_{normal}}$**:**	$\mathbf{T_{deviation}}$**:**
February	-1.7°C	-16.2°C	14.5°C
March	-8.6°C	-15.7°C	7.1°C
April	-9.7°C	-12.2°C	2.5°C

Wind

The wind direction is generally from the SE, which means the wind comes from within the Adventdalen valley. Periods with NW wind, from Adventfjorden, also occurs at some occasions. The NW wind lasts at no occasion longer than 2 days, while the SE wind can be consistent for periods up to a week (see Appendix A.1 for detailed time series). For most of the campaign the wind speeds were low, in the range lower than 6 m s^{-1}. Occasionally we got wind speeds up to 11 m s^{-1}, which is still relatively low compared to what is possible on Svalbard.

The corresponding wind roses for the 2 meter and 4 meter fast response data sets are shown in Figure 3.7. Here we can clearly see the two main wind directions, which correspond to wind from within the valley (SE) and from Adventfjorden (NW). We also, at times, have short episodes of wind from the SW, which would correspond to wind coming from the Endalen valley (see Figure 3.1).

[4] https://www.yr.no/sted/Norge/Svalbard/Svalbard_lufthavn_målestasjon/klima.html

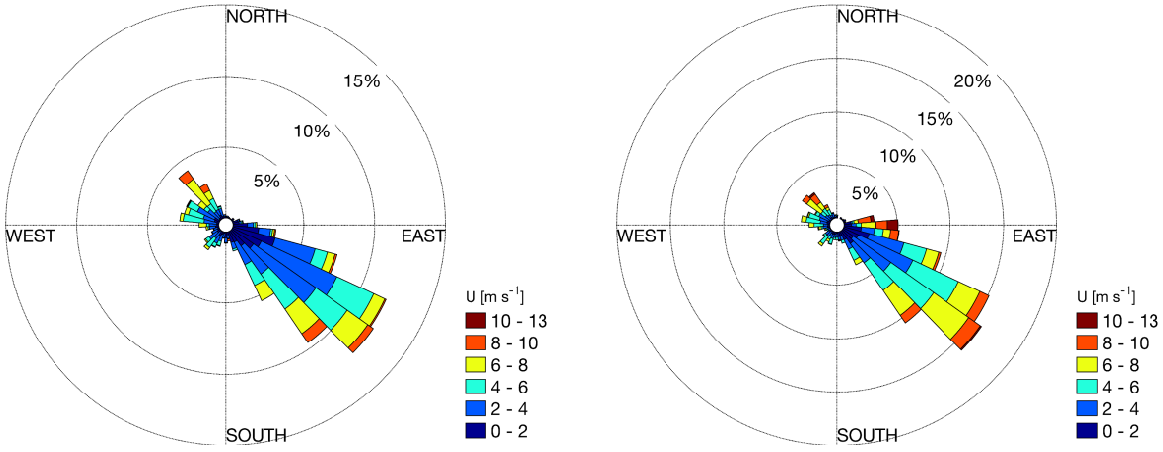

(**a**) 2 m height

(**b**) 4 m height

Figure 3.7: Wind rose for Adventdalen at 2 m (**a**) and 4 m (**b**) height. This shows histograms of the wind speed, with respect to wind direction and percentage of occurrences. The data are 30 minute averages of the high frequency data from the Sonic anemometers.

Radiation

The net radiation in Figure 3.6 is mostly negative, which we would expect in the Arctic winter, with some smaller periods with positive net radiation. It is generally fluctuating from 2 to -60 W m^{-2}. One exception is a period from around the 13th to the 18th of March, where we have a long lasting negative net radiation in the range of -50 to -80 W m^{-2}, opposed to the more normal fluctuations in the 2 to -60 W m^2 range. This could potentially lead to very stable conditions, if the wind is relatively calm, and the rest of the conditions favor a stable boundary layer. But since the stability depends on a lot of different parameters, the only conclusion we can say is that the net radiation favors stable conditions during this period. Turbulent mixing induced by wind shear could possibly oppose this.

4 Methodology

In section 4.1 we present the software used in the analysis of the high-frequency data. Then we explain the calculation of the wind and temperature gradients during the campaign in section 4.2.

4.1 Data processing

We used the software Turbulence Knight 3.11, in detail described by *Mauder and Foken* (2015), for the statistical analysis of the Sonic anemometer data and the calculation of the different turbulence parameters. It is an open source software package that is widely used for turbulence data analysis (e.g *Göckede et al.*, 2008; *Mauder et al.*, 2008; *Song et al.*, 2013; *Eigenmann et al.*, 2011) and is the standard software used in the CarboEurope network (*Mauder and Foken*, 2015). One of its strength is a comprehensive system of quality control and flagging with the possibility to choose from different flagging systems (e.g. *Foken*, 2008; *Mauder et al.*, 2013; *Mauder and Foken*, 2015). It allows the user to select appropriate subsets of the overall data basis used in this thesis, depending on the turbulent parameter of interest.

The main settings used in Turbulence Knight are shown in Table 4.1, while the full parameter files for the two different heights used in this thesis are shown in Appendix A.2. The important settings will be explained in more detail in the following section.

4.1.1 Planar fit method

When doing measurements with a sonic anemometer we want the vertical velocity to be perpendicular to the mean streamline direction, and the two horizontal components to be parallel to the streamline direction. In reality the anemometer will be tilted compared to the streamline direction. To correct for this tilt we make use of the planar fit method proposed by *Wilczak et al.* (2001). The wind in the mean streamline direction is:

$$\vec{u}_p = \mathbf{P}(\vec{u}_m - \vec{c}) \tag{4.1}$$

Table 4.1: Settings used in TK3.11. True indicates that the setting is turned on, while false indicates it is turned off.

Setting	2-m Sonic	4-m Sonic
Sonic type	CSAT3	
Measuring height	1.97 m	4.06 m
Canopy height	0.0 m	0.0 m
Orientation	236°	230°
Height a.s.l.	8 m	12.06 m
Averaging interval	30 min	
Missing values	Take last value	
MAD spike test	True (following *Mauder et al.*, 2013)	
Std for spikes	3.5	
Reference measurements	False	
Max number of missing values in averaging interval	1%	
Calculate random error and instrument noise	True (following *Mauder et al.*, 2013)	
Planar fit	True (following *Wilczak et al.*, 2001)	
Rotation to mean wind direction	True	
Scalar fluxes	True	
Double rotation	False	
Stationary test	True (following *Foken et al.*, 2012)	
Test on developed turbulent conditions with integral turbulence characteristics	True (following *Foken and Wichura*, 1996)	
Check for independence of quality flags due to corrections	True (following *Mauder et al.*, 2013)	
Check for w-offset	True (following *Mauder et al.*, 2013)	
Quality flags	True (following *Mauder et al.*, 2013)	
Footprint analysis	False	
Ogive	False	
Spectral analysis	False	

where $\vec{u}_p$ is the wind vector in the mean streamline direction, $\vec{u}_m$ is the measured wind vector, $\vec{c}$ is the mean offset error of the instrument, and $\mathbf{P}$ is a rotational matrix transforming the wind vector to the mean streamline direction.

4.1.2 Stationarity test

The eddy covariance method is based on an assumption of stationary conditions. To check for stationarity, we perform a stationarity test (or a steady state test) following *Foken et al*. (2012) and *Foken and Wichura* (1996). The concept is used to identify non-stationarity which can be caused by changing weather patterns, gravity waves and mesoscale variability (*Foken et al.*, 2012).

The covariance of vertical wind w and X_s, which could be the horizontal wind speed or the Sonic temperature, is calculated for $M = 6$ intervals of 5 minutes. N is denoting the number of measuring points inside a 5-minute interval (*Foken et al.*, 2012).

$$(\overline{w'X_s'})_i = \frac{1}{N-1}\left[\sum_j w_j \cdot X_{sj} - \frac{1}{N}\left(\sum_j w_j \cdot \sum_j X_{sj}\right)\right] \tag{4.2}$$

Then we calculate the covariance for the 30-minute interval, taking the mean of the 6 5-minute intervals (*Foken et al.*, 2012):

$$\overline{w'X_s'}|_{SI} = \frac{1}{M}\sum_i (\overline{w'X_s'})_i \tag{4.3}$$

which will be compared with the covariance calculated for the whole 30-minute interval (*Foken et al.*, 2012):

$$|\overline{w'X_s'}|_{WI} = \frac{1}{M \cdot N - 1}\left[\sum_i \left(\sum_j w_j \cdot X_{sj}\right)_i - \frac{1}{M \cdot N}\sum_i \left(\sum_j w_j \cdot \sum_j X_{sj}\right)_i\right] \tag{4.4}$$

The difference between the covariances is then calculated (*Foken et al.*, 2012):

$$Ratio_{Cov} = \left|\frac{\overline{(w'X_s')_{SI}} - \overline{(w'X_s')_{WI}}}{\overline{(w'X_s')_{WI}}}\right| \tag{4.5}$$

If the difference between the covariances, $Ratio_{Cov}$, is less than 30%, the time series is defined as stationary (*Foken et al.*, 2012).

4.1.3 Test on developed turbulent conditions with integral turbulence characteristics

The flux-variance similarity is a good way to measure the development of the turbulent conditions (*Mauder and Foken*, 2015). The concept is that the ratio of the standard deviation of turbulent parameters and its flux is approximately a constant, or a function of stability (*Mauder and Foken*, 2015). These ratios are called integral turbulence characteristics and the one used here are based on *Foken and Wichura* (1996) with functions from *Foken et al.* (1991), where the ratio is a function of stability:

$$\frac{\sigma_{u,v,w}}{u_*} = c_1 \cdot [\phi_m \frac{z}{L}]^{c_2} \tag{4.6}$$

where u,v and w are the the horizontal and vertical wind in three directions, u_* is the friction velocity and L is the Obukhov length. For scalar fluxes X_* the ratio is defined

as:

$$\frac{\sigma_X}{X_*} = c_1 \cdot [\frac{z}{L} \cdot \phi_h \frac{z}{L}]^{c_2} \tag{4.7}$$

The constants used in Equation 4.6 and Equation 4.7 are shown in Table 4.2.

Table 4.2: Constants for the similarity functions given in Equation 4.6 and Equation 4.7 as presented by *Foken et al.* (1991) and *Mauder and Foken* (2015).

Parameter	$z\,L^{-1}$	c_1	c_2
σ_u/u_*	$0 > z\,L^{-1} > -0.032$	2.7	0
	$-0.032 > z\,L^{-1}$	4.15	1/8
σ_w/u_*	$0 > z\,L^{-1} > -0.032$	1.3	0
	$-0.032 > z\,L^{-1}$	2.0	1/8
σ_T/T_*	$0.02 < z\,L^{-1} < 1$	1.4	−1/4
	$0.02 > z\,L^{-1} > -0.062$	0.5	−1/2
	$-0.062 > z\,L^{-1} > -1$	1.0	−1/4
	$-1 > z\,L^{-1}$	1.0	−1/3

For near-neutral conditions ($-0.2 < z\,L^{-1} < 0.4$) *Thomas and Foken* (2002) has defined the following ratios:

$$\frac{\sigma_u}{u_*} = 0.44 \ln\left(\frac{z_+ \cdot f}{u_*}\right) + 6.3 \tag{4.8}$$

$$\frac{\sigma_w}{u_*} = 0.21 \ln\left(\frac{z_+ \cdot f}{u_*}\right) + 3.1 \tag{4.9}$$

where $z_+ = 1$ m.

There are no functions for stable conditions, but TK3.11 uses the same parameterizations for stable conditions as for unstable (*Mauder and Foken*, 2015).

$$ITC_\sigma = \left| \frac{\frac{\sigma_X}{X_*\,model} - \frac{\sigma_X}{X_*\,measurement}}{\frac{\sigma_X}{X_*\,model}} \right| \tag{4.10}$$

If the ratio $ITC_\sigma < 30\%$ we assume well developed turbulent conditions. This test will not be performed for the sensible heat, when the flux is smaller than 10 Wm^{-2}, because the ratio is not well defined in this case (*Mauder and Foken*, 2015).

4.1.4 Spike detection

To detect the spikes, a relation to the Median Absolute Deviation (MAD) is used. The data point x_i is defined as a spike if is outside the threshold (*Mauder et al.*, 2013):

$$\langle x \rangle - \frac{q \cdot \mathrm{MAD}}{0.6745} \leq x_i \leq \langle x \rangle + \frac{q \cdot \mathrm{MAD}}{0.6745} \tag{4.11}$$

where $\langle x \rangle$ is the median of x, q is a threshold value set to 3.5 in our analysis, and

$$\mathrm{MAD} = \langle |x_i - \langle x \rangle| \rangle \tag{4.12}$$

where $\langle\rangle$ denotes the median value. The value 0.6745 relates the MAD value to one standard deviation, assuming a Gaussian distribution, which is, however, not always the case for turbulent flows (*Mauder et al.*, 2013).

4.1.5 Quality flags

For the determination of data quality, we follow the method proposed by *Mauder et al.* (2013). The flags are based on a series of tests on the 30 minute statistics, and result in a flag for the different fluxes. Figure 4.1 illustrates the process of the quality analysis. The different quality flags and suggestions for the use of correspondingly flagged data points are shown in Table 4.3.

Table 4.3: Quality flags for our dataset based on the method from *Mauder et al.* (2013).

Flag	Quality	Use
Flag 0	Good quality data	Fundamental research
Flag 1	Medium quality data	Long-term observation programs
Flag 2	Low quality data	Should be discarded

Table 4.4: Consistency limits set for our data. Values outside the consistency limits will be filtered out. u,v and w are the wind speeds in the horizontal and vertical direction, respectively. T_s is the Sonic temperature, and the diag_CSAT3 is a diagnostic flag produced by the Sonic anemometer.

Quantity	Lower limit	Upper limit	Units
u, v	-50	50	m s^{-1}
w	-10	10	m s^{-1}
T_s	-50	30	°C
diag_CSAT3	0	63	

The different steps of the quality analysis in Figure 4.1 will be explained in the following sections. The process is following *Mauder et al.* (2013). All flags given are

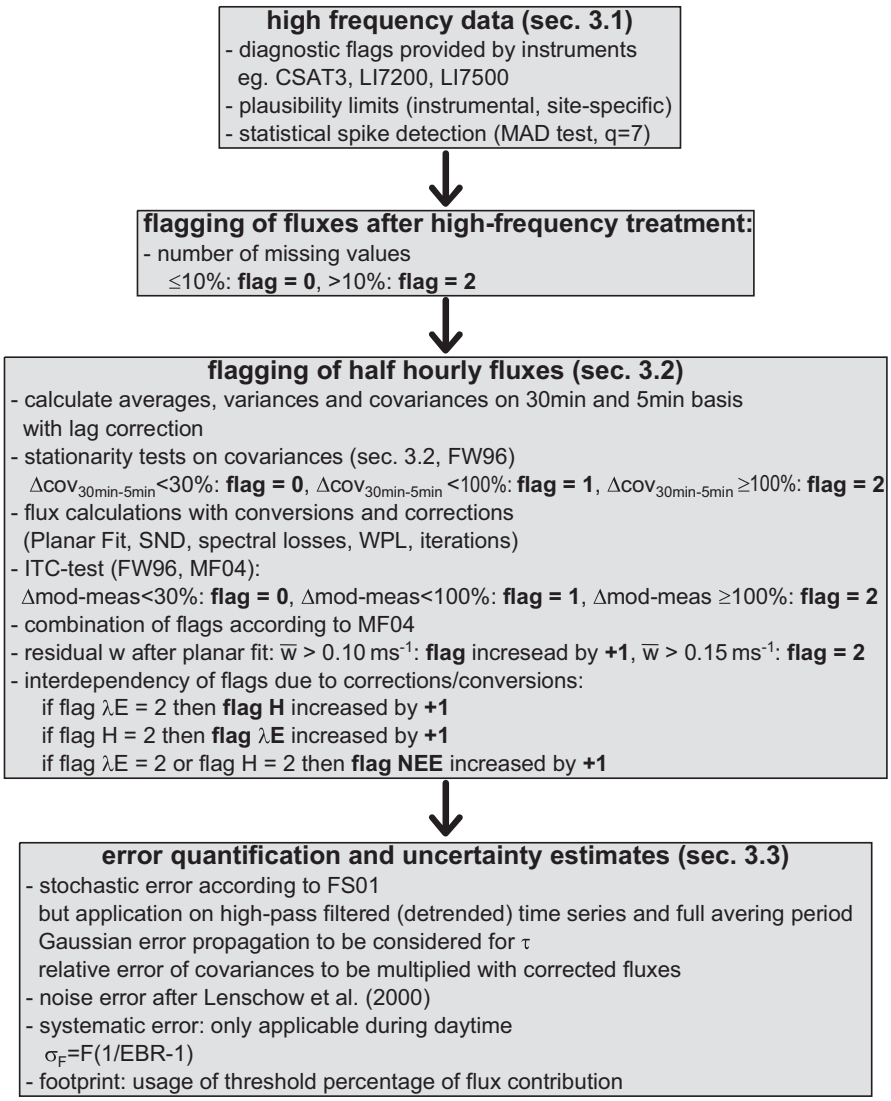

Figure 4.1: Process of the quality analysis. Reprinted from *Mauder et al*. (2013) with permission from Elsevier.

additive, meaning that if a flux is given two or more Flag 1 by different quality analyses, the resulting flag is Flag 2.

Flagging of high frequency data

The first set of quality tests is done on the high frequency data. The Sonic anemometer CSAT3, which we have used in the campaign, produces a diagnostic flag. Analyzing these flags will identify instrumental malfunctions, disturbances by animals or precipitation and power peaks. In the first step, all data outside the physically meaningful consistency limits (Table 4.4) will be filtered out. Then a MAD spike test (Section 4.1.4) is used to remove remaining outliers.

If more than 10% of the data points inside the window, which in our case is a 30-minute interval, are filtered out, the 30-minute block of data is discarded as bad

data (Flag 2). If not, it is defined as good data (Flag 0), and for all the data-points missing, we assign the value to be the last value.

Flagging of half hourly fluxes

After this both, 5-minute and 30-minute averages of variances and covariances are calculated. A stationarity test is performed (Section 4.1.2), where a difference in the 5-minute averages and the 30-minute averages of $Ratio_{Cov} > 30\%$ results in Flag 1, while $Ratio_{Cov} > 100\%$ results in Flag 2. A test on developed turbulent conditions with integral turbulence characteristics (Section 4.1.3) is also performed. Here $ITC_{\sigma} < 30\%$ results in Flag 0, $30\% < ITC_{\sigma} < 100\%$ results in Flag 1, and $ITC_{\sigma} > 100\%$ results in Flag 2.

For a meaningful application of the eddy covariance method, the mean vertical velocity needs to be approximately zero ($\overline{w} \approx 0$). If this is not the case, even after applying the planar fit coordinate transformation (Section 4.1.1), then this is a sign of strong vertical advection, which should result in flagging. *Mauder et al.* (2013) has defined the threshold based on *Foken and Wichura* (1996) that for $\overline{w} > 0.10$ m s^{-1} all flux flags are increased by 1, and under situations when $\overline{w} > 0.15$ ms^{-1} all fluxes get a Flag 2.

Then we check the interdependency of the data quality between the different fluxes, but because we neither have latent heat and CO_2 fluxes, this test does not change the flags for the heat and momentum flux.

Error quantification and uncertainty estimates

In the end the method calculates the different errors in the dataset. The instrumental noise is calculated following *Mauder et al.* (2013). An estimate of the stochastic error is calculated, and the systematic error due to insufficient sampling of large scale atmospheric motion as well. The systematic error is only applicable when you have a convective boundary layer. *Mauder et al.* (2013) describes in detail the calculation of the instrument noise and different errors. In the end TK3 gives an output for the error and the noise for the different fluxes. They do not effect the quality flags.

Flags in the Sonic dataset

The distribution of the quality flags in our dataset after the analysis are shown in Table 4.5.

Table 4.5: Quality distribution in the dataset from the two CSAT3 Sonic anemometers used in our campaign.

Parameter	Height	Flag 0	Flag 1	Flag 2
u_*	2m	54.0%	26.5%	17.5%
	4m	56.1%	39.9%	4.0%
HT_s	2 m	49.5%	24.1%	26.4%
	4m	47.5%	35.7%	16.8%

4.2 Calculation of gradients

In order to calculate the non-dimensional gradients in MOST (Section 2.3) we need to determine the wind and temperature gradients.

4.2.1 Wind gradient

In order to find the gradients for the wind, we need to assume a basic functional shape for the wind profile. The most straight forward method would be to find a linear fit to the data. A more realistic approach is to assume a logarithmic wind profile, and find a logarithmic fit.

Linear fit

A gradient approximated from a linear fit is shown in Equation (4.13):

$$\frac{du}{dz} = \frac{u_{z_2} - u_{z_1}}{z_2 - z_1} = A \tag{4.13}$$

where u is the absolute horizontal wind speed at the different levels, and A is the gradient.

Logarithmic fit

If we assume that the wind profile is logarithmic, the gradient should be linear in log-z-space. The wind speed is defined as a function height in Equation 2.16, with the gradient given in Equation 2.17. For neutral conditions the gradient in Equation 2.17 becomes:

$$\frac{du}{dz} = \frac{u_*}{\kappa z} \tag{4.14}$$

since $\zeta \approx 0$. For non-neutral conditions $\psi_m(\zeta)$ in Equation 2.16 will give the wind profile a systematic deviation from the logarithmic profile for stable and unstable stratification (*Monin and Obukhov*, 1954). It should be steeper for stable conditions, and less steep for unstable conditions. To fit our data to a wind profile we use a method using three data points, instead of just the two measured wind speeds. Since the wind speed is zero at the z_0, we can use this in a fit. We try to find the best fit to our data using a first degree polynom with a logarithmic height variable:

$$u(z) = A \ln z + B \tag{4.15}$$

We use the matlab function *polyfit* to find the coefficients A and B by using the wind measurements from the sonic anemometer at 2 and 4 meters, and setting the wind at the surface to zero ($u_{z=0} = 0$), which gives us three points to make a fit from. This gives a separate value to A and B for each time step. Equation 4.15 is equivalent to the wind profile equation (Equation 2.16). To get the gradient we take the derivative of Equation 4.15. This gives

$$\frac{du}{d\ln z} = A \tag{4.16}$$

which is equivalent to

$$\frac{du}{dz} = \frac{A}{z} \tag{4.17}$$

where A is the coefficient calculated when fitting Equation 4.15.

4.2.2 Temperature gradient

In order to calculate the non-dimensional temperature profile (Equation 2.14) we need to know the potential temperature gradient. The first thing to do is to convert the sonic temperature, T_s, at the two levels into potential temperature. We assume that the sonic temperature is approximately equal to the virtual temperature ($T_s \approx T_v$) (e.g. *Foken*, 2008). Then we calculate the virtual potential temperature by (e.g. *Stull*, 1988):

$$\Theta_v = T_v \left(\frac{p_0}{p}\right)^{\frac{R_L}{c_p}} \approx T_s \left(\frac{p_0}{p}\right)^{\frac{R_L}{c_p}} \tag{4.18}$$

where p is the measured pressure, $p_0 = 1000$ hPa is the reference pressure, $c_p = 1004.67$ J kg^{-1}K^{-1} is the specific heat of dry air at constant pressure and $R_L = 287.058$ J kg^{-1}K^{-1} is the gas constant of dry air. Then we calculate the gradient linearly from the two data-points:

$$\frac{d\Theta_v}{dz} = \frac{\Theta_{v,4m} - \Theta_{v,2m}}{z_{4m} - z_{2m}} \tag{4.19}$$

4.2.3 Temperature bias correction

After calculating the gradients we saw that they were never negative, and that the difference in temperature between 4 m and 2 m never were around zero, which we would expect during neutral conditions.

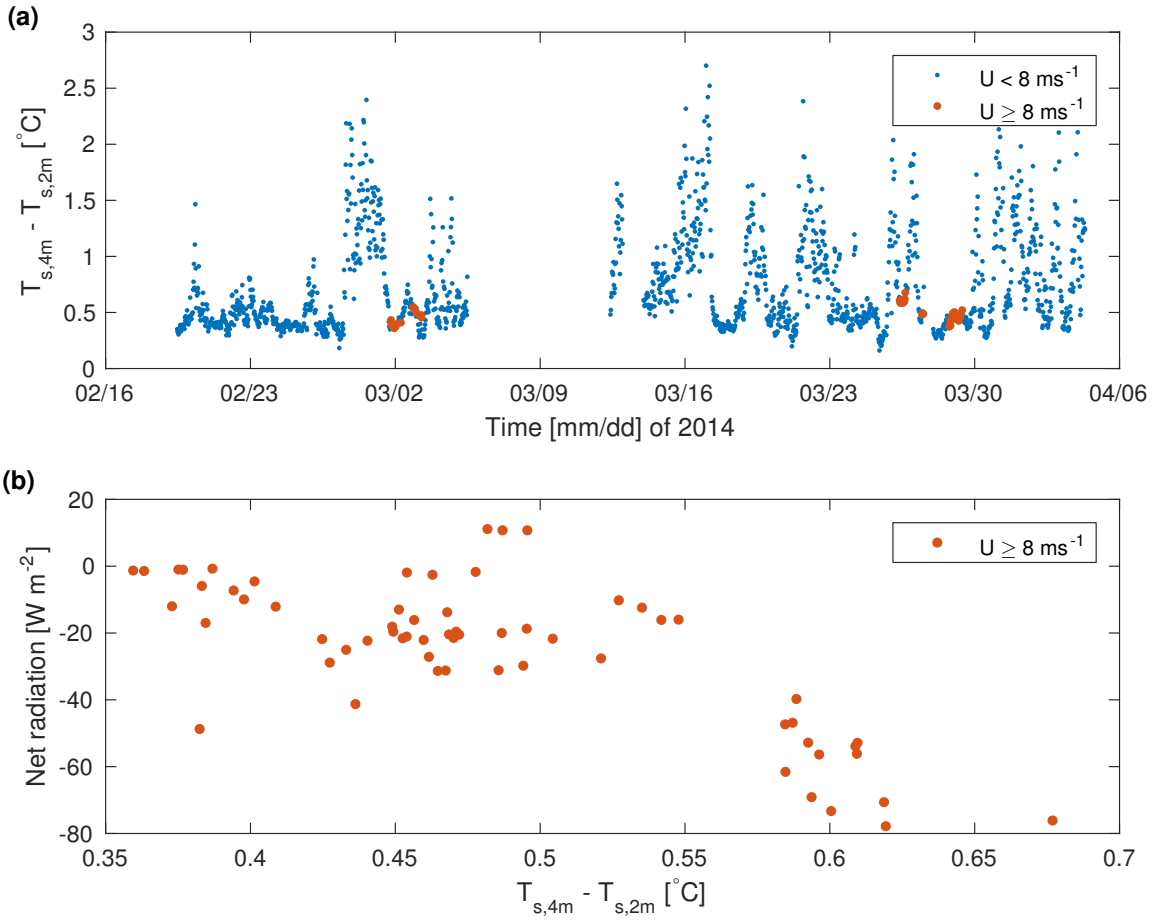

Figure 4.2: (**a**) show a time series of the temperature difference between T_s at 2 and 4 meters (**a**). The red dots shows the difference when the wind speed U $\geq$ 8 m s^{-1}. The corresponding red dots are plotted against the net radiation in (**b**).

Figure 4.2a shows the difference in sonic temperature for 2 and 4 meters. The red markers indicate situations where the wind speed is greater than 8 m s^{-1}. These are situations where we expect the difference in temperature to be approximately zero, while our measurements show it lies around 0.4°C. This indicates that the temperature sensors might not be correctly calibrated. To confirm that the difference in fact should be zero, we take a look at the radiation balance at the times where the wind is greater than 8 m s^{-1} (Figure 4.2b), which corresponds to the red dots in Figure 4.2a. Here we see that for times when the net radiation is around zero, where we would expect the temperature difference to be around zero, since the winds are relatively high, the difference in temperature is still around 0.3-04 °C. This is therefore a strong indication that the values of T_s for one or both sonic anemometers are erroneous.

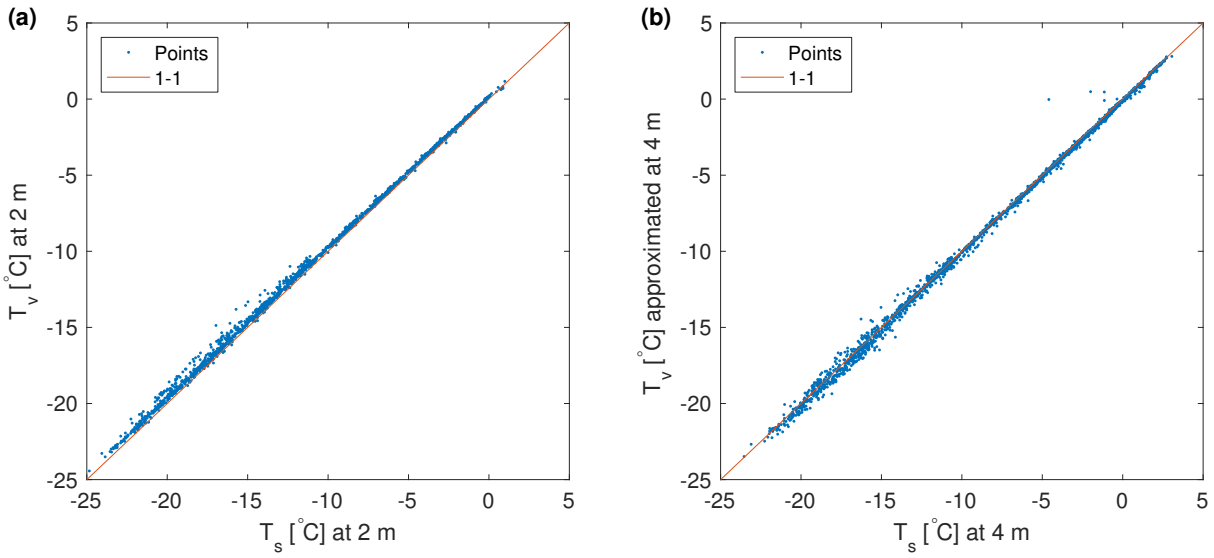

Figure 4.3: Sonic temperature plotted against the virtual temperature from the slow meteorological sensor at 2 (**a**) and 4 (**b**) meter height.

To account for this we will perform a comparison between the sonic temperatures to the slow response temperature measurements from the 10-meter-mast (Section 3.3.2). To be able to correct we assume that the temperature measurements from the slow response sensors are correct. We converted the slow response temperature measurements to virtual temperature (Equation 3.1), and compared them to the sonic temperatures, since sonic and virtual temperature is approximately the same (e.g. *Foken*, 2008). Figure 4.3a shows $T_{s,2m}$ plotted against $T_{v,2m}$. If they were equal ($T_s = T_v$) the measurements would follow the 1-1 line. We see a slight deviation towards colder values of T_s compared to T_v, for temperatures above −10°C. For even colder temperatures (T< −10°C), the scatter of the data increases. In total the 2 meter T_s seem to be systematically shifted towards colder temperatures. At 4 meter height (Figure 4.3b) the scatter is, in contrast to 2 meter, towards both colder and warmer temperatures for T< −10°C. For temperatures above -10°C there seems to be a small deviation towards warmer temperatures of T_s compared to T_v. We would therefore expect a positive correction of $T_{s,\,2m}$ and a negative correction for $T_{s,\,4m}$.

Caveats

It is of importance to mention that the slow response temperature at 4 meter is approximated. We did a linear interpolation between 2 and 10 meter height, as we did not have any measurements at the 4 meter level. This means that we have already assumed to have a linear temperature profile, which might not be the case. An other big caveat is that when the inversion layer is very shallow (lower than 10 meter) the interpolation will not be valid at all, due to a non-linear temperature profile. We are also assuming that the temperatures measured by the 10-meter mast represents the tem-

peratures at the location of the sonic anemometer. During relatively stable conditions horizontal inhomogeneity can become important, and the temperature we assume is correct might not be representative at all. It is, however, the best we can do as the raw sonic temperatures, in their current state, are unusable in calculating the correct temperature gradient. We will therefore try to find an offset value for the two temperature sensors.

Median of the offset

We will find the offset value by taking the median of the difference in the virtual temperature at 2 and 4 meters and the sonic temperature at 2 and 4 meters.

$$T_{\mathrm{corr,\,z}} = \overline{T_{\mathrm{v,\,z}} - T_{\mathrm{s,\,z}}} \tag{4.20}$$

where the bar denotes the median, and subscript z denotes the height. This gives the corrected sonic temperature:

$$T_{\mathrm{s,\,corrected}} = T_{\mathrm{s,\,z}} + T_{\mathrm{corr,\,z}} \tag{4.21}$$

The calculated offset values, for different calculation thresholds, are given in Table 4.6. Here we are using a temperature threshold, and different stability thresholds.

Table 4.6: Correction coefficients for The sonic temperature in the form of the median of the difference $T_{\mathrm{corr,\,2m}} = T_{v,\,\mathrm{2m}} - T_{s,\,\mathrm{2m}}$ and $T_{\mathrm{corr,\,4m}} = T_{v,\,\mathrm{4m}} - T_{s,\,\mathrm{4m}}$

Height	$T_{\mathbf{corr}}$	**Calculation threshold:**
2 m	0.19	$T_s \geq -10°\mathrm{C}$
	0.25	Only using finite values
	0.24	$0 < \zeta < 0.1$
	0.25	$0 < \zeta < 1$
	0.26	$0.1 < \zeta < 1$
	0.24	$-0.1 < \zeta < 0.1$
4 m	-0.10	$T_s \geq -10°\mathrm{C}$
	-0.09	Only using finite values
	-0.05	$0 < \zeta < 0.1$
	-0.08	$0 < \zeta < 1$
	-0.11	$0.1 < \zeta < 1$
	-0.05	$-0.1 < \zeta < 0.1$

In this thesis, we are focusing mainly on the stable stratification. To keep the correction simple, we want to only use one offset value, and then limit the applicability of the data calculated. If we apply a $\mathrm{T_{corr,\,2m}} = 0.25$ and $\mathrm{T_{corr,\,4m}} = -0.08$ it should be a

good fit for the values in the range $0 < \zeta < 1$. These values are not too far away from the offset values calculated using other thresholds. The applicability outside this ζ range might be somewhat limited.

Implications of the temperature correction

The temperature correction will not have any effect on the calculation of fluxes. This is because fluxes are calculated using perturbations around the mean, and shifting the mean will not effect the perturbations. When dealing with the absolute temperature, for example in the Obukhov length (Equation 2.12 and Equation 2.19) the effect is only going to be in the order of 0.1%, since the temperatures are in Kelvin. This means that the only place where it is needed to correct for the temperature offset is for the calculation of the temperature gradients. Consequently the temperature correction has only been applied on the temperature gradients (Equation 4.19) and the non-dimensional gradient for heat (Equation 2.14).

5 Dynamic stability

In this chapter we will take a look at the stability during the measurement period. It should be noted that when talking about stability in this thesis, we are referring to dynamic stability, opposed to static stability. We will discuss the different factors increasing or decreasing the stability, and find the conditions favoring a stable stratification.

5.1 Stability distribution

First we look at the stability distribution during the whole period. Table 5.1 show the stability distribution for different stability ranges. The stratification is at most times stable, with some unstable cases. The stable cases are mostly within the weakly stable/near-neutral to fairly stable range. We observe that the stability is undefined 16.7% of the time at 2 meter height, which is not ideal as this is the stability parameter used for both heights in classic MOST (Section 2.3). At 4 meter height it is only undefined 3.5% of the time. This difference is caused by a reduced availability of reliable data sets from the 2 meter sensor.

Table 5.1: The distribution of the different stability regimes, for 2 and 4 meters.

ζ **range**	**2 m**	**4 m**	**Range:**
$\zeta > 0$	77.6%	86.6%	All stable ranges
$-0.1 < \zeta < 0.1$	39.2%	30.0%	Near-neutral
$0 < \zeta < 0.1$	36.8%	28.1%	Weakly stable/near-neutral
$\zeta > 0.1$	41.0%	58.5%	Fairly stable
$\zeta > 1$	4.5%	9.1%	Very stable
$\zeta < 0$	5.6%	10.0%	All unstable ranges
$\zeta < -0.1$	2.6%	8.0%	Fairly unstable
$\zeta = \text{NaN}$	16.7%	3.5%	Undefined

Figure 5.1a and 5.1b shows histograms of the stability distribution for the whole campaign. As seen in Table 5.1 most of the measurements are within the weakly stable/near-neutral to the fairly stable range, with some very stable measurements.

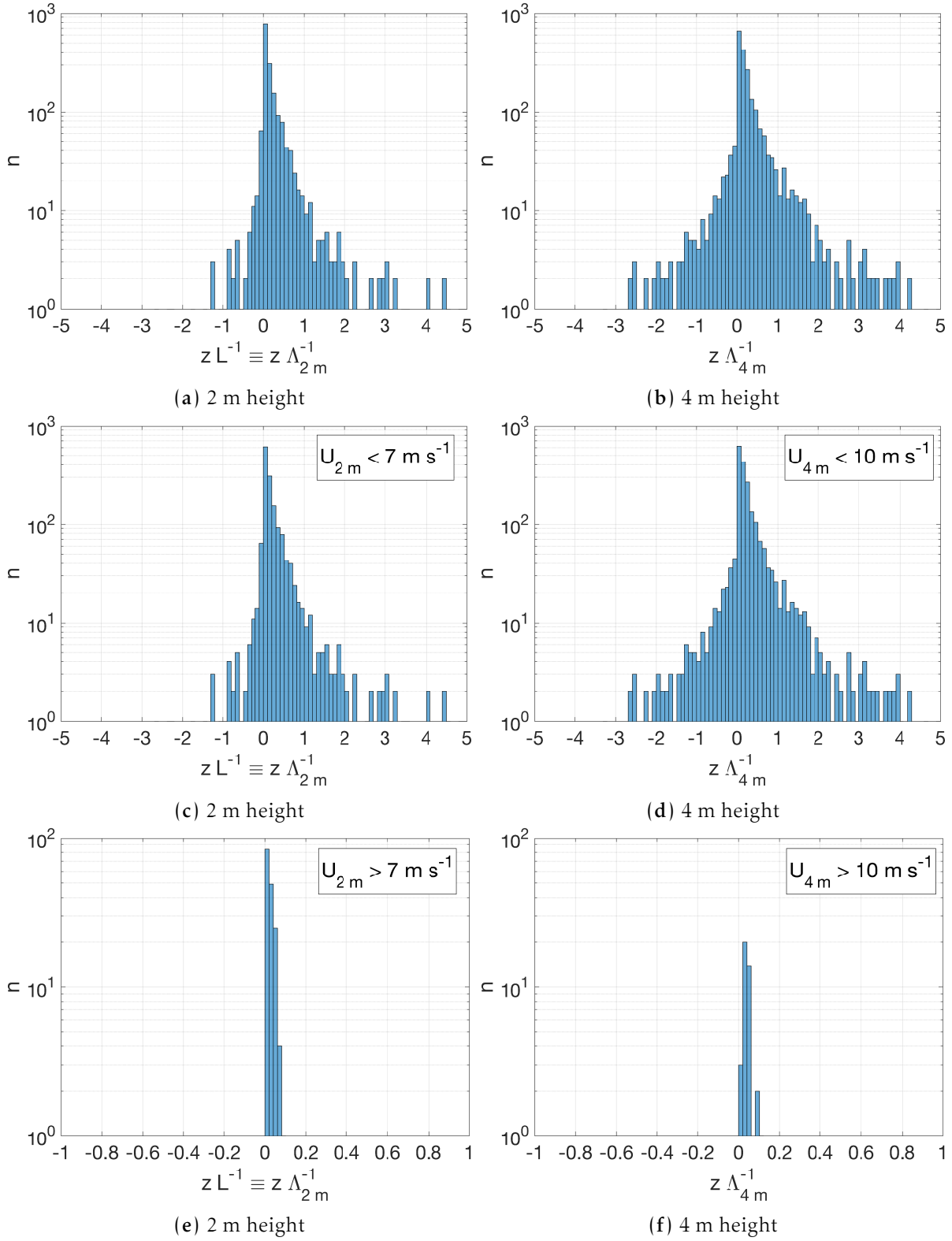

(**a**) 2 m height (**b**) 4 m height

(**c**) 2 m height (**d**) 4 m height

(**e**) 2 m height (**f**) 4 m height

Figure 5.1: Histogram of the stability parameter $z\,\Lambda^{-1}$ (at 2 m height $z\,\Lambda^{-1} = z\,L^{-1}$) during the campaign for the Sonic anemometer for all wind speeds at (**a**) 2 and (**b**) 4 meter height, for (**c**) $U_{2\,m} < 7$ m s^{-1} for 2 meter height and (**d**) $U_{4\,m} < 10$ m s^{-1} for 4 meter height, and for (**e**) $U_{2\,m} > 7$ m s^{-1} for 2 meter height and for (**f**) $U_{4\,m} > 10$ m s^{-1} for 4 meter height. The threshold is chosen for the wind speed when all stability measurements are within the near-neutral range.

There is a wider spread in the stability measurements at 4 meter compared to 2 meter, meaning that we have more observations in the range $|\zeta| > 1$ at 4 meter compared to 2 meter.

5.2 Influence of wind speed and direction

We expect the wind to influence the stability to a large degree. Higher wind speeds should induce mechanical mixing, which leads to neutral or near-neutral conditions. Figure 5.1c-5.1f shows histograms of the stability separated for wind speed. For periods with relatively high wind speeds, the wind shear generated turbulence mix the layer and develops a near-neutral stratification ($|\zeta| < 0.1$). The empirically determined wind speed thresholds for near-neutral conditions are $U_{2\,m} < 7$ m s^{-1} and $U_{4\,m} < 10$ m s^{-1} for 2 and 4 meter height, respectively. This means that when the wind speed for the two different heights exceeded these thresholds, the stabilities were, at all times, within the near-neutral range (Figure 5.1e and 5.1f).

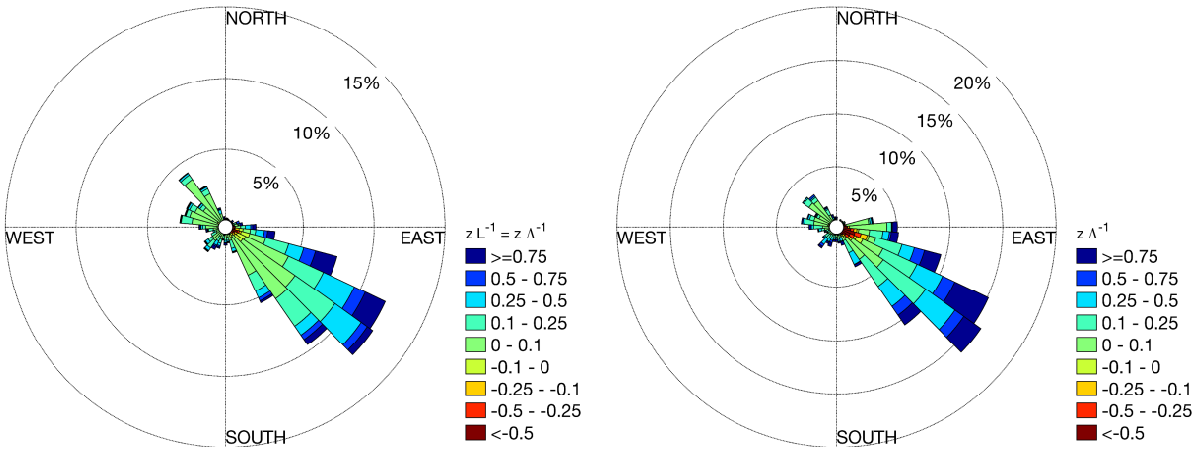

(**a**) 2 m height (**b**) 4 m height

Figure 5.2: Stability rose for Adventdalen at (**a**) 2 m and (**b**) 4 m height, where histograms of the stability parameter z L^{-1} and the local stability parameter z Λ^{-1} are plotted against wind direction.

Wind direction could also play a large role, due to advection effects. Since we are in a valley, relatively close to the entrance, we have two main wind directions, wind from within the valley, and wind entering the valley. Measurements do not represent the properties at the location of the instrument, but rather a certain distance upwind of the instrument; the so called footprint area (e.g *Foken*, 2008). The effect is that for a change in wind direction, the measured properties could change significantly because the air measured still has properties from a different type of surface (rougher surface, open water, etc.). The surface heterogeneities can be described as non-ideal conditions, compared to ideal conditions on a homogeneous surface (e.g. sea ice with no nearby

terrain). The fetch is the upwind distance from the surface change. Measurements needs to be taken at a distance far enough from the surface change in order to know that you are actually measuring the local field (e.g *Stull*, 1988).

If the two main wind directions we see represent air masses we expect this to potentially have an effect on the stability. Figure 5.2 is like a wind rose, but for the stability parameter derived from MOST instead of the wind speed. We see that for the most stable conditions measured (z $L^{-1}$and z $\Lambda^{-1} > 0.5$) we have SE wind, which is from within the valley. The unstable stratification happens also mostly with SE wind. There is an unstable stratification only 1-3% of the time with NW wind, while it happens between 9-13% of the time with SE wind. This is the same direction as were the most stable stratifications occur. For NW wind the wind is fairly stable ($\zeta > 0.1$) 25-39% of the time, and 55-68% of the time for SE wind. This leads us to the conclusion that the stability is affected differently by the different air masses from within the valley, and the one coming from Adventfjorden.

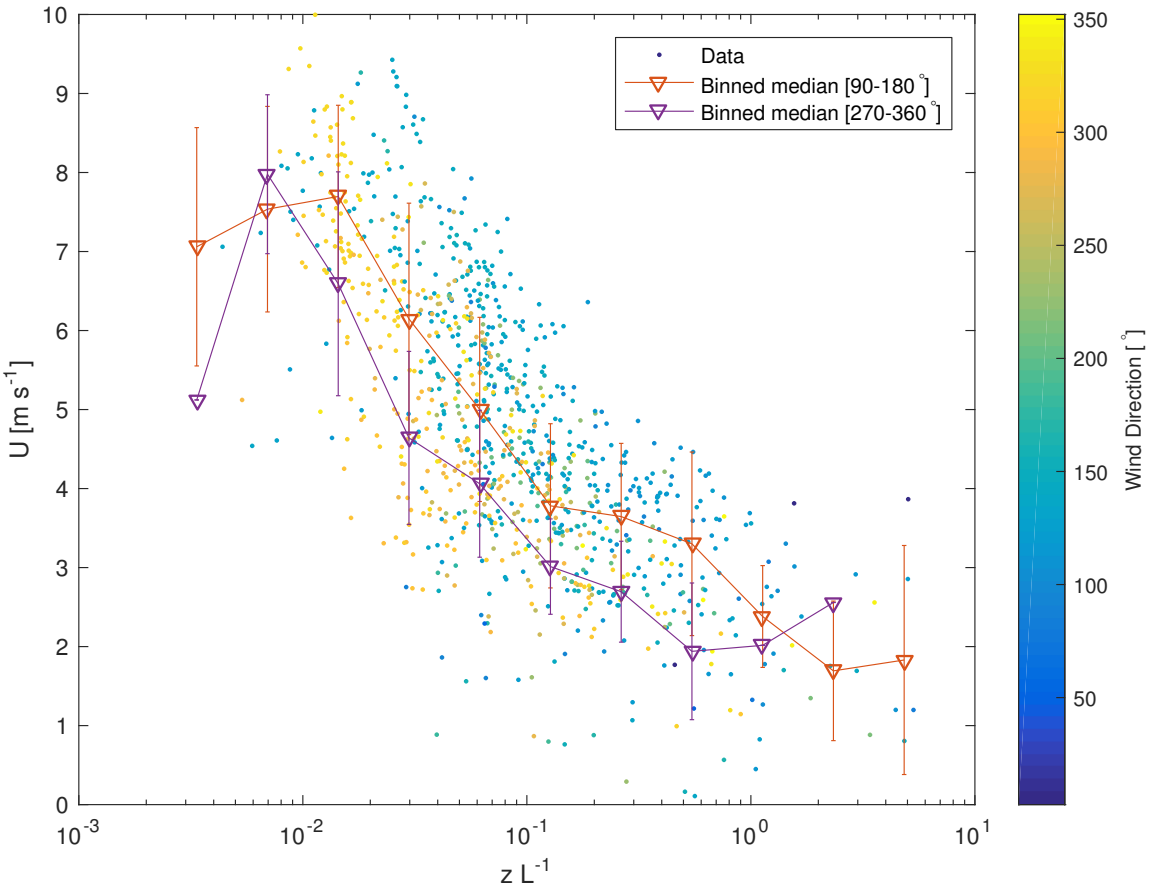

Figure 5.3: The wind speed U plotted against the stability parameter ζ = z L^{-1} = z Λ^{-1} at 2 meter height. The colors on the markers indicates the wind direction. The red line indicates the median for values with SE wind binned for different stabilities, also showing the standard deviation. The purple line shows the same for NW wind.

To investigate this further we take a look at the stability distribution for different wind speeds and directions. Figure 5.3 shows a scatter plot between the wind speed

and the stability parameter ζ, with wind direction presented as color coding. It also shows the binned median of the relationship using different wind direction thresholds. The red line represents wind from within the valley (SE) and the purple line represents wind from Adventfjorden (NW). We see that for higher wind speeds we get lower stabilities, and for lower wind speeds we have a potential for higher stabilities, just like we saw in Figure 5.1. A distinct directional dependency for the stability is also seen, for the same wind speeds. The binned medians for NW and SE wind show that for the same wind speed, the ABL is less stable for wind coming from Adventfjorden (NW) compared to the opposite direction. This indicates that we have two different types of air masses from the two different directions, and this might be because NW wind comes from an open fjord. When we reach the very stable range ($z\,L^{-1} > 1$) the dependence of wind speed and direction seems to weaken (for $U < 2$ m s^{-1}), but there are too few observations in this range to make any conclusions.

5.3 Influence of radiation

As mentioned before the main mechanism for the creation and maintenance of a SBL is a negative net radiation balance. We will therefore try to a connection between the radiation measurements and the stability.

Figure 5.4 shows the stability dependence on the net radiation, with wind speed as color coding. When looking only at the blue line, which indicates relatively high wind speeds ($U > 7$ m s^{-1}), there are low values of stability, as shown in Section 5.2. We also see a tilt in the blue line, meaning that the more negative net radiation the more stable the the air is. There seems to be a stability maximum for this wind speed range at $z\,L^{-1} \approx 0.06$, when looking at the binned medians.

For wind speeds in the middle range (4 m s^{-1} $< U <$ 7 m s^{-1}) seen in the purple line, the same tendency is seen. The more negative net radiation, the higher stabilities we get. After $z\,L^{-1} > 0.15$ the tendency flattens out. The red line is the median for calm conditions ($U < 3$ m s^{-1}), which has the same tendency as the previous wind speed ranges. Yet again the median flattens out, this time at about $z\,L^{-1} > 0.25$. The reason for this flattening is hard to determine. It could be that the effect of net radiation is limited, for the different wind speed ranges, at a certain stability threshold, or it is just too few observations in this stability range. The standard deviations are also quite big at this point, making it hard to say something with confidence.

The biggest difference between the different wind ranges is that the net radiation needed in order to get the same stabilities are larger for higher winds. In order to achieve a stability of $z\,L^{-1} \approx 0.06$ a net radiation of -70 W m^{-2}, -35 W m^{-2} and -10 W m^{-2} for high winds ($U >$ 17 m s^{-1}), middle range winds (4 m s^{-1} $< U <$ 7 m s^{-1}) and calm conditions ($U <$ 4 m s^{-1}), respectively. It is also seen that the stability in-

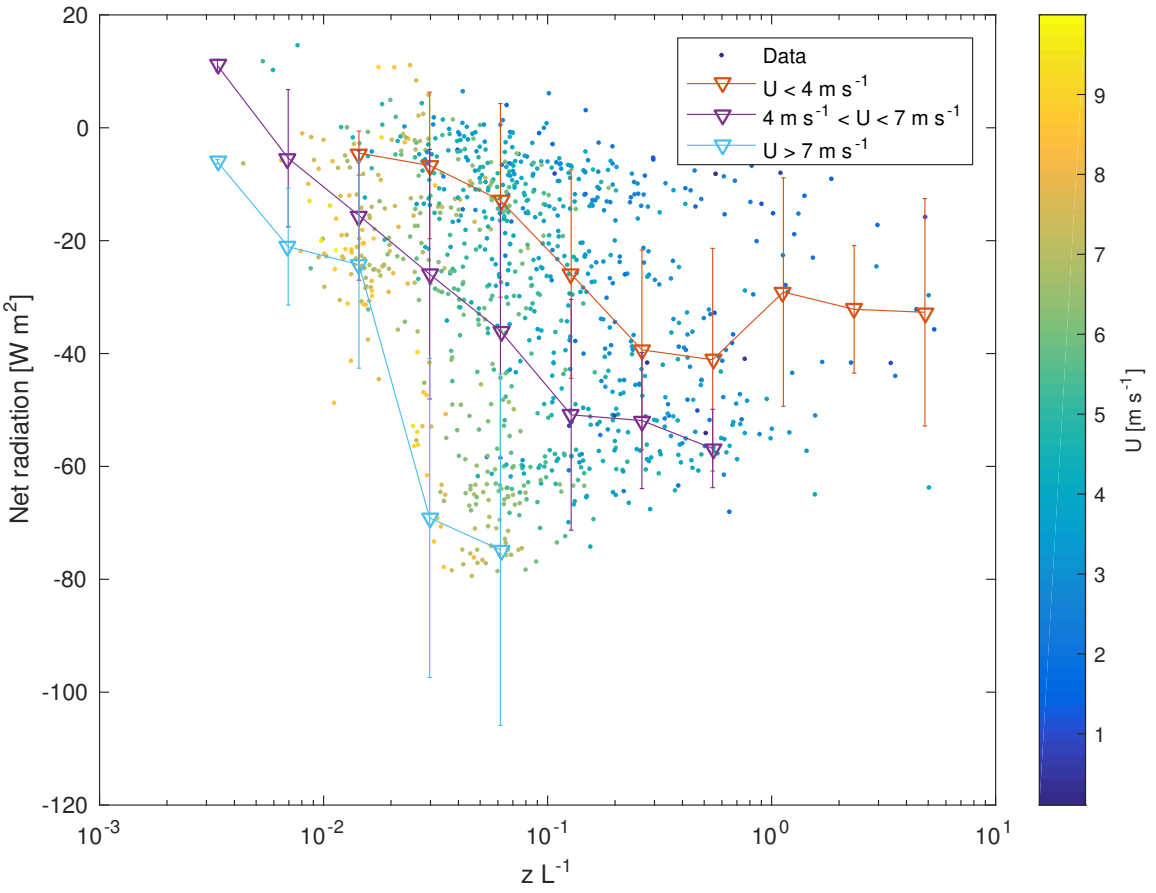

Figure 5.4: Scatter of the stability parameter $\zeta = z\,L^{-1} = z\,\Lambda^{-1}$ against the net radiation at 2 meter height. The color on the markers indicate the wind speed. The binned medians for different ranges in wind speed are also shown; the red are for $U < 4$ m s^{-1}, purple line for 4 m s^{-1} $< U < 7$ m s^{-1} and the blue line is for $U > 7$ m s^{-1}.

creases at a higher rate for increasing net radiation when there is calm and medium range wind conditions, compared to relatively high wind speeds.

5.4 Discussion

The stabilities seems to have a tendency to be distinctly stronger, both on the stable and unstable side, at 4 meter height, compared to 2 meter height. The same tendency is seen when looking at the full time series in Appendix A.1. As most of our measurements are in stable range ($z\,L^{-1} > 0$), we do not discuss any further than this on the unstable conditions.

We see also that we have a clear trend for the stability with wind speed. Higher wind speeds cause turbulent mixing, which leads to a shift towards neutral conditions. This is what we would expect. We found the wind-speed threshold for near-neutral conditions at $U_{2\,m} \approx 7$ m s^{-1} and $U_{4\,m} \approx 10$ m s^{-1}. There is also a clear dependency of the wind direction. When looking at data from the 2 meter sonic anemometer (Figure 5.3), we see that higher wind speeds lead to less stable conditions, but the stabilities

are generally higher for SE wind compared to NW wind, for the same wind speed. It leads to the conclusion that the two main wind directions advect different air masses, and that SE favors relatively higher stabilities compared to NW wind. This is not unexpected as NW wind has its source in Adventfjorden, where the air mass is exposed to advection from the relatively warm water.

The net radiation was also found to be important. Figure 5.4 shows a trend for higher stabilities during strong negative net radiation. This is in accordance with the assumption that one of the main drivers of the SBL is a negative radiation balance at the surface. It is also seen that net radiation alone does not cause very stable conditions, and that calm conditions are another requirement to get high stabilities.

It is concluded that the main drivers for the stability in Adventdalen are the wind speed, the wind direction and the surface radiation balance. Calm conditions with weak SE wind and strong negative net radiation are favorable for very stable conditions.

6 Scaling

6.1 Heat flux

It has been shown that the downward heat flux in the stable boundary layer increases with higher stability, until it reaches a point where it starts to decrease (*Derbyshire*, 1990, e.g.). Different values for the maximum of the downward heat flux have been found. *Malhi* (1995) found it at $\zeta = 0.2$, *Mahrt et al.* (1998) found it at $\zeta \approx 0.06$ for measurements at 10 meter height, and at $\zeta \approx 0.02$ at 3 meter height. *Grachev et al.* (2005) found it at $\zeta \approx 0.025$ using classic MOST (Section 2.3), and at $z\,\Lambda^{-1} \approx 0.02$ for 2.2 meters and at $z\,\Lambda^{-1} \approx 0.1$ for their highest level (≈18.4 or 14 m) using local scaling (Section 2.3). This heat flux maxima is found to be the separation between the weakly stable (surface based scaling regime) and the transition regime (*Mahrt et al.*, 1998), mentioned in Section 2.3.

Figure 6.1 shows the buoyancy flux plotted against different stability parameters, the flux Richardson number (Rf), and the surface based ($z\,L^{-1}$) and local scaling parameter ($z\,\Lambda^{-1}$). We see that the maximum negative heat flux for the binned medians occur at $z\,L^{-1} \approx z\,\Lambda_{2\,m}^{-1} \approx Rf_{2m} \approx 0.007$, except for the flux Richardson number and the local stability parameter at 4 meter height, where this minimum is located at $Rf_{4m} \approx z\,\Lambda_{4\,m}^{-1} \approx 0.015$. This is almost of the same magnitude as the values found by *Mahrt et al.* (1998) and *Grachev et al.* (2005), but one order of magnitude lower than the value reported by *Malhi* (1995). *Mahrt et al.* (1998) found that the downward heat flux maxima defined the separation from the surface layer scaling regime to the transition regime. This indicates that the transition regime starts at $\zeta \approx 0.01$ in our dataset, as this is the location of the downward heat flux maxima, and MOST using the local stability parameter $z\,\Lambda^{-1}$ should give better results for more stable conditions.

Figure 6.1 does not show this behavior. In classical MOST the fluxes should be independent of height, for the same stabilities. The median of the buoyancy flux is closer together when plotted against the surface based stability parameter, $z\,L^{-1}$ compared to the local stability parameter $z\,\Lambda^{-1}$. This is the case until around $z\,L^{-1} \approx 0.3$. From there local scaling works better, but for very stable cases ($z\,\Lambda^{-1} > 1$) it separates again, but this might be because we have too few observations in this range, or that other

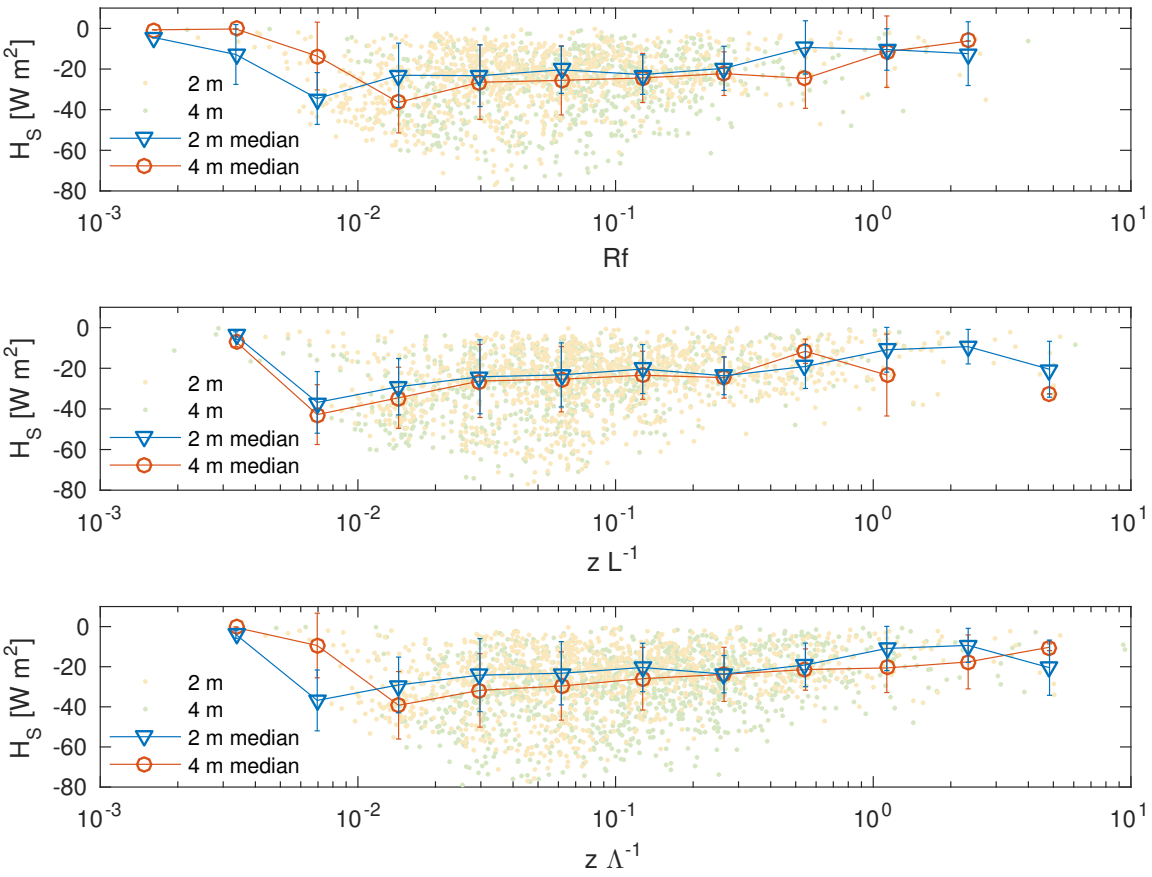

Figure 6.1: The buoyancy flux (H_s) plotted against the Flux Richardson number (Rf), the surface based stability parameter z L^{-1}, and the local stability parameter z Λ^{-1}.

effects become important.

Classic MOST seems to be a better fit than MOST based on local scales until z $\Lambda^{-1} \approx 0.3$, which is not what we would expect if the limit of the transition regime is defined by the maximum downward heat flux. The limits for the transition regime found by *Grachev et al.* (2005), where $\zeta > 0.1$, seems to be more in accordance with our results, but they found the maximum downward heat flux at this point as well, as opposed to our maximum one order of magnitude lower. This could be because we do not have any measurements higher up, as the downward heat flux maxima is shifted to the right for the second lowest measurement (~ 3.2 meters) in *Grachev et al.* (2005), but their 5.1 meter measurement has the maxima on the same location as the rest of the heights, at $\zeta \approx 0.1$.

For the most part, our results are in agreement with *Grachev et al.* (2005). The downward heat flux maxima is located at lower stabilities, but as mentioned before, this could possibly be because we do not have any measurements at larger heights. When using local scales, the heat flux maxima is shifted to the right for the 4 meter data (2 meter heat flux is unaffected by definition). Both *Mahrt et al.* (1998) and *Grachev et al.* (2005) found the downward heat flux maxima at lower stabilities for the lower heights, compared to the measurements higher up. The direction of the shift of the

maxima is in the same direction as in *Grachev et al.* (2005), meaning that if we would have measurements higher up, we might have had a downward heat flux maxima at higher stabilities at these heights. Since local scales do not work significantly better until $\zeta \approx 0.3$, we would expect the transition regime to start around here, based on Figure 6.1. A regime boundary at $\zeta \approx 0.3$ is not far from the results from *Grachev et al.* (2005), where they found the transition regime to start at $\zeta \approx 0.1$.

6.2 Momentum flux

Figure 6.2 shows the momentum flux in the form of the frictional velocity, u_*, plotted against different stability parameters. Like for the buoyancy flux, the momentum fluxes are the same for the two heights using classic MOST. The binned median of u_*, with respect to stability, has a clear deviation between u_* at the two heights, when using the local scaling parameter z Λ^{-1} compared to the surface based stability parameter z L^{-1}. This is a indication that classic MOST represent the momentum flux better than MOST with local scaling, at least up to around $\zeta \approx 1$.

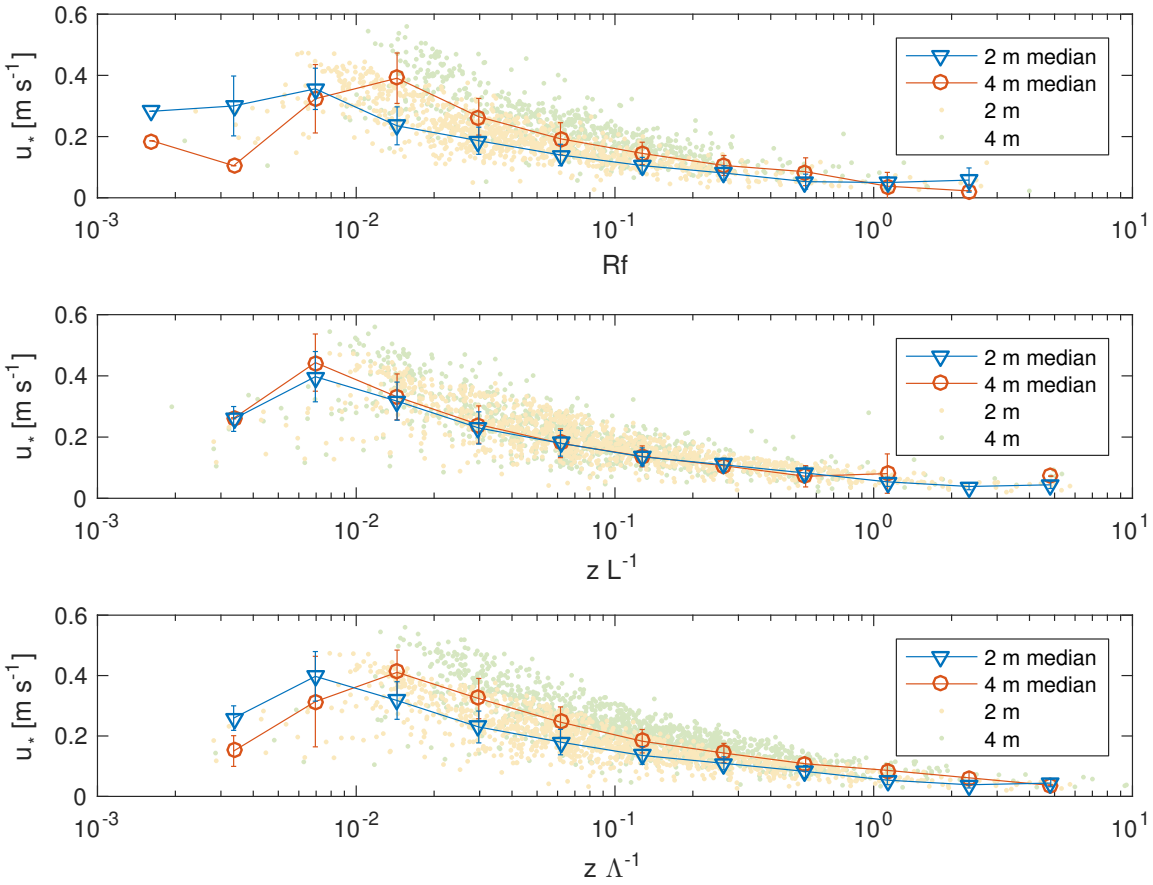

Figure 6.2: The friction velocity (u_*) plotted against the Flux Richardson number (Rf), the surface based stability parameter z L^{-1}, and the local stability parameter z Λ^{-1}.

6.3 The flux Richardson number

A "critical" flux Richardson number, where turbulence growth is suppressed, is found as $\mathrm{Rf_{cr}} \approx 0.2 - 0.25$ (e.g *Zilitinkevich et al.*, 2010), which should not not be confused with the classical critical Richardson number ($\mathrm{Rf_c} = 1$), which tells where turbulence changes to a quasi-laminar and non-turbulent state (e.g. *Foken*, 2008). *Galperin et al.* (2007) and *Grachev et al.* (2013) found the Richardson number to be an inappropriate threshold for when turbulence is suppressed.

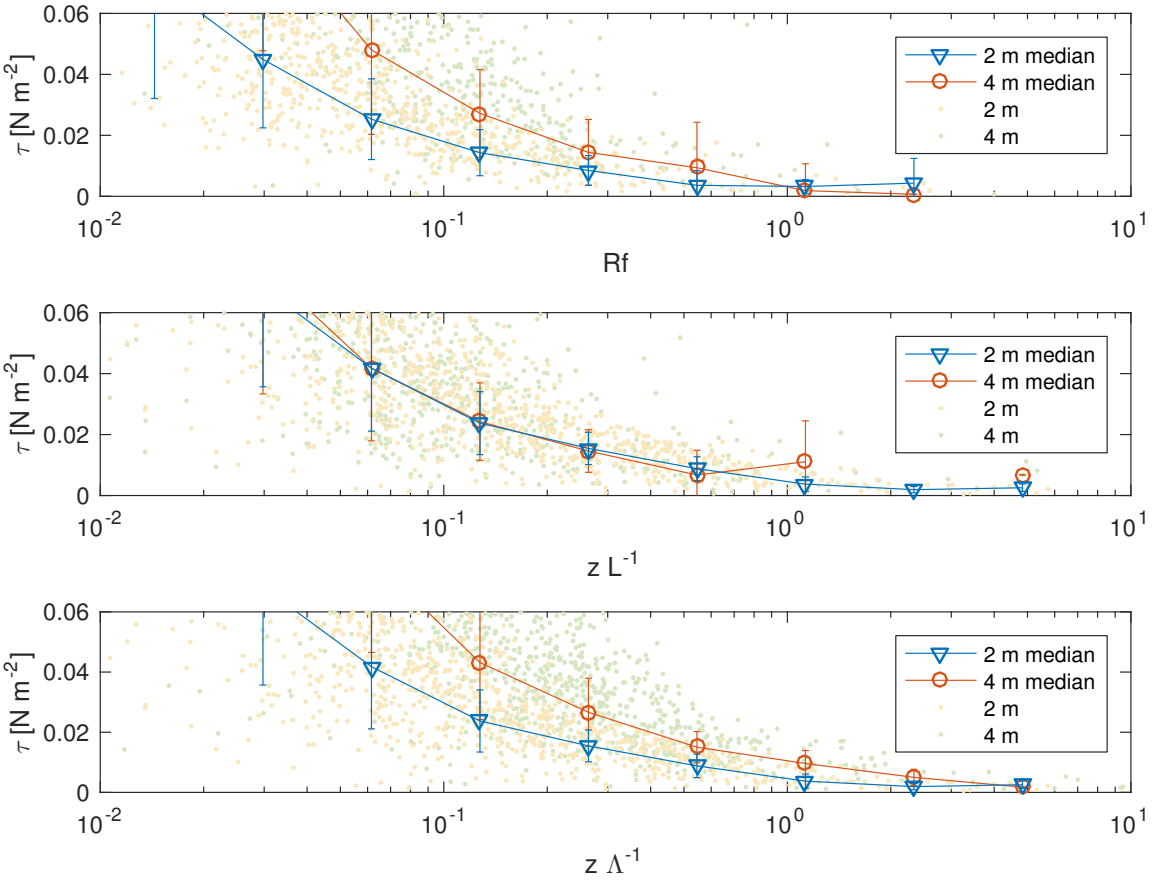

Figure 6.3: The friction velocity (u_*) plotted against the Flux Richardson number (Rf), the surface based stability parameter z L^{-1}, and the local stability parameter z Λ^{-1}.

Figure 6.3 is the same as Figure 6.2 but using τ as the momentum flux, and looking only at the momentum fluxes in the smaller range. The use of τ is chosen by comparability reasons with Figure 5 in *Grachev et al.* (2013). When looking at the flux Richardson number, we do not see a clear point where the momentum flux is suppressed. Our fluxes are in the same range as *Grachev et al.* (2013), but they do not die out as quickly for $\mathrm{Rf} > \mathrm{Rf_{cr}} \approx 0.2$. The fluxes are persisting for $\mathrm{Rf} \leq O(1)$, where they cease to exist, but as the number of measurements is low, it is hard to say something exact. It should be mentioned that we have not, in contrast to *Grachev et al.* (2013), filtered out large-scale features in our measurements, meaning that some of the momentum fluxes can contain contributions from larger scales.

We also do not see any flux Richardson number threshold for suppressed turbulence, which is in agreement with *Galperin et al*. (2007) and *Grachev et al*. (2013). We see the same behavior for the buoyancy flux (Figure 6.1), where we have small downward heat fluxes up to $Rf > 2.3$, where we no longer have any observations.

Grachev et al. (2013) did find the critical flux Richardson number to be an upper threshold for the applicability of local scaling. $Rf > Rf_{cr}$ at 12% and 19% at the time, at 2 and 4 meter height, respectively. We do not see any clear upper boundary for the applicability of local scaling, in our data, for reasons that will be discussed in the next section. A inferior boundary is not seen as well, as surface based scaling performs better than local based scaling for the momentum flux (Figure 6.2-6.3), and the same is true for the buoyancy flux up to $z\,L^{-1} \approx 0.3$. Surface based scaling seems therefore to generally perform better when looking at both fluxes. The upper boundary of the transition regime, where local scaling should perform better, will be discussed next.

6.4 Influence of Coriolis

When the Coriolis force is a significant driver of the wind, features related to an Ekman spiral have been found by e.g. *Grachev et al*. (2005). This is related to the turbulent Ekman layer mentioned in Section 2.3, where the fluxes are small and the vertical structure of the wind is highly influenced by the Coriolis force (*Grachev et al*., 2005). Neither surface based or local based MOST are able to adequately describe the turbulence in this regime, and it is therefore important to identify if we have any periods under this regime in our observations.

In Figure 6.4 we see the difference in wind direction at 4 and 2 meter height. After calculating the mean there was a 3.4° deviation from 0 for all stabilities. This is not physical, as we do not expect the net effect from Coriolis to be the same for all stabilities, and we attribute this difference to the accuracy of the orientation of two the sonic anemometers. The mean of the deviation was therefore subtracted, before plotting the angle deviation in Figure 6.4. The difference is then around zero at stabilities up to $\zeta = z\,L^{-1} \approx 1$ This indicates that the effect from the earths rotation is negligible approximately up to this point. To confirm this, we plotted the Ekman number at 4 meter height against the stability parameter $z\,\Lambda^{-1}$, seen in Figure 6.5. The Ekman number is a non-dimensional ratio comparing the frictional force and the Coriolis force. This means that the Coriolis force has the most important significance when $Ek > Ek_{cr} \approx 1$. The median of the Ekman number is above 1 at all times, with a few Ek outliers below 1. At $z\,\Lambda^{-1} \approx 3$ the surface forcing is twice as important as the Coriolis, for the median. Some outliers are seen, but when comparing Figure 6.4 and Figure 6.5 we can say that Coriolis is negligible for $\zeta < O(1)$ which is in agreement with *Grachev et al*. (2005), and that the Turbulent Ekman layer (Section 2.3) is nearly not present in our dataset.

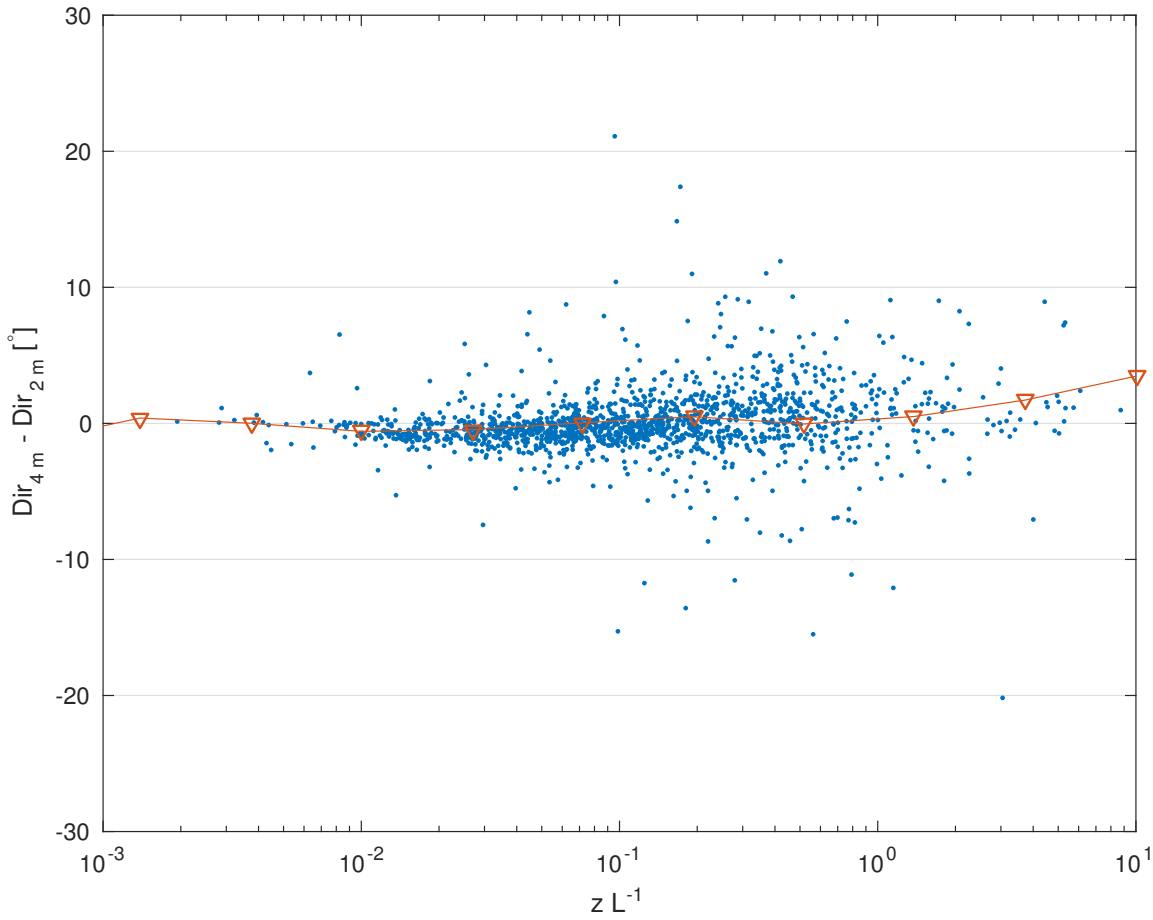

Figure 6.4: The difference in wind direction at 4 meter vs 2 meter height. We have subtracted the mean of the difference (3.4°) because of errors in the orientation of the sonic. The red line indicates the binned median with respect to stability.

This means that our data are dominated by the Surface layer scaling regime and the Transition regime, with nearly no occasions where higher stability scaling regimes are applicable.

This indicates that there is probably no upper boundary for the applicability of local scaling, or the transition regime, in our data. The surface layer scaling regime seems to be the important boundary, in order to look for the applicability of local scaling in our data set. As discussed in the previous section, surface based scaling seems to perform better in general when looking at the fluxes in our data.

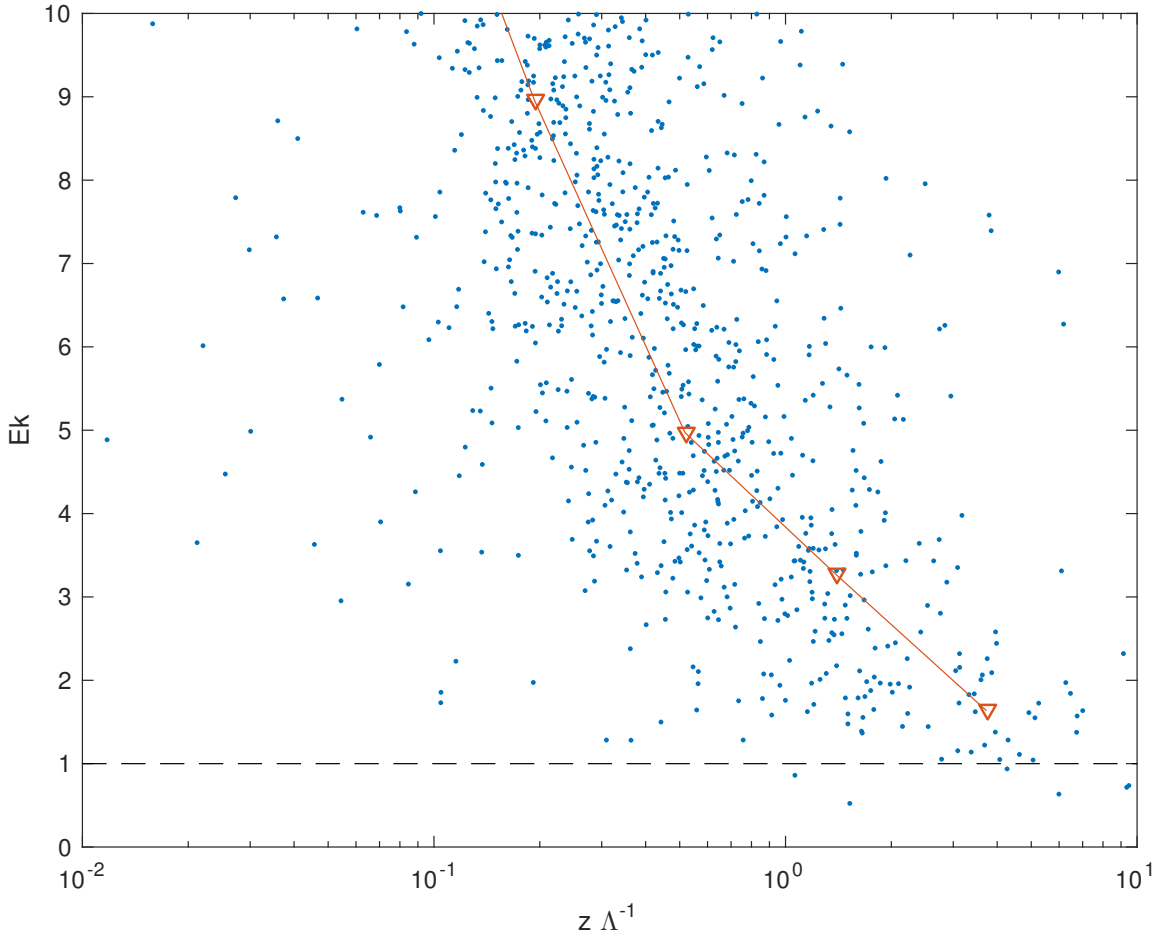

Figure 6.5: The Ekman number at 4 meter height plotted against the local stability parameter $z\,\Lambda^{-1}$. The red line shows the binned median of Ek with respect to stability.

7 Gradients

When calculating the non-dimensional profiles in MOST (Equation 2.13-2.14), they will be sensitive to errors in the estimate of the vertical wind and temperature gradients. An overestimated gradient will lead to a too large non-dimensional gradient (ϕ), and vice versa for an underestimation. The inaccurate estimation of the gradient might be different for different stabilities, as the gradient is dependent on the stability (Equation 2.17). In the following sections we will present the calculated non-dimensional profiles, and discuss the implications of a flawed representation of the vertical wind and temperature gradient, before comparing our results with empirically found parameterizations of the non-dimensional gradients.

7.1 The non-dimensional momentum profile

As just stated, an inaccurate representation of the vertical wind gradient, will have an implication on the accuracy of the non-dimensional gradient. We will for this reason investigate the sensitivity of the choice of the vertical wind gradient, to the calculation of the non-dimensional profile of momentum (or the non-dimensional gradient of momentum). A logarithmic wind profile will be investigated first, before examining a second order logarithmic profile, and several linear profiles.

Figure 7.1 shows the non-dimensional gradient of momentum (ϕ_m) plotted with respect to the surface based stability parameter ($\zeta = z\ L^{-1}$) and the local based stability parameter ($\zeta = z\ \Lambda^{-1}$). It shows each 30 minute average as yellow and green dots for 2 and 4 meter height, respectively, and the binned median of ϕ_m with respect to the stability parameter, ζ, for 2 meter (blue line) and 4 meter height (red line). Surface based scaling in MOST (Section 2.3) is applied for the top plot, while local based scaling in MOST is used for the bottom plot. The **black line** shows the universal function by *Högström* (1996) where

$$\phi_m^{\mathrm{H96}} = 1 + 5.3\zeta \tag{7.1}$$

and the **dashed line** shows the universal function developed by *Grachev et al.* (2007)

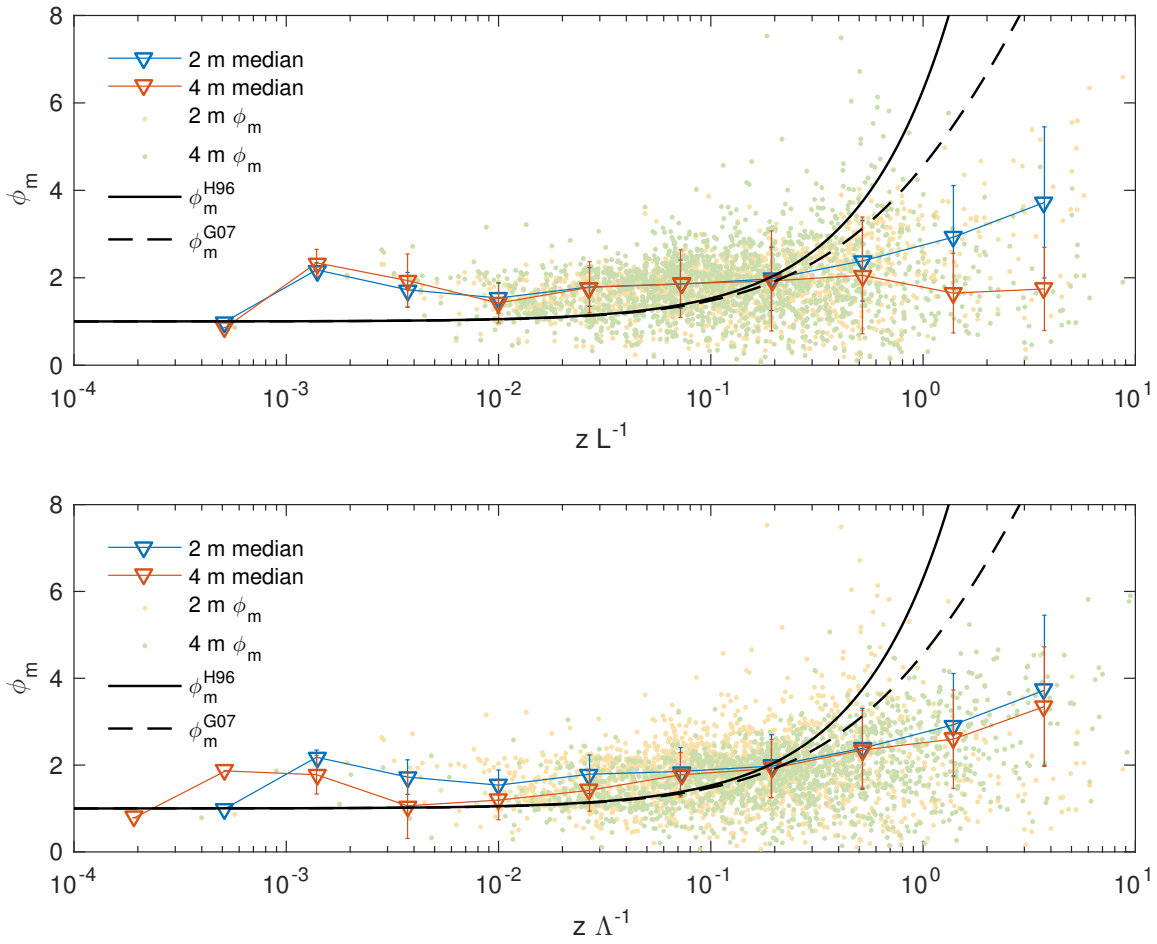

Figure 7.1: The non-dimensional gradient of momentum ϕ_m, using a first order logarithmic fit to calculate the wind gradient, plotted against the surface based stability parameter $\zeta = z\ L^{-1}$, and the local stability parameter $\zeta = z\ \Lambda^{-1}$. The red and blue line shows binned medians with standard deviation at 2 and 4 meter height, and the yellow and green markers shows all 30-minute averaged measurements. The **black** line represents universal function from *Högström* (1996) (Equation 7.1), and the **dashed line** are the universal function developed by *Grachev et al.* (2007) using the SHEBA data (Equation 7.2) . The bins are logarithmically distributed in respect to $z\ \Lambda^{-1}$.

using the SHEBA data where:

$$\phi_m^{G07} = 1 + \frac{6.5\zeta(1+\zeta)^{1/3}}{1.3+\zeta} \tag{7.2}$$

The wind gradient is calculated according to Section 4.2.1, fitting the wind profile logarithmically (Equation 4.15).

The calculated non-dimensional gradients overestimate, compared to the universal function, by around 1 for $\zeta < 0.2$ at both heights when using the surface based stability parameter $\zeta = z\ L^{-1}$. This overestimation is slightly lower for the 4 meter height when using the local stability parameter $\zeta = z\ \Lambda^{-1}$. For $\zeta > 0.2$ there is an underestimation, which is quite far from both the universal functions. The medians of ϕ_m are very close together for the two heights when using the surface based stability parameter $\zeta = z\ L^{-1}$ until $\zeta \approx 0.2$ where they separate. For $\zeta > 0.2$, ϕ_m, for the two heights, are much closer

together when using the local stability parameter $\zeta = z\,\Lambda^{-1}$. If the non-dimensional gradients should be constant with height at a given stability, the use of surface based scaling in MOST (Section 2.3) works good up until $\zeta \approx 0.2$ where local scaling gives a better height-independent relationship.

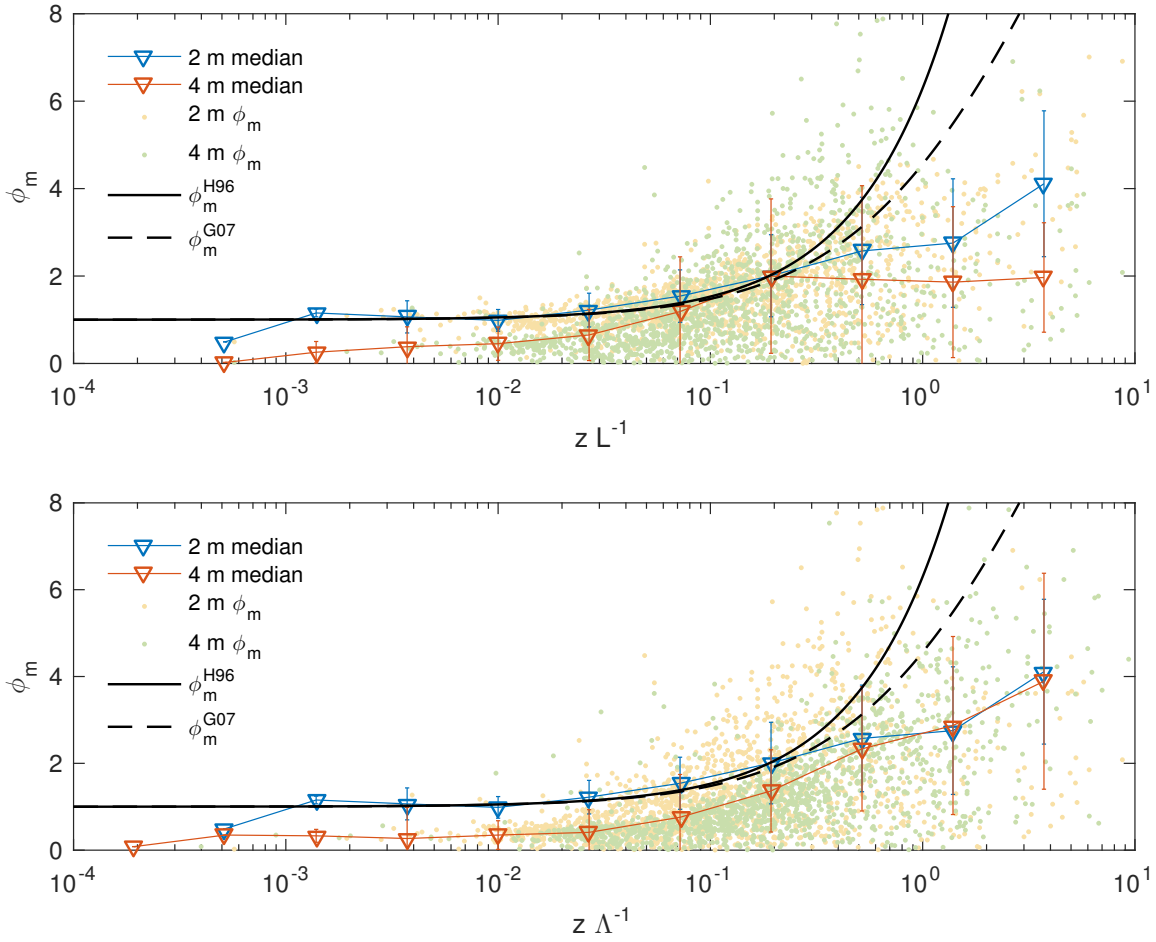

Figure 7.2: The non-dimensional gradient of momentum ϕ_m, using a second order logarithmic fit to calculate the wind gradient, plotted against the surface based stability parameter $\zeta = z\,L^{-1}$, and the local stability parameter $\zeta = z\,\Lambda^{-1}$. The red and blue line shows binned medians with standard deviation at 2 and 4 meter height, and the yellow and green markers shows all 30-minute averaged measurements. The **black** line represents universal function from *Högström* (1996) (Equation 7.1), and the **dashed line** are the universal function developed by *Grachev et al.* (2007) using the SHEBA data (Equation 7.2) . The bins are logarithmically distributed in respect to $z\,\Lambda^{-1}$.

Grachev et al. (2005) found quite a good relationship between the empirical and calculated non-dimensional profiles. They used a second order logarithmic fit to the wind profile, while we, in Figure 7.1, used a first order logarithmic fit. We have therefore plotted for a second order logarithmic fit to the wind gradient using the matlab function *polyfit* to find the gradient in the form of:

$$u(z) = A \ln z^2 + B \ln z + C \tag{7.3}$$

where we get coefficients for A, B and C for each time step, which gives the gradient

$$\frac{du}{dz} = \frac{2A \ln z}{z} + \frac{B}{z} \tag{7.4}$$

Figure 7.2 is the same as Figure 7.1 but using a second order logarithmic gradient (Equation 7.4). This gradient performs well on the 2 meter data, where it is in line with the empirical universal functions, while it underestimates at 4 meter height. It has more of a spread between the two heights, compared to when we are using a first order logarithmic gradient (Figure 7.1). The performance is equally good using a first and second order logarithmic gradient in calculating ϕ_m for higher stabilities (z $L^{-1} > 0.5$).

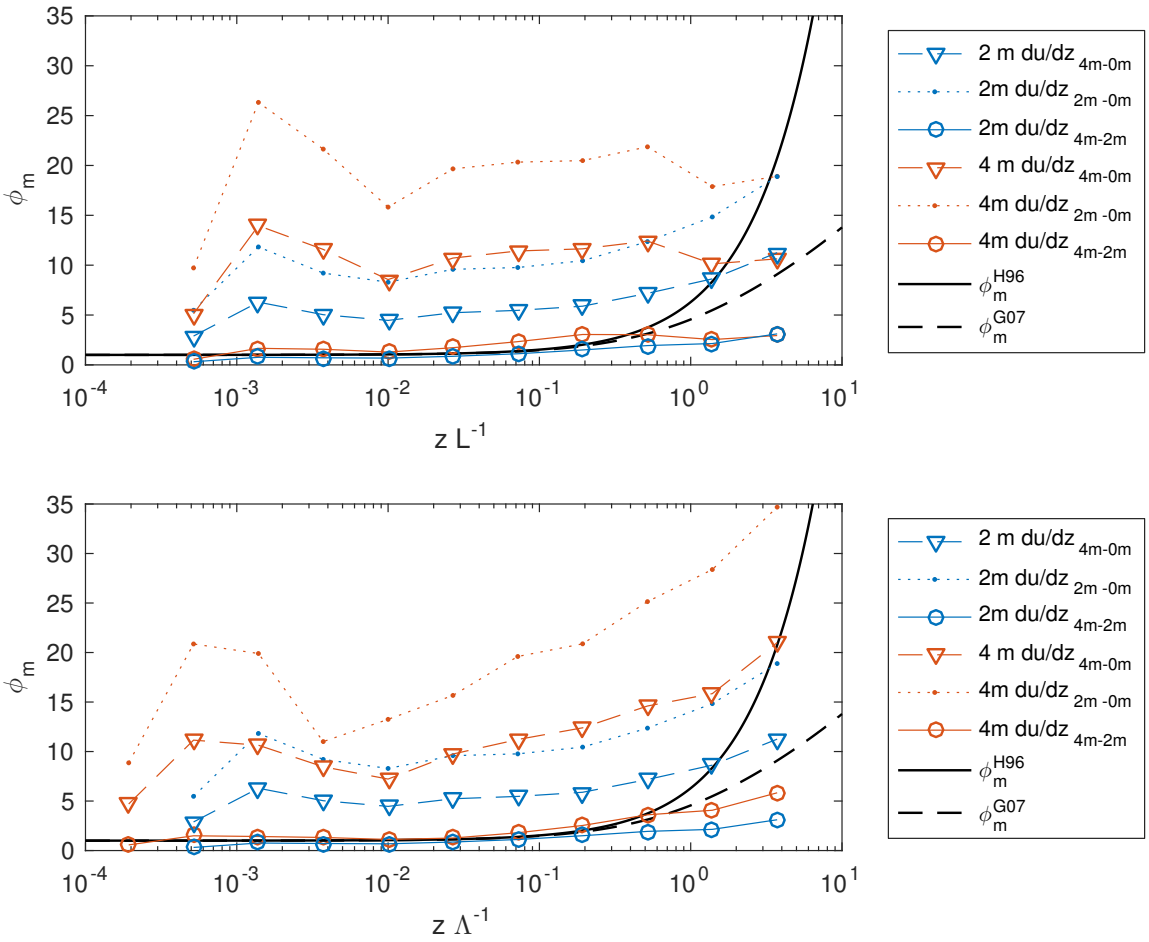

Figure 7.3: The non-dimensional gradient of momentum ϕ_m plotted against the surface based stability parameter ζ = z L^{-1}, and the local stability parameter ζ = z Λ^{-1}. The red and blue line shows binned medians at 2 and 4 meter height, respectively. The *dashed lines* are using a linear gradient calculated between 4 and 0 meter height, the *dotted lines* are using a linear gradient between 2 and 0 meter height, and the *normal lines* is the gradient between 4 and 2 meter height, using Equation 4.13. The **black** line represents the universal function from *Högström* (1996) (Equation 7.1), and the **dashed black line** are the universal function developed by *Grachev et al.* (2007) using the SHEBA data (Equation 7.2) . The bins are logarithmically distributed in respect to z Λ^{-1}.

It is obvious that the choice of the gradient impacts the non-dimensional profiles to a large degree. The choice is, however, not straight forward. We will now take a look at the sensitivity of choosing a linear gradient, using different calculating ranges.

Figure 7.3 is the same as Figure 7.1 and Figure 7.2, but for different linear approximations of the gradient. The *dashed line* is calculated from a linear gradient between 4 and 0 meter height, the *dotted line* is calculated between 2 and 0 meter height, while the *full line* is calculated between 4 and 2 meter height, using Equation 4.13. The blue lines are for 2 meter height, and the red lines for 4 meter height. The non-dimensional profiles, estimated using the vertical wind gradients based on one of the two sonics and the surface (where the wind speed is zero), overestimates by around one order of magnitude. Using a gradient based only on the two direct measurements gives a non-dimensional gradient more in agreement with the universal functions. We see that the relationship between ϕ_m and z L^{-1} and z Λ^{-1} is in general twice as large for the 4 meter height. The source for this is the increase of z in Equation 2.13, and when using a linear gradient, u_* is the only component that can compensate for the increased z, as the gradient is constant with height when using a linear approximation. Looking at the time series for the whole campaign (Section A.1), we see that u_* is generally the same at both heights, with some variations. The only thing left to compensate for this is increase is the stability parameter, but as seen in Figure 7.3, the relationship using local scaling does not look significantly better.

Figure 7.3 shows that the non-dimensional profile is highly sensitive to the estimation of the vertical gradient. When using a linear gradient estimated between the ground and one of the two Sonic anemometers, it does not represent the expected non-dimensional profile, while using a linear gradient between the two Sonic anemometers performs better. This value seems to be more close to the local gradient, while it still does not look as good as the non-dimensional profiles using different orders of a logarithmic gradient.

In Figure 7.1-7.3 we have shown a high sensitivity for the non-dimensional momentum profile, to the choice of vertical wind gradient. As MOST assumes a logarithmic boundary layer, a linear gradient will not be valid for the whole surface layer. It is possible that the linear gradient calculated represents the present gradient at a given height. A linear gradient will therefore, by definition, not be suitable for MOST, but the calculated gradient might adequately represent, at times, the actual gradient. We have seen that a linear gradients calculated between both the surface and 2 meter and the surface and 4 meter height, overestimates by the order of one magnitude, while a gradient calculated between 2 and 4 meter, represents the non-dimensional profile better. The medians of ϕ_m comes closer to the universal functions ϕ_m^{H96} and ϕ_m^{G07} when using a logarithmic and second order logarithmic wind gradient.

If we assume the two different logarithmic wind profiles to be the best fit to our data, we can draw some conclusions from Figure 7.1 and Figure 7.2. When using a first order logarithmic gradient, the universal functions underestimate compared to our data for $\zeta < 0.2$, and overestimate for $\zeta > 0.2$. This will cause an overestimation of

the momentum fluxes for $\zeta < 0.2$ and an underestimation for $\zeta > 0.2$, when modeling using the parameterized non-dimensional profiles, as the fluxes are directly dependent on the gradient, which are dependent on the parameterization of the non-dimensional gradient.

The second order logarithmic fit manages to represent the universal functions for $\zeta < 0.2$ at 2 meter height, while it underestimates at 4 meter height. In total we find our data to be adequately represented by the empirical non-dimensional profiles until $\zeta > 0.2$ where the universal functions overestimates ϕ_m. The reason for this could be that we have too few observations in the higher stability range, or that the chosen gradient is underestimated for high stabilities. 2014 was a very mild winter on Svalbard (Section 3.4), which in general is expected to decrease the stability, compared to normal conditions, during the whole winter. This could be the reason for the few very stable measurements, and it can be one of the reasons why the non-dimensional gradient of momentum is poorly represented under very stable conditions. It is also possible that the universal function does not represent the stable conditions in Adventdalen, but it is hard to say something confidently, as the sensitivity to the chosen gradient is quite big, and the number of measurements are few.

7.2 The non-dimensional temperature profile

The non-dimensional temperature profile (or the non-dimensional gradient of heat), ϕ_h, is shown in Figure 7.4 with respect to the surface based (top) and local stability parameter (bottom). The universal function by *Högström* (1996) for heat (**black line**) is defined as:

$$\phi_h^{\mathrm{H96}} = 1 + 8\zeta \tag{7.5}$$

and the universal function for heat (**dashed line**) developed by *Grachev et al.* (2007) is:

$$\phi_h^{\mathrm{G07}} = 1 + \frac{5\zeta + 5\zeta^2}{1 + 3\zeta + \zeta^2} \tag{7.6}$$

The figure is the same as Figure 7.4 but for the non-dimensional temperature profile, ϕ_h, instead of the non-dimensional momentum profile, ϕ_m. It is important to note that we found the temperature measurements to not have been correctly calibrated, which have impacted the temperature gradient. We have tried to correct for this, under the assumption that the temperature profile is linear (Section 4.2.3), and if this is not the case, both the temperature difference and the temperature gradient will be erroneous.

As we have already assumed the shape of temperature profile we can no longer test with different approximations of the shape of the wind profile. We have to assume that a linear fit works adequately. As shown in the previous section, the choice of gradient can have large implications for the accuracy of the non-dimensional profile.

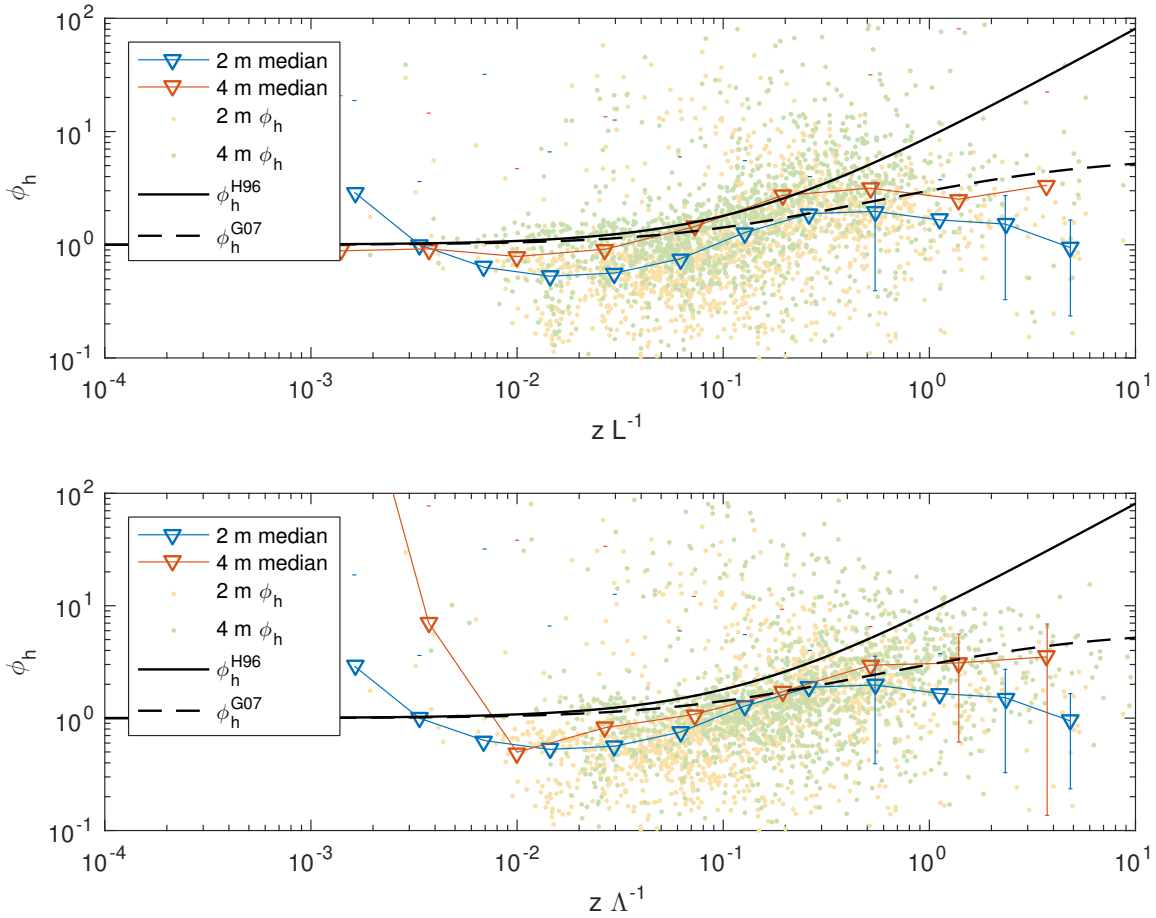

Figure 7.4: The non-dimensional temperature profile, ϕ_h, plotted against the surface based stability parameter z L^{-1}, and the local stability parameter z Λ^{-1}. The red and blue line shows binned medians with standard deviation at 2 and 4 meter height, and the yellow and green markers shows all 30-minute averaged measurements. The **black** line represents the universal function from *Högström* (1996) (Equation 7.5), and the **dashed line** represents the universal function developed by *Grachev et al.* (2007) based on the SHEBA data (Equation 7.6) . The bins are logarithmically distributed in respect to z Λ^{-1}.

From Equation 2.14 we see that an overestimated temperature gradient will lead to a overestimated non-dimensional profile, and vice versa for an underestimated gradient. Ideally we would like to test for different gradients, but as our sensors are not correctly calibrated, and we only have measurements at two heights, a reliable examination of different temperature gradients is not possible.

The shape of the medians in Figure 7.4 is quite close to the two empirically found universal functions, but it resembles ϕ_h^{G07} better for z L^{-1} > 0.2 and z Λ^{-1} > 0.2. When using the surface based stability parameter z L^{-1} there is a clear separation between ϕ_m at the two different levels. Using the local stability parameter z Λ^{-1} decreases this separation, in particular in the range 0.05 < z Λ^{-1} < 0.5.

As long as our non-dimensional profiles are trustworthy, the universal function by *Grachev et al.* (2007) in Equation 7.6 seems to be a relatively good fit to our data set, even tough there is a clear underestimation at 2 meter height for stabilities above z L^{-2} > 0.5 and z Λ^{-1} > 0.5. For stabilities lower than z L^{-1} < 0.01 the non-dimensional

gradients are highly overestimated, implying that the temperature gradient is erroneous, because the shape of the temperature profile wrong, or that we have performed an erroneous calibration of the temperature sensors (Section 4.2.3).

We found a high sensitivity for the non-dimensional momentum profile to the chosen wind gradient (Section 7.1). This should imply that the non-dimensional temperature profile is, as well, very sensitive to the chosen temperature gradient. The reliability of our data is consequently reduced, as we have made a lot of assumptions in the process of calculating the temperature gradient. Despite of this uncertainty we found the median of ϕ_h to be quite well represented by the universal function developed by *Grachev et al.* (2007), ϕ_h^{G07}, for stabilities higher than $\zeta > 0.01$.

8 Summary and outlook

8.1 Summary

We did fast response measurements in Adventdalen, Svalbard, using Sonic anemometers at two heights, and slow response measurements on a 10-meter mast at two heights. The objective of this thesis is to analyze the data set, with respect to the driving forces for stability. We also wanted to check, for Adventdalen, the validity of MOST under stable conditions, and compare with MOST extended for stable conditions using local scales. An examination of the non-dimensional profiles, and the sensitivity to the calculation of the vertical wind gradient, were also performed.

We found a wider spread in the stabilities at 4 meter compared to 2 meter height (Figure 5.1-5.2), meaning that we had a tendency to get more stable, or unstable, conditions from the 4 meter measurements. Because of too few measurements in the unstable range, we decided to focus only on the stable conditions, from there on. We, expectedly, found that the stability was highly influenced by the wind speed, the wind direction and the net radiation. Higher wind speeds caused turbulent mixing, which shifted the stratification towards the neutral range. During calm conditions the potential for very stable conditions were present. We found that the stratification had a tendency to be more stable for SE wind (Figure 5.3), coming from within the valley. For NW wind, coming from the ice-free Adventfjorden, the air had a tendency to be less stable for the same wind speeds, compared to SE wind. The net radiation balance was also important (Figure 5.4), where large negative net radiations caused a more stable atmosphere, but with a clear dependence on the wind speed. The conclusion is that the main drivers of the stability in Adventdalen are the wind speed, the wind direction and the net radiation balance. Calm conditions with weak SE wind and strong negative net radiations were favorable to get very stable conditions.

We found the downward heat flux maxima at $\zeta \approx 0.01$ (Figure 6.1). *Mahrt et al.* (1998) found the transition regime to start at the location of the downward heat flux maxima. Local scaling should perform better in the transition regime, but we did not find that local scaling worked best for $\zeta > 0.01$. As MOST assumes the fluxes to be constant with height, we want to find a relationship between the flux and the stability

parameter, that is the same for the two heights. We found that the surface based scaling represented this behavior best, until $\zeta \approx 0.3$. For $\zeta > 0.3$ local based scaling performed better until $\zeta \approx 0.5$, where the number of observations gets too low to say anything with confidence. One reason why we did not see the downward heat flux maxima at higher stabilities could be because we do not have observations at higher levels. *Grachev et al*. (2005) found the heat flux maxima to shift to higher stabilities for the higher levels, when using local scaling, until reaching a constant value of $\zeta \approx 0.1$. This shift is not seen in our data set. Surface based MOST predicted the relationship between the momentum flux and the stability best, for all stability ranges (Figure 6.2). Applying local scales to the stability parameters separated the relationship for the two heights, and thus had a worse performance than the surface based scales.

The turbulent Ekman layer is the stability regime where the the influence of the earth's rotation becomes important, and where MOST fails to predict the turbulence. We found by investigating the Ekman number (Figure 6.5) that our observations are, for stabilities below $\zeta \approx 3$, twice as much influenced by surface forcing compared to the Coriolis force. This leads us to conclude that for most of the time, we are either within the surface layer scaling regime, or the transition regime, with no significant amount of measurements within the turbulent Ekman layer. As surface based scaling performed better up to $\zeta \approx 0.3$ for the buoyancy flux, and at all times for the momentum flux, it leads to the conclusion that our data lies mostly in the surface based scaling regime, and classic MOST represents the turbulence best. This is in contrast with *Grachev et al*. (2005) who found local based scaling, or the transition regime, to represent the fluxes better for $\zeta > 0.1$.

The flux Richardson number was found to be a poor threshold for suppressed turbulence, as we saw small fluxes for the critical flux Richardson number, $\mathrm{Rf_{cr}} > 0.2$, which is agreement with the results found by *Grachev et al*. (2013). They did find $\mathrm{Rf_{cr}} > 0.2$ as a good threshold for the boundary between the transition regime and the turbulent Ekman layer. In our data $\mathrm{Rf} > \mathrm{Rf_{cr}}$ occurs at 12% and 19% of the time at 2 and 4 meter height, respectively. As we previously found that we did not have any significant number of measurements which were significantly influenced by the rotation of the earth (Figure 6.5), the critical flux Richardson number does not seem to be an appropriate upper boundary for the applicability of local scaling.

By investigating the non-dimensional profiles of temperature and momentum, we found a high sensitivity to the choice of the vertical wind gradient. An inaccurate wind gradient overestimated ϕ_m by up to one order of magnitude. A first order and second order logarithmic fit to the wind profile gave the best results. The universal functions by *Högström* (1996) and *Grachev et al*. (2007) adequately represented ϕ_m for stabilities in the range $\zeta < 0.2$. The universal functions overestimated ϕ_m for higher stabilities. This could be caused by too few observations in this stability range, or that the uni-

versal functions simply do not represent Adventdalen adequately for relatively stable conditions, but too firm conclusions are unreasonable because of the low number of observations in this range.

The non-dimensional temperature gradient, ϕ_h, was quite well represented for stabilities higher than $\zeta > 0.01$, by the universal function empirically found by *Grachev et al*. (2007). As we had to perform a temperature correction, due to wrongly calibrated temperature sensors, the temperature gradients are not as reliable as they could have been. The temperature profile is assumed to be linear in the correction process, and the investigation of different gradients were thus unreasonable. As we have already seen the sensitivity for the calculated non-dimensional gradient to the choice of vertical gradient, our calculated ϕ_h might therefore be, somewhat, inaccurate. Our non-dimensional temperature profile, ϕ_h, is, however, well-represented by the universal function found by *Grachev et al*. (2007).

The differences compared to the results from SHEBA (e.g *Grachev et al*., 2005, 2013) can possibly be explained by the exceptionally mild conditions during our campaign on Svalbard. Consequently, very stable conditions are absent, or at least heavily underrepresented. In contrast to the SHEBA environment, we are also in a heterogenous and non-idealized area, such that orographic effects and local advection may limit the similarity theory, as found by *Mäkiranta et al*. (2011).

8.2 Further work

A better temperature correction algorithm can be created, in order to get more reliable temperature measurements. The contribution from large-scale motion could be filtered out from the fluxes, in order to investigate the behavior of the fluxes at high flux Richardson numbers, with more confidence. A new measurement campaign, with correctly calibrated temperature sensors and measurements at more and higher levels, could be taken in order to continue to evaluate the results from the SHEBA campaign, in a non-idealized environment.

A Appendix

A.1 Data

Weekly plots of the complete dataset are shown in Figure A.1 to A.14.

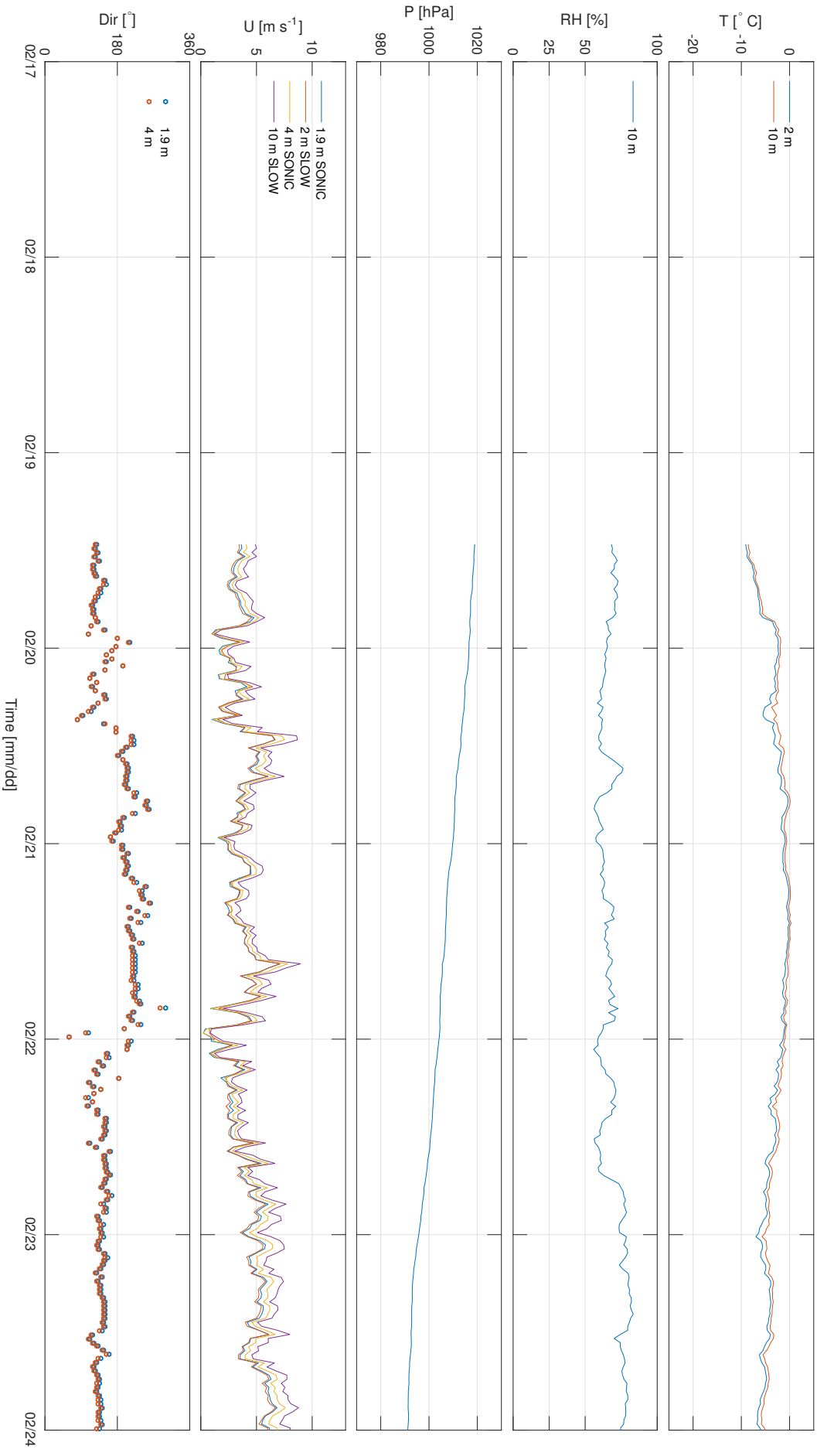

Figure A.1: Meteorological parameters measured in Adventdalen from the 18th to the 24th of February 2014. It shows, from top to bottom, temperature at 2 m and 10 m, relative humidity at 10 m, pressure, wind speed and wind direction at different heights and from to types of sensors.

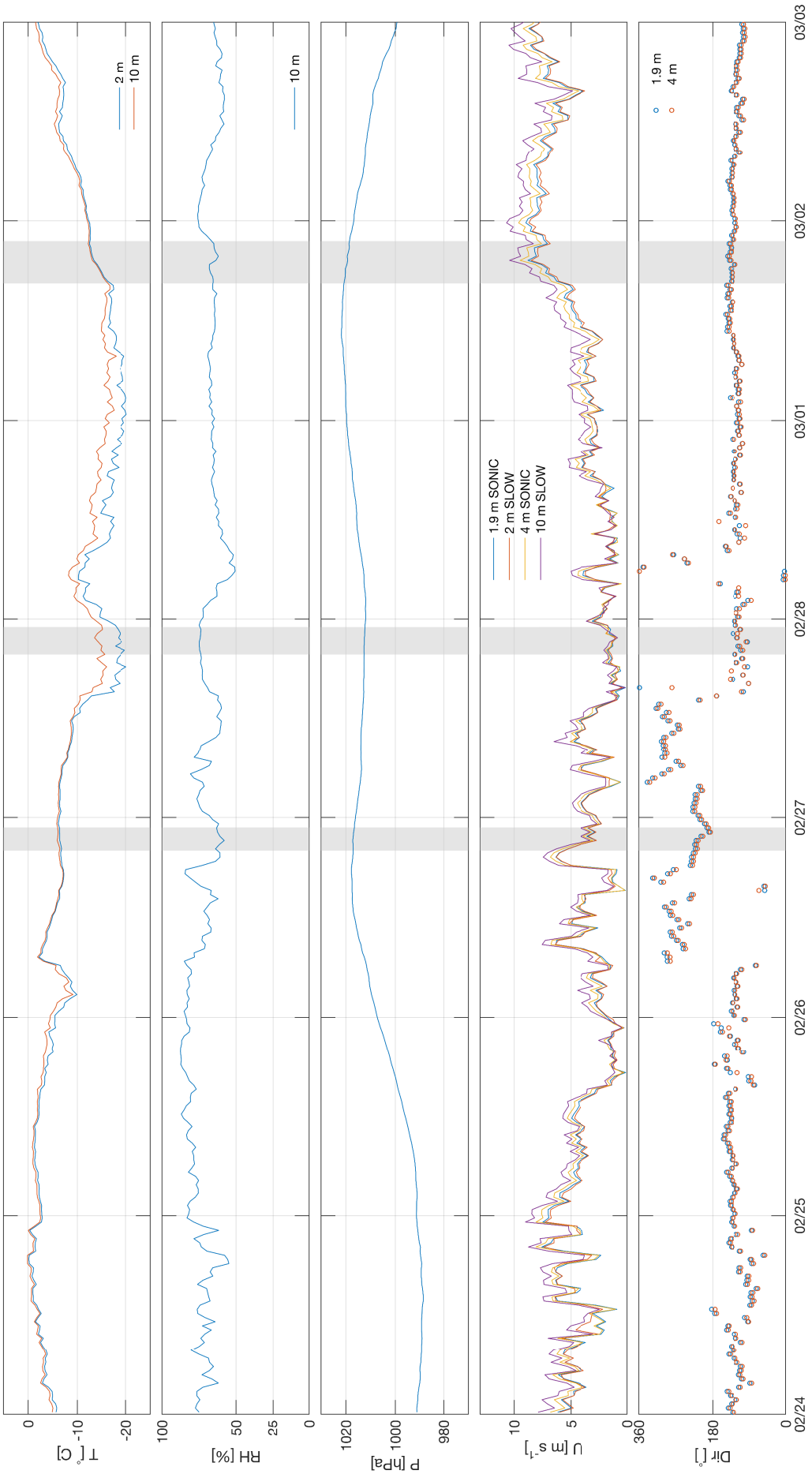

Figure A.2: Same as Figure A.1 for week 9 of 2014.

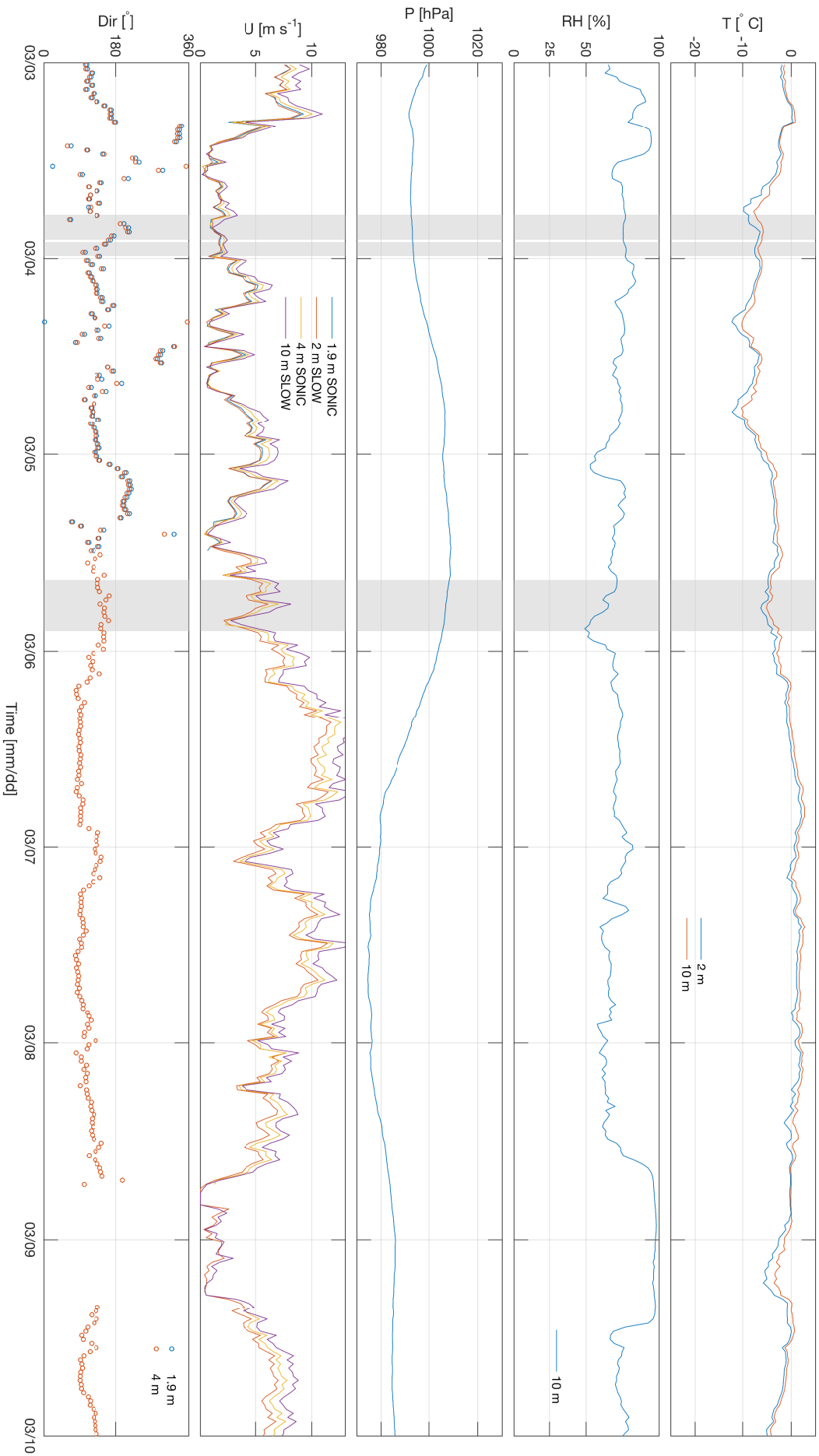

Figure A.3: Same as Figure A.1 for week 10 of 2014.

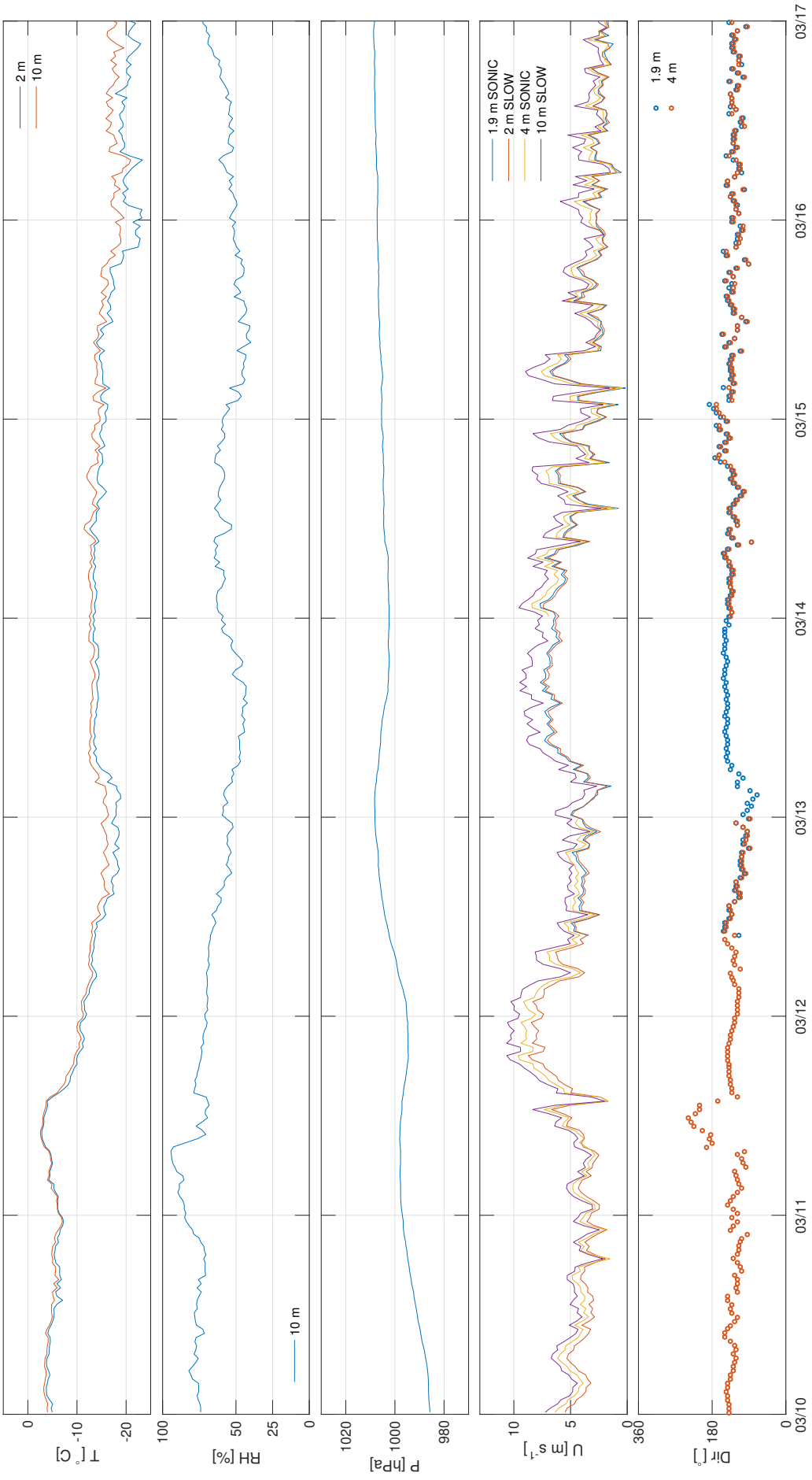

Figure A.4: Same as Figure A.1 for week 11 of 2014.

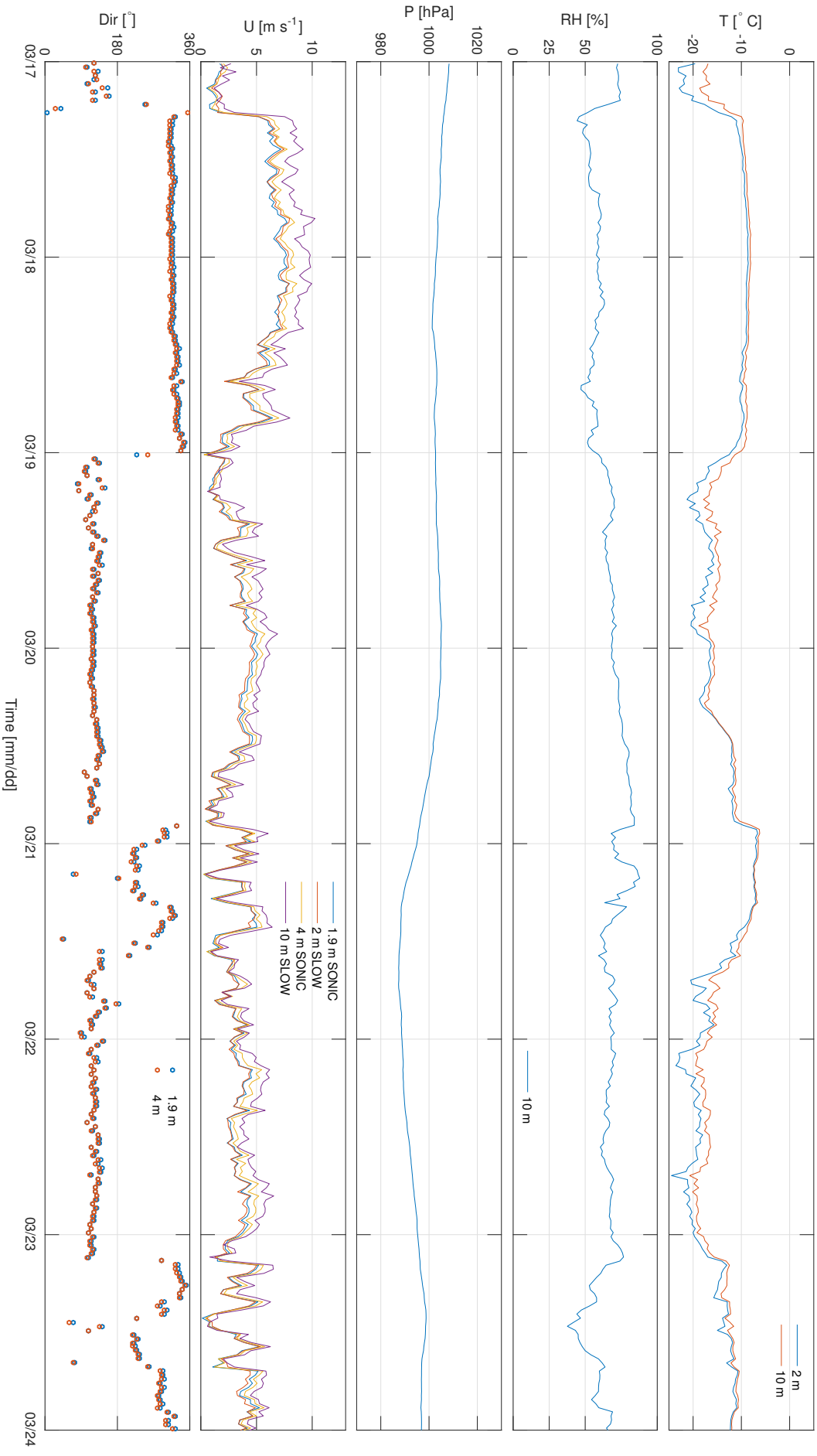

Figure A.5: Same as Figure A.1 for week 12 of 2014.

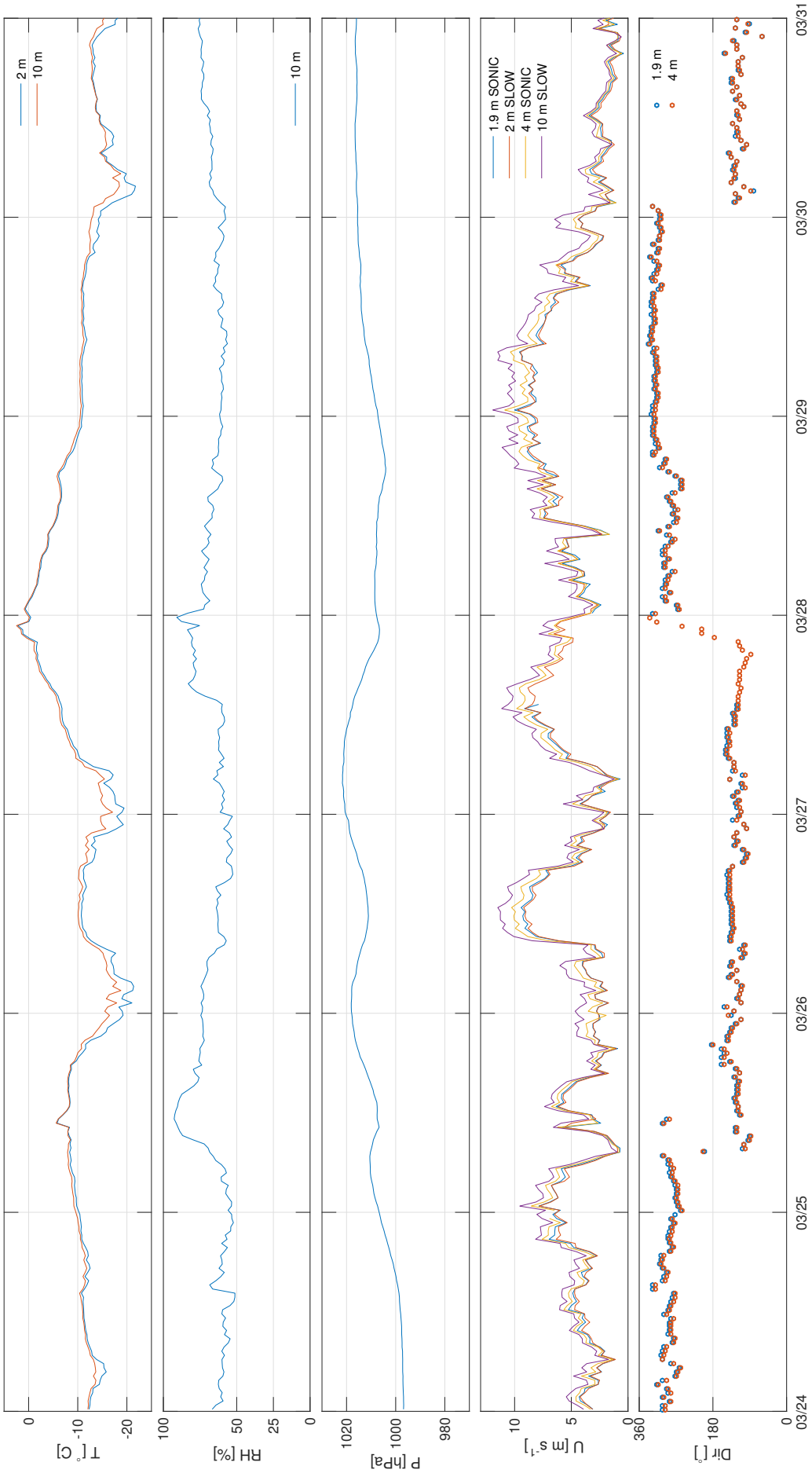

Figure A.6: Same as Figure A.1 for week 13 of 2014.

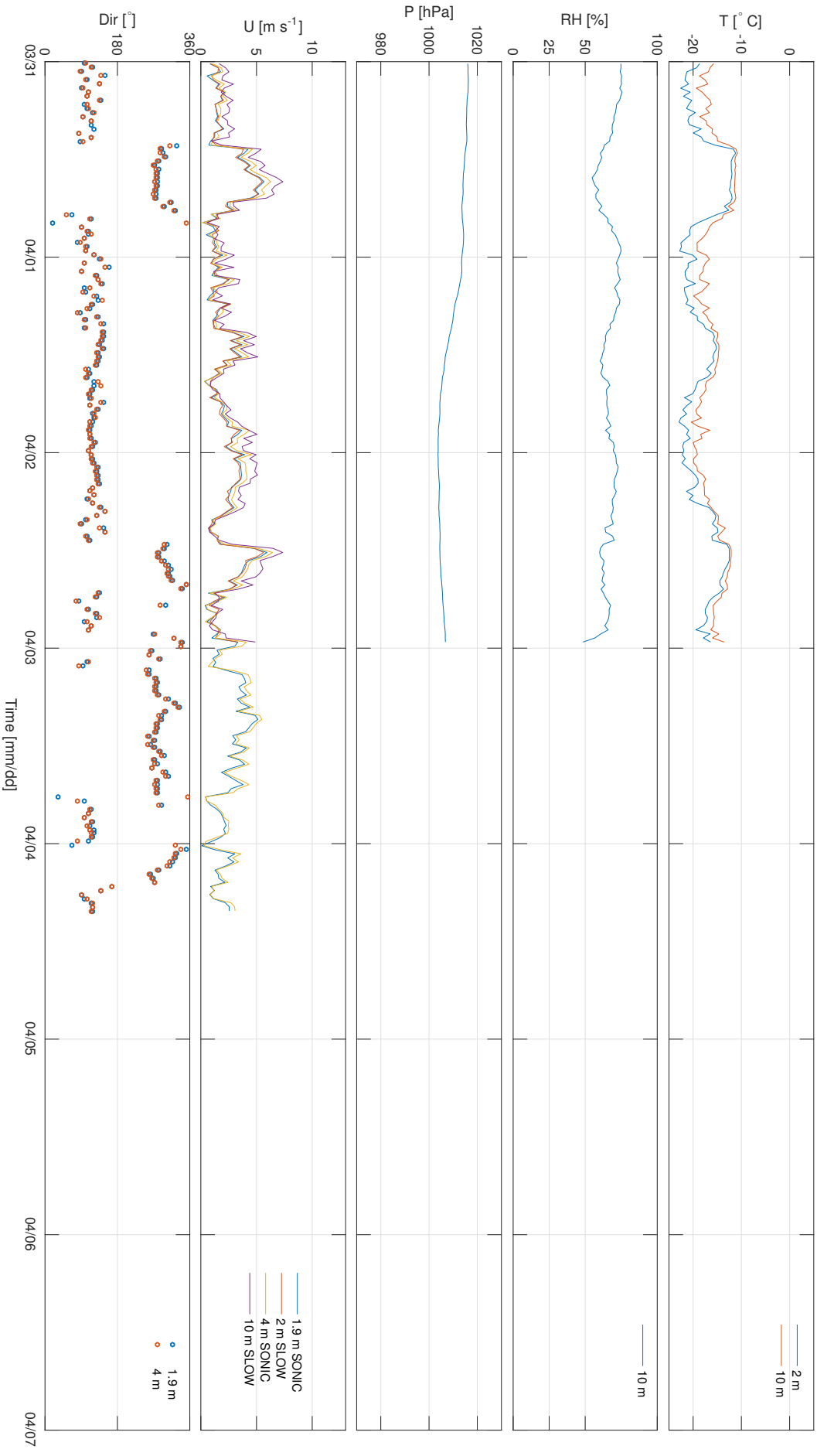

Figure A.7: Same as Figure A.1 for week 14 of 2014.

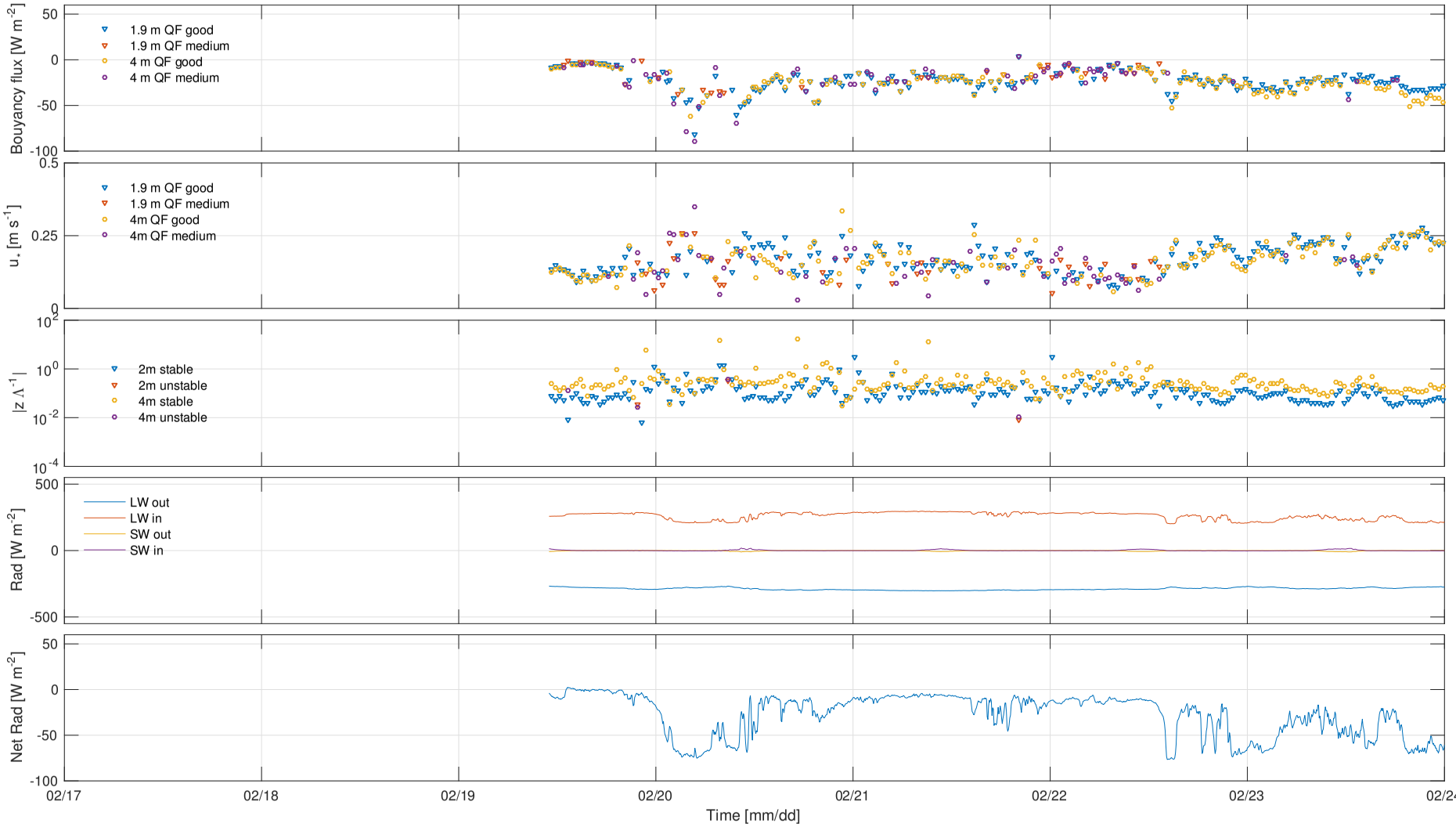

Figure A.8: Derived meteorological parameters based on the measurements in Adventdalen from the 18th to the 24th of February 2014. It shows, from top to bottom, the buoyancy flux at 1.9 and 4 m, the friction velocity u_* at 1.9 and 4 m, the local stability parameter $z\ \Lambda^{-1}$ at 1.9 and 4 m, incoming and outgoing longwave and shortwave radiation, and the net radiation. The first three plots also include the information on the data quality as color code (see Section 4.1.5). Grey filling means that tethersonde data is available.

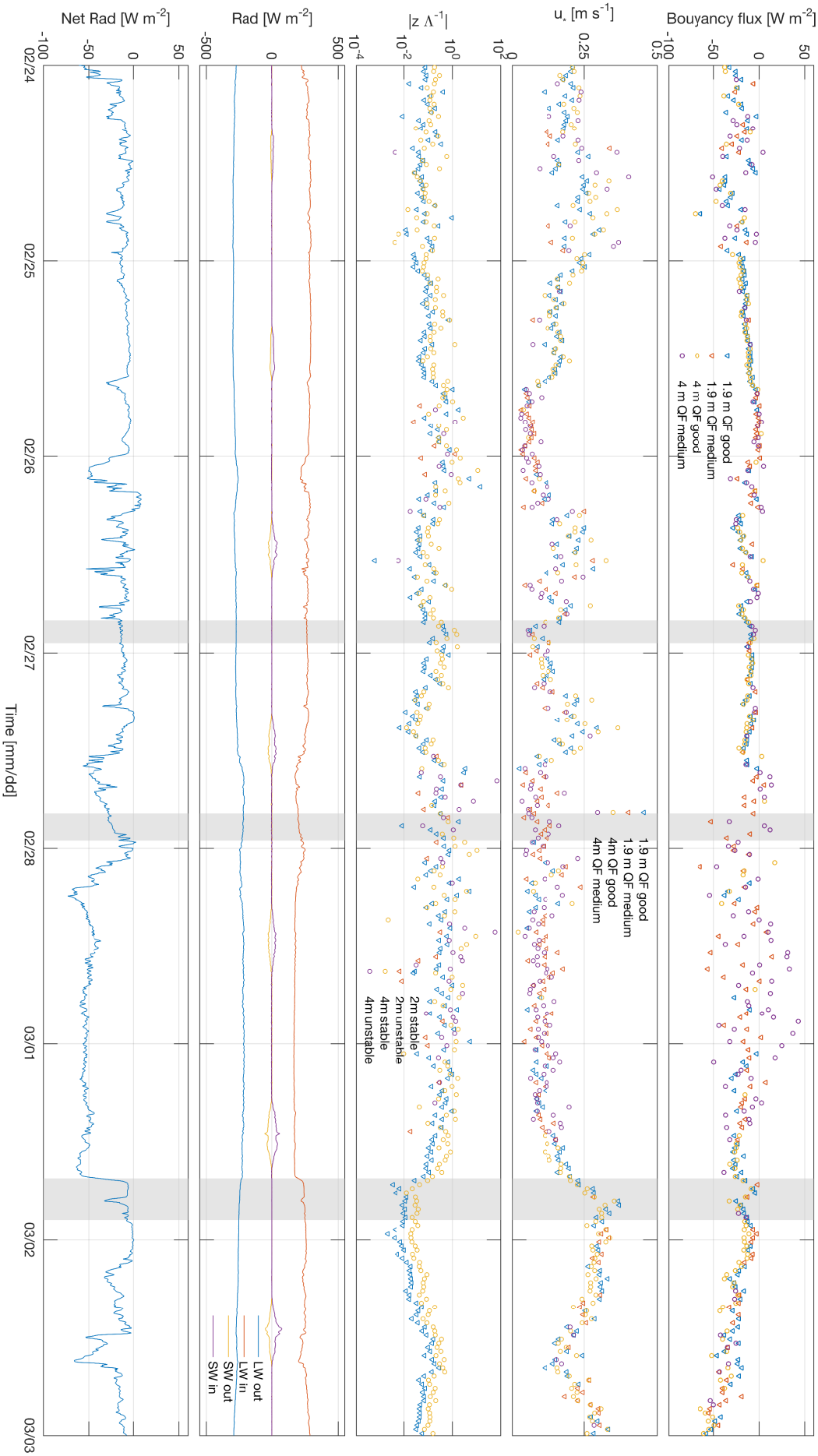

Figure A.9: Same as Figure A.8 for week 9 of 2014.

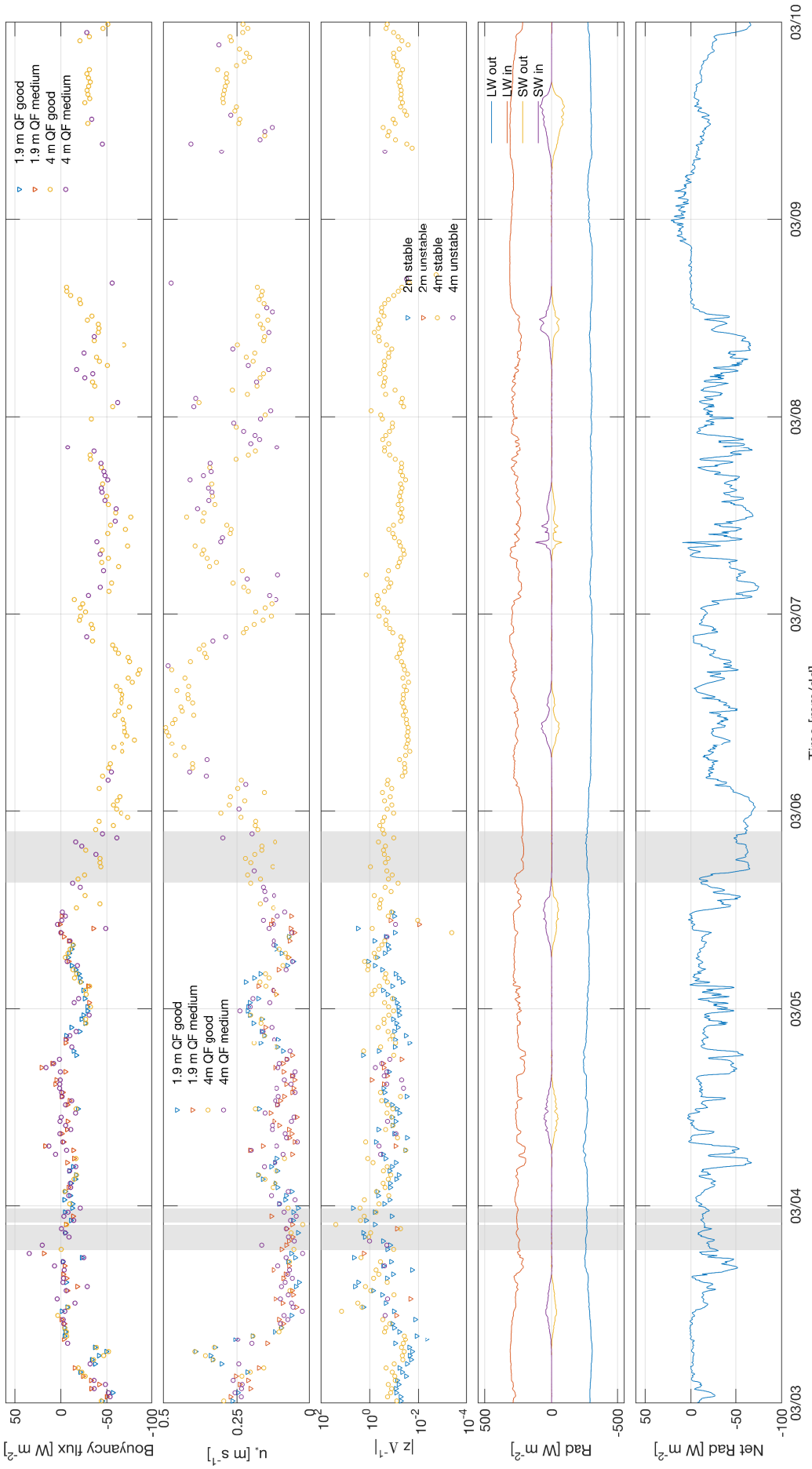

Figure A.10: Same as Figure A.8 for week 10 of 2014.

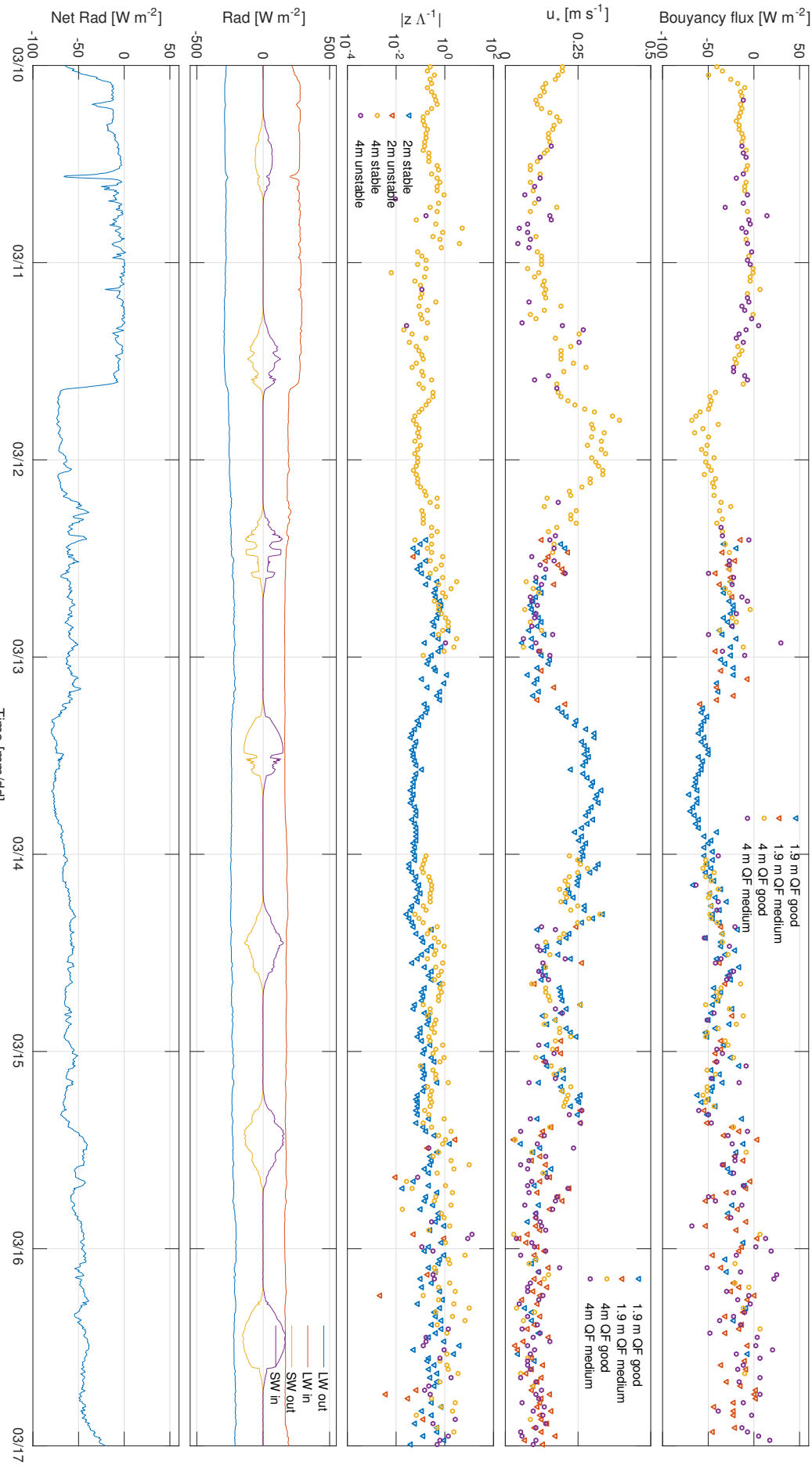

Figure A.11: Same as Figure A.8 for week 11 of 2014.

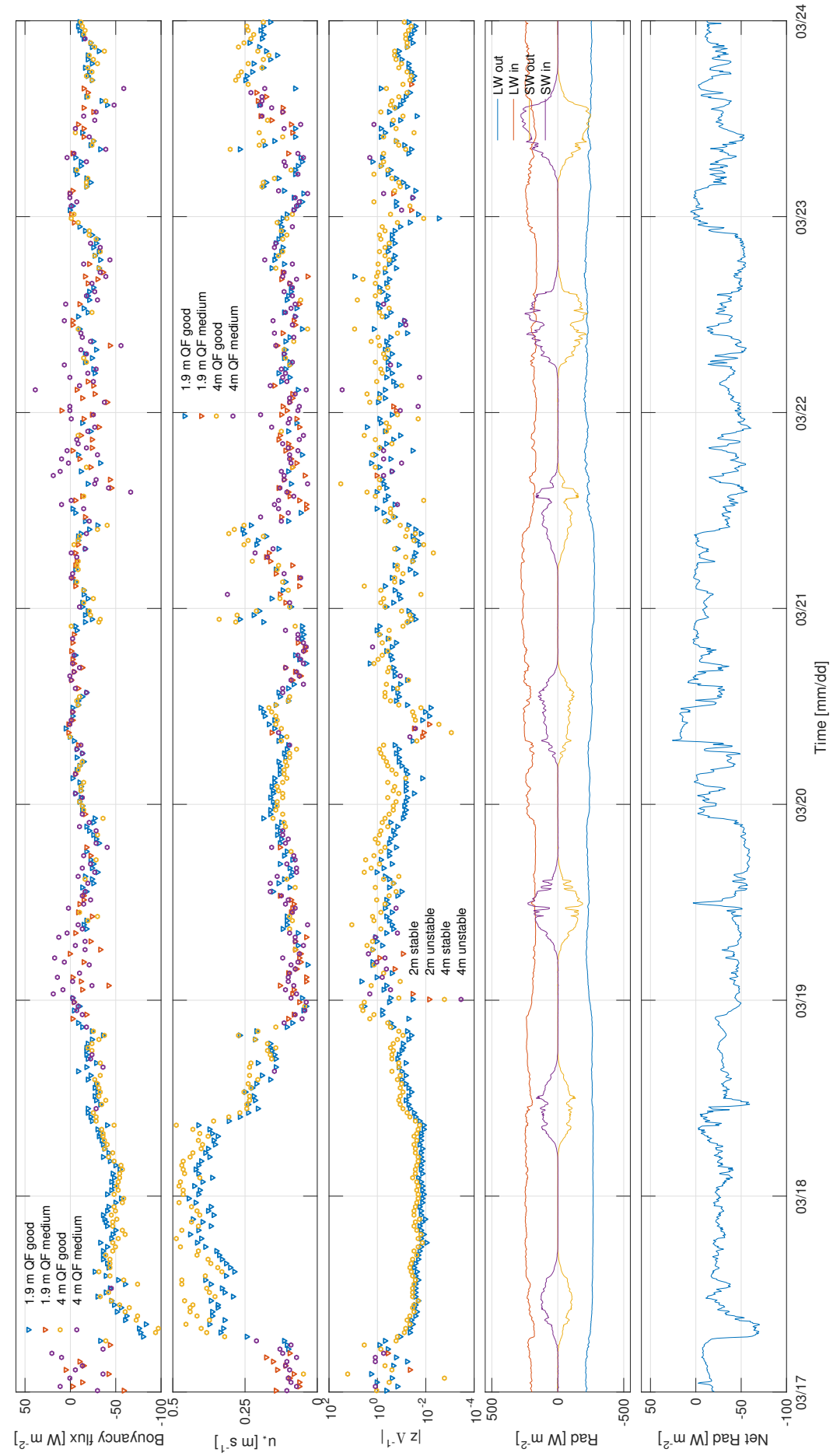

Figure A.12: Same as Figure A.8 for week 12 of 2014.

texcount

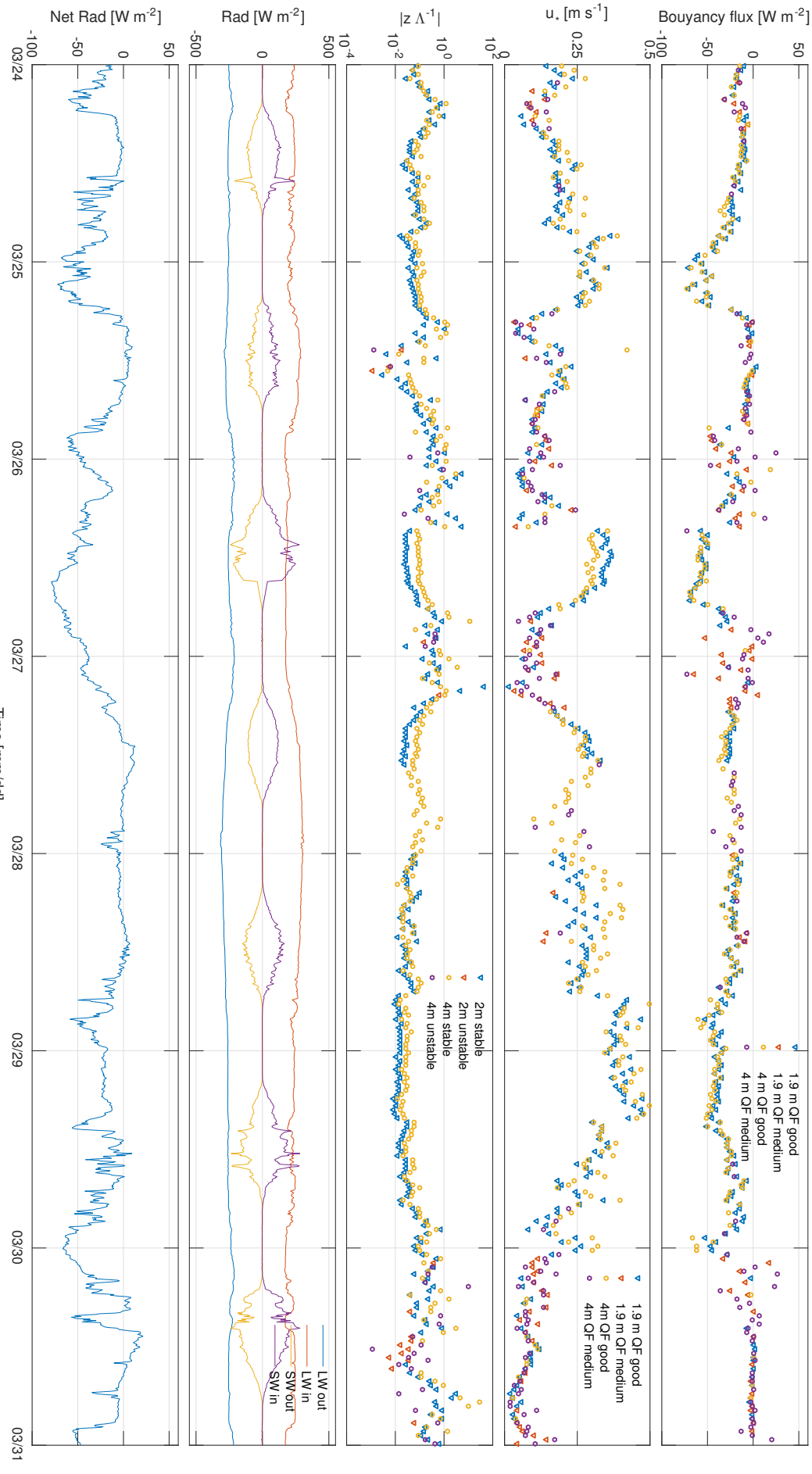

Figure A.13: Same as Figure A.8 for week 13 of 2014.

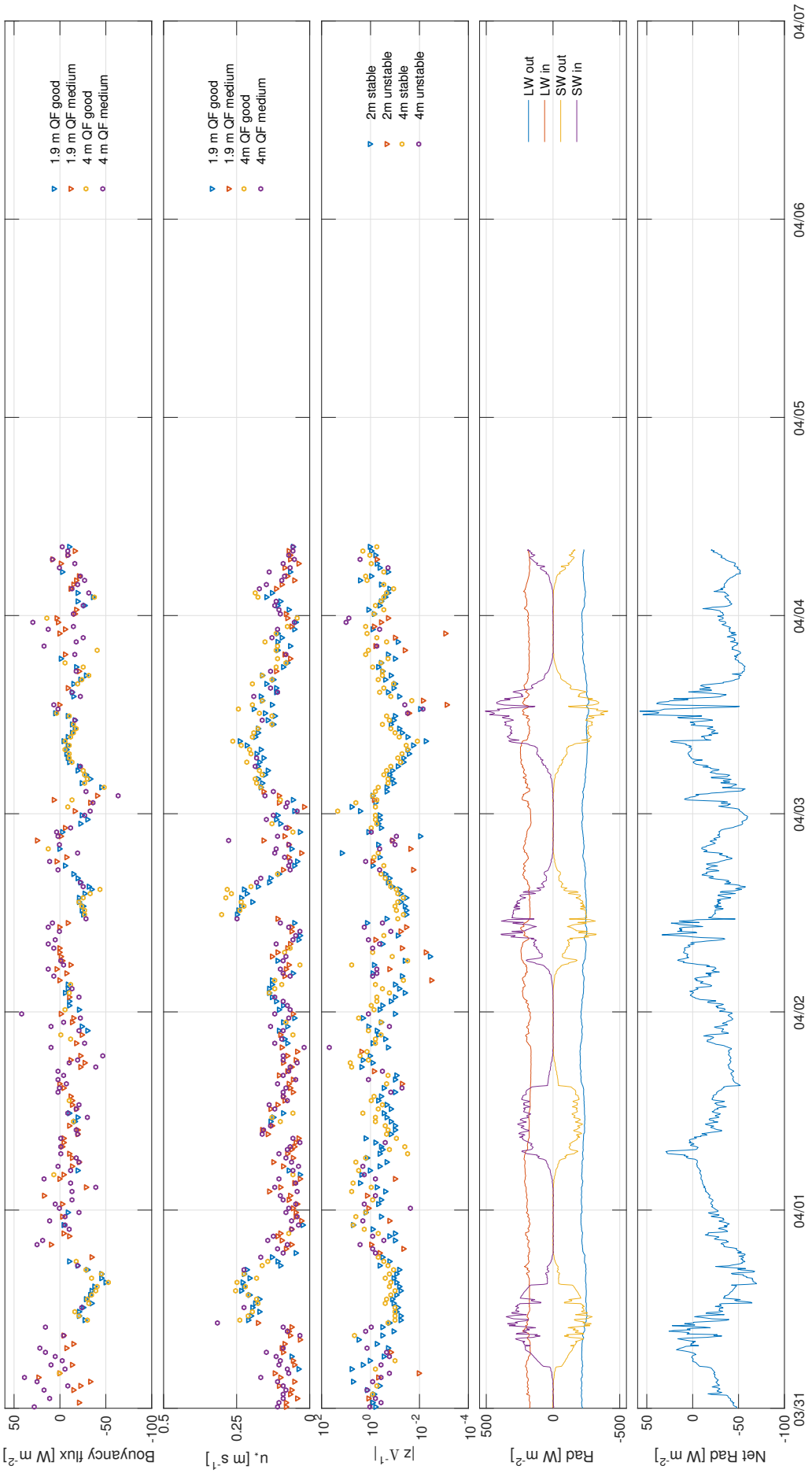

Figure A.14: Same as Figure A.8 for week 14 of 2014.

A.2 TK3.11

The following is the code for the Turbulence Knight 3.11 parameter file, used to analyze the data from the two Sonic anemometers. The parameter file for the Sonic anemometer at 2 and 4 meter height is shown in Listing A.1 and Listing A.2, respectively.

Listing A.1: Parameter file for the Sonic anemometer at 2 meters

```
# parameter.vbp
#
# The new Turbulence Knight (TK3) reads all input parameters from this file
    .
# TK3 may also be controlled by editing this file.
#
# Lines beginning with '!' serve as label for parameters to be read in the
    next line
# Lines beginning with '#' serve as comments and will be ignored
# Blank lines will be ignored as well
# Parameters shall be given with an explanation in the line above for
    better reading of this Input-File
#
#-------------------------------------------
# Path of input data
!path_in
'C:\TK3_11\Sonic2\in\'
# Path of working directory
!path_work
'C:\TK3_11\Sonic2\work\'
# Path of output data
!path_out
'C:\TK3_11\Sonic2\out\'

# who did calculations
!author
'Andreas Froyland'
# Project Name
!project
Adventdalen2m

!header_info
F
#################### site and device data ####################
# sonic type (CSAT3,USA-1,Solent-HS,Solent-R3,Solent-R2,ATI-K,NUW,YOUNG)
!sonic_type
'CSAT3'

# H2O/CO2 instrument type (LI-7500,KH20,LI-6262,LI-7000,LI-7200,EC150,EC155
    ,LGR,NONE)
!h2o_type
'NONE'

# CH4 instrument type (LI-7700,LGR,Aerodyne,NONE)
!ch4_type
'NONE'
```

```
# hd: measuring height of the device in m (for each measuring complex), (
    REAL)
# hc: canopy height below the device in m (for each measuring complex), (
    REAL)
# wd: wind direction or orientation of u-component of the device in deg. (
    REAL)
# height above sea level (REAL)
!dev_data
1.97, 0, 236, 8

# latitude(REAL,INTEGER,INTEGER)
!latitude
78, 12, 06


# Start of processing period (day of year, hour, second) and end-time (
    integer,integer,real)
!start
50,1100,0.00
###45,1400, 0.00

# End of processing period (day of year, hour, second) and end-time (
    integer,integer,real)
!end
94,0830,0.00
### 94,0834,20.95
### 71 is the missing day

# Year of measurements (calculations are only possible within one calender
    year)
!year
2014

# minutes in binary files (REAL)
!t_interval
30

# if binary files exist, type T (LOGICAL)
!load_binary
F
######################## INPUT DATA FILE
    ###################################
#Set true T if the original Campbell logger files are split into hourly
    portions using the program HourlySplitData;
#the input file name will then automatically be generated starting with the
    letter "B"
```

```
!HourlySplitData
F

#name␣of␣first␣data␣file␣(all␣other␣files␣will␣be␣found␣by␣nTK2␣according␣
    to␣the␣given␣time␣window)
!data%file_name
'TOA5_2246_Flux_20140219.dat'


#Input␣file␣format␣('ASCIIcsv','SLT')
!input_file_format
'ASCIIcsv'

#number␣of␣records,␣total␣number␣of␣columns␣in␣input␣file,␣including␣time␣
    stamps␣(INTEGER)
!number_of_records
8

#Format␣of␣time␣stamp
#1␣=␣CR23x,␣e.g.␣254,1030,30.44
#2␣=␣TOA5,␣e.g.␣"2005-09-11␣10:30:30.44"
#3␣=␣LabView,␣e.g.␣254,10:30:30.44
!time_format
2

#Start␣column␣of␣each␣channels␣in␣input␣files,␣if␣not␣associated␣enter␣'0'
!column
␣␣␣␣␣␣␣0,␣␣␣␣␣␣␣␣␣␣1,␣3,␣4,␣5,␣␣6,␣␣␣␣7␣,␣␣0␣,␣␣0␣,␣␣0␣␣,␣0␣,␣␣0,␣␣␣␣␣␣0,␣␣
    ␣␣␣0,␣␣␣␣0␣,␣␣␣␣0,␣␣␣0,␣␣0␣,␣␣␣␣0,␣0
#log_num,␣time_stamp,␣u,␣v,␣w,␣Ts,diagCS,␣co2,␣h2o,diagLI,␣Tp,␣o3,␣incl_x,␣
    incl_y,␣LI_p,␣LI_T,␣CH4,␣N2O,␣HMP_T,HMP_RH

!Aerodyne_file
F
!data_Aero%file_name
'140821_000000.str'

#Units␣of␣channels␣in␣input␣data␣file,␣if␣not␣associated␣enter␣'0'
!unit_wind␣('m s-1','cm s-1')
'm s-1'
!unit_Ts␣('degC','K')
'degC'
!unit_co2␣('mV','mmol m-3','umol mol-1','mg m-3')
'mg m-3'
!unit_h2o␣('mV','g m-3','mmol mol-1','mmol m-3')
'g m-3'
!unit_Tp␣('R R0-1','degC','K')
```

```
0
!unit_o3␣('µg m-3','ppb')
0
!unit_LI_p␣('kPa','hPa')
'kPa'
!unit_LI_T␣('degC')
0
!unit_CH4␣('umol mol-1','nmol mol-1','umol m-3')
0
!unit_N2O␣('nmol mol-1')
0
!unit_HMP_T␣('degC')
degC
!unit_HMP_RH␣('%','kPa')
%

#consistency␣limits,␣in␣same␣units␣as␣in␣input␣file
!input%log_num␣#Logger␣program␣ID␣number,␣e.g.␣for␣CR23X
0,0
!input%day␣#Day␣of␣year
1,366
!input%hour␣#Daily␣time
0,2400
!input%second␣#Seconds
0.0,60.0
!input%u␣#Wind␣u
-50.0,50.0
!input%v␣#Wind␣v
-50.0,50.0
!input%w␣#Wind␣w
-10.0,10.0
!input%Ts␣#Sonic␣temperature
-50.0,30.0
!input%diagCS␣#CSAT␣error␣code,␣usually␣counts␣up␣from␣0␣to␣63;␣set␣0,0␣if␣
   not␣associated,␣IMPORTANT!
0,63
!input%co2␣#CO2
0,2000
!input%h2o␣#H2O
0,35
!input%Tp␣#Platinum␣temperature
0.,0.
!input%o3␣#Ozone
0,0
!input%diagLI␣#diagnostic␣Licor
240,251
!input%incl_x␣#Inclinometer␣x-axis
```

```
0,0
!input%incl_y␣#Inclinometer␣y-axis
0,0
!input%LI_p␣␣␣#pressure␣Licor
80,110
!input%LI_T␣␣#temperature␣Licor
0,0
!input%CH4␣␣␣#methane
0,0
!input%N2O␣␣␣#nitrous␣oxide
0,0.
!input%HMP_T␣␣#reference␣temperature
-20,50
!input%HMP_RH␣␣#reference␣humidity
0,100


#Fixed␣time␣delays␣of␣channels␣in␣input␣data␣file␣[seconds]
!lag
0.0,0.0,0.0,0.0,0.2,0.2,0.0,0.0,␣␣␣0.2,␣␣␣0.0,␣␣␣0.0,0.2␣,0.0␣,0.0,0.0,␣0.0
   ␣,␣0.0
#u␣,␣v␣,␣w␣,␣Ts,co2,h2o,␣Tp,␣o3,diagLI,incl_x,incl_y,LI_p,LI_T,CH4,N2O,
   HMP_T,HMP_RH

!lag_Aerodyne
4.,4.
#CH4,N2O

#Parameters␣are␣required␣to␣create␣an␣equidistant␣time␣scale
#TK2␣will␣search␣for␣the␣data␣line␣in␣input␣file␣that␣matches␣the␣given␣
   time␣stamp␣best
#desired␣time␣interval␣or␣measure␣interval␣in␣sec␣(REAL)
#minimal␣time␣interval␣in␣sonic␣data␣file:␣very␣important␣(REAL
!calc_data
0.051,0.049

#What␣is␣missing␣value,␣what␣is␣the␣code␣for␣missing␣values␣in␣input␣file
!NaN
-9999


#What␣to␣do␣with␣missing␣values
#0␣=␣insert␣NaN␣␣(recommended␣for␣flux␣calculations)
#1␣=␣take␣last␣value␣␣(recommended␣for␣spectral␣calculations,␣including␣
   errors)
#2␣=␣linear␣interpolation
!mv_option
```

```
1

#Missing␣values␣at␣the␣beginning␣of␣blocks␣will␣be␣ignored(F)␣or␣replaced(T
    )
!fill_up_missing_values_at_begin
T

##␣Calibration␣data␣#################
#left␣hand␣coordinate␣system␣(e.g.␣USA-1,Solent-R2):
!lefthand
F
#Head␣Correction␣for␣METEK␣USA-1:␣(0,1,3)
!HC
0
#Licor␣CO2:␣0V␣and␣5V␣equal␣[mmol/m?]␣if␣LI-7500␣in␣mV,␣or␣[ummol␣mol-1]␣if
    ␣LI-7000/LI-6262␣in␣mV
!calib_data%co2
0.,␣1.

#Licor␣H2O:␣0V␣and␣5V␣equal␣[mmol/m?]␣if␣LI-7500␣in␣mV,␣or␣[mmmol␣mol-1]␣if
    ␣LI-7000/LI-6262␣in␣mV
!calib_data%h2o
0.,1.
!calib_data%pt150
17.5,100.,146.84,0.00366
!calib_data%kh20
0.00,␣0.0000,␣␣0.0000,␣-0.0450

!apply_spike_test␣#Apply␣MAD␣spike␣test␣(Mauder␣et␣al.,␣2013)
T
#values␣exceeding␣median+-'7'*std␣equivalent␣are␣spikes
3.5

####################␣REFERENCE␣FILE␣################################
#Reference␣option?
#0␣=␣no␣reference␣measurements␣for␣pressure,␣temperature␣and␣humidity
#1␣=␣reference␣measurements␣in␣same␣data␣file␣as␣turbulent␣data␣(e.g.␣from␣
    HMP45)
#2␣=␣reference␣measurements␣in␣second␣data␣file␣(e.g.␣A6__M001.csv)
!ref_option
0

#consistency␣limits
#Temperatur␣reference␣(degC)
!input%temp
0.,50.
#Humidity␣reference␣(g/m3)
```

```
!input%hum
0.,50.
#Pressure␣reference␣(hPa)
!input%pressure
800.,1100.

#------------------------------------------------------------------
##############################␣Trouble␣Shooting␣
    ################################
!ascii␣#ASCII␣Output␣of␣raw␣data(T/F),with␣flags␣(T)␣or␣without␣(F)
F,F

!invalid_data
T

###################␣Calculation␣parameters␣##########################
!load_statistics␣#files␣with␣Covariances␣already␣exist?
F
!calc_data%t_interval1␣#␣Calculation␣time␣intervals␣in␣minutes
30
!calc_data%bad_max␣#␣maximum␣allowed␣number␣of␣missing/bad␣values␣in␣
    averaging␣interval␣in␣%␣(REAL)
1
#format␣of␣the␣covariance␣output␣file
#0␣=␣LITFASS-2003␣standard␣exchange␣format
#1␣=␣Mikrometeo␣with␣Sonic␣Nvalue␣(incl.␣wind␣direction,␣<w'e'>)
#2␣=␣Mikrometeo␣and␣detailed␣Nmiss
#5␣=␣Mikrometeo␣with␣Sonic␣Nvalue␣plus␣MBR␣psychrometers
#6␣=␣Mikrometeo␣and␣detailed␣Nmiss,␣incl.␣N2O
#7␣=␣like␣2␣plus␣random␣errors␣␣␣(allows␣for␣error␣calculation)
#8␣=␣like␣7,␣plus␣CH4,␣and␣N2O␣␣␣(allows␣for␣processing␣CH4␣and␣N2O␣data)
!format_cov
0

!errors␣#calculate␣random␣errors␣and␣instrumental␣noise␣(Mauder␣et␣al.,␣
    2013)
T

!x_max␣#perform␣cross␣correlation␣to␣maximise␣covariances␣of␣additional␣
    sensors␣with␣w
F
!combine␣#combine␣short-term␣moments␣for␣longer␣time␣periods(T/F),␣only␣
    useful␣if␣no␣high-frequency␣data␣are␣available
F
!calc_data%t_interval2␣#short-term␣averaging␣interval␣[min]
5
```

```
!calc_data%t_interval3 #Interval between two subsequent averaging intervals
    , only applies if combine = T, else enter '0'
0

#---------------------------------------------------------------
#################### Correction of Fluxes ###############################
!planar_correct #Planar fit method (Wilczak et al.,2001)
T
!read_pf #read(T) or calculate(F) coefficients of multiple regression
F
!bk #b-coefficients, default 0.,0.,0. means no tilt correction, only
    rotation into mean wind
0.,0.,0.
!mean_wind #perform rotation into mean wind direction
T
!scalar_fluxes #transformation of scalar fluxes
T
!double_rotation #apply the double rotation method (T/F), should only be
    applied if !planar_correct = F
F

!tanner_correct #Tanner oxygen Correction
F

!moore_correct #Moore correction
F
!sa #sensor separation w - a [m]
0.30
!sc #sensor separation w - CO2 [m]
0.30
!n0 #cut-off frequency for CO2, H2O, CH4, N2O [Hz]
20,20,20,20
!sTp #sensor separation w - Tp [m]
0.01
!sn2o  #sensor separation w - N2O [m]
0.01
!sch4  #sensor separation w - CH4 [m]
0.01
!Tptau #time constant of add. fast temperatur sensor [s]
0.01
!lateral #spatial separation only for lateral wind component (T) only or
    total (F)
T
!drctn #direction of H2O/CO2 measurement [degree] against N
348.
!drctn_CH4  #direction of CH4 measurement [degree] against N
0
```

```
!liu_correct␣#Schotanus/Liu␣correction
F

!wpl_correct␣#WPL␣correction
F

#---------------------------------------------------------------
############################␣QA/QC␣###################################
!stat␣#Perform␣stationarity␣test␣␣(Foken␣et␣al.,␣2012)
T
!itc␣#Test␣on␣developed␣turbulent␣conditions␣with␣integral␣turbulence␣
   characteristics
T
#␣coefficients␣for␣sigma_u/u*␣parameterizations␣according␣to␣Rannik␣et␣al.␣
   (2003)␣or␣Biermann␣(2008)
!within_canopy_u␣#␣a_i,␣alpha_i,␣beta_i,␣gamma_i
2.01,8.97,1.37,0.29
#␣coefficients␣for␣sigma_w/u*␣parameterizations␣according␣to␣Rannik␣et␣al.␣
   (2003)␣or␣Biermann␣(2008)
!within_canopy_w␣#␣a_i,␣alpha_i,␣beta_i,␣gamma_i
1.13,0.9,1.2,-0.63

#Check␣for␣interdependence␣of␣quality␣flags␣due␣to␣corrections:␣ustar␣>␣LvE
   ␣and␣HTs/HTp␣>␣NEE␣(Mauder␣et␣al.,␣2013)
!chk_interdependence
T

#Check␣for␣w-offset␣(Mauder␣et␣al.,␣2013)
!chk_wind
T

#Quality␣Flags
#(1)after␣Foken␣et␣al.␣2004␣(1-9)␣or
#(2)after␣Rebmann␣et␣al.␣2004␣(2)␣for␣CARBOEUROPE␣(1-5)␣or
#(3)according␣the␣scheme␣found␣on␣the␣1st␣CARBOEUROPE␣IP␣Meeting␣in␣Spoleto
   ␣(Mauder␣et␣al.,␣2013)␣(0-2)
!howto_combine
3

#Use␣ITC␣of␣temperature␣for␣the␣sensible␣heat␣flux␣flag,␣only␣applies␣for␣!
   howto_combine␣=␣1␣or␣2
#if␣!howto_combine␣=␣3,␣the␣ITC␣of␣temperature␣is␣not␣used␣anyways
!use_itc_T
F
```

```
#------------------------------------------------------------------
############################ Footprint ################################
#Perform footprint analysis according to Kormann and Meixner (2001)
!footprint
F
#File name of input file with landuse information, required for footprint
    analysis, in ESRI compatible ASCII grid (*.asc)
#The target landuse has to be labelled as '1'; a second target landuse can
    be labelled as '2'
!map_name
'fendt_extended.asc'
#Sensor location in UTM coordinate system [REAL]
!m_easting
654210.060
!m_northing
5299781.402

!footprint_out #output of footprint distribution as ESRI compatible ASCII
    grid (*.asc)
F
#------------------------------------------------------------------
############################ output ###################################
#time information in filename
!timeinfo
T
#append result to existing file
!append
F
!ogive_on
F
!spectra_on
F
!stor_flux
F
!3rd_moments
F
```

Listing A.2: Parameter file for the Sonic anemometer at 4 meters

```
# parameter.vbp
#
# The new Turbulence Knight (TK3) reads all input parameters from this file
    .
# TK3 may also be controlled by editing this file.
#
# Lines beginning with '!' serve as label for parameters to be read in the
    next line
# Lines beginning with '#' serve as comments and will be ignored
# Blank lines will be ignored as well
# Parameters shall be given with an explanation in the line above for
    better reading of this Input-File
#
#-------------------------------------------
# Path of input data
!path_in
'C:\TK3_11\Sonic3\in\'
# Path of working directory
!path_work
'C:\TK3_11\Sonic3\work\'
# Path of output data
!path_out
'C:\TK3_11\Sonic3\out\'

# who did calculations
!author
'Andreas Froyland'
# Project Name
!project
Adventdalen4m

!header_info
F
#####################  site and device data  ####################
# sonic type (CSAT3,USA-1,Solent-HS,Solent-R3,Solent-R2,ATI-K,NUW,YOUNG)
!sonic_type
'CSAT3'

# H2O/CO2 instrument type (LI-7500,KH20,LI-6262,LI-7000,LI-7200,EC150,EC155
    ,LGR,NONE)
!h2o_type
'NONE'

# CH4 instrument type (LI-7700,LGR,Aerodyne,NONE)
!ch4_type
'NONE'
```

```
# hd: measuring height of the device in m (for each measuring complex), (
    REAL)
# hc: canopy height below the device in m (for each measuring complex), (
    REAL)
# wd: wind direction or orientation of u-component of the device in deg. (
    REAL)
# height above sea level (REAL)
!dev_data
4.06, 0, 230, 12.06

# latitude(REAL,INTEGER,INTEGER)
!latitude
78, 12, 08


# Start of processing period (day of year, hour, second) and end-time (
    integer,integer,real)
!start
45,1400,0.00
###45,1400, 0.00

# End of processing period (day of year, hour, second) and end-time (
    integer,integer,real)
!end
94,0834,20.95
### 94,0834,20.95
### 71 is the missing day

# Year of measurements (calculations are only possible within one calender
    year)
!year
2014

# minutes in binary files (REAL)
!t_interval
30

# if binary files exist, type T (LOGICAL)
!load_binary
F
######################## INPUT DATA FILE
    ###################################
#Set true T if the original Campbell logger files are split into hourly
    portions using the program HourlySplitData;
#the input file name will then automatically be generated starting with the
    letter "B"
```

```
!HourlySplitData
F

#name␣of␣first␣data␣file␣(all␣other␣files␣will␣be␣found␣by␣nTK2␣according␣
    to␣the␣given␣time␣window)
!data%file_name
'TOA5_7687_Flux_20140214.dat'


#Input␣file␣format␣('ASCIIcsv','SLT')
!input_file_format
'ASCIIcsv'

#number␣of␣records,␣total␣number␣of␣columns␣in␣input␣file,␣including␣time␣
    stamps␣(INTEGER)
!number_of_records
7

#Format␣of␣time␣stamp
#1␣=␣CR23x,␣e.g.␣254,1030,30.44
#2␣=␣TOA5,␣e.g.␣"2005-09-11␣10:30:30.44"
#3␣=␣LabView,␣e.g.␣254,10:30:30.44
!time_format
2

#Start␣column␣of␣each␣channels␣in␣input␣files,␣if␣not␣associated␣enter␣'0'
!column
␣␣␣␣␣␣␣0,␣␣␣␣␣␣␣␣␣␣1,␣3,␣4,␣5,␣␣6,␣␣␣␣7␣,␣␣0␣,␣␣0␣,␣␣0␣␣,␣0␣,␣␣0,␣␣␣␣␣␣0,␣␣
    ␣␣␣0,␣␣␣␣0␣,␣␣␣␣0,␣␣␣0,␣␣0␣,␣␣␣␣0,␣0
#log_num,␣time_stamp,␣u,␣v,␣w,␣Ts,diagCS,␣co2,␣h2o,diagLI,␣Tp,␣o3,␣incl_x,␣
    incl_y,␣LI_p,␣LI_T,␣CH4,␣N2O,␣HMP_T,HMP_RH

!Aerodyne_file
F
!data_Aero%file_name
'140821_000000.str'

#Units␣of␣channels␣in␣input␣data␣file,␣if␣not␣associated␣enter␣'0'
!unit_wind␣('m s-1','cm s-1')
'm s-1'
!unit_Ts␣('degC','K')
'degC'
!unit_co2␣('mV','mmol m-3','umol mol-1','mg m-3')
'mg m-3'
!unit_h2o␣('mV','g m-3','mmol mol-1','mmol m-3')
'g m-3'
!unit_Tp␣('R R0-1','degC','K')
```

```
0
!unit_o3␣('µg m-3','ppb')
0
!unit_LI_p␣('kPa','hPa')
'kPa'
!unit_LI_T␣('degC')
0
!unit_CH4␣('umol mol-1','nmol mol-1','umol m-3')
0
!unit_N2O␣('nmol mol-1')
0
!unit_HMP_T␣('degC')
degC
!unit_HMP_RH␣('%','kPa')
%

#consistency␣limits,␣in␣same␣units␣as␣in␣input␣file
!input%log_num␣#Logger␣program␣ID␣number,␣e.g.␣for␣CR23X
0,0
!input%day␣#Day␣of␣year
1,366
!input%hour␣#Daily␣time
0,2400
!input%second␣#Seconds
0.0,60.0
!input%u␣#Wind␣u
-50.0,50.0
!input%v␣#Wind␣v
-50.0,50.0
!input%w␣#Wind␣w
-10.0,10.0
!input%Ts␣#Sonic␣temperature
-50.0,30.0
!input%diagCS␣#CSAT␣error␣code,␣usually␣counts␣up␣from␣0␣to␣63;␣set␣0,0␣if␣
   not␣associated,␣IMPORTANT!
0,63
!input%co2␣#CO2
0,2000
!input%h2o␣#H2O
0,35
!input%Tp␣#Platinum␣temperature
0.,0.
!input%o3␣#Ozone
0,0
!input%diagLI␣#diagnostic␣Licor
240,251
!input%incl_x␣#Inclinometer␣x-axis
```

```
0,0
!input%incl_y␣#Inclinometer␣y-axis
0,0
!input%LI_p␣␣␣#pressure␣Licor
80,110
!input%LI_T␣␣#temperature␣Licor
0,0
!input%CH4␣␣␣#methane
0,0
!input%N2O␣␣␣#nitrous␣oxide
0,0.
!input%HMP_T␣␣#reference␣temperature
-20,50
!input%HMP_RH␣␣#reference␣humidity
0,100


#Fixed␣time␣delays␣of␣channels␣in␣input␣data␣file␣[seconds]
!lag
0.0,0.0,0.0,0.0,0.2,0.2,0.0,0.0,␣␣␣0.2,␣␣␣0.0,␣␣␣0.0,0.2␣,0.0␣,0.0,0.0,␣0.0
   ␣,␣0.0
#u␣,␣v␣,␣w␣,␣Ts,co2,h2o,␣Tp,␣o3,diagLI,incl_x,incl_y,LI_p,LI_T,CH4,N2O,
   HMP_T,HMP_RH

!lag_Aerodyne
4.,4.
#CH4,N2O

#Parameters␣are␣required␣to␣create␣an␣equidistant␣time␣scale
#TK2␣will␣search␣for␣the␣data␣line␣in␣input␣file␣that␣matches␣the␣given␣
   time␣stamp␣best
#desired␣time␣interval␣or␣measure␣interval␣in␣sec␣(REAL)
#minimal␣time␣interval␣in␣sonic␣data␣file:␣very␣important␣(REAL
!calc_data
0.051,0.049

#What␣is␣missing␣value,␣what␣is␣the␣code␣for␣missing␣values␣in␣input␣file
!NaN
-9999


#What␣to␣do␣with␣missing␣values
#0␣=␣insert␣NaN␣␣(recommended␣for␣flux␣calculations)
#1␣=␣take␣last␣value␣␣(recommended␣for␣spectral␣calculations,␣including␣
   errors)
#2␣=␣linear␣interpolation
!mv_option
```

```
1

#Missing␣values␣at␣the␣beginning␣of␣blocks␣will␣be␣ignored(F)␣or␣replaced(T
    )
!fill_up_missing_values_at_begin
T

##␣Calibration␣data␣#################
#left␣hand␣coordinate␣system␣(e.g.␣USA-1,Solent-R2):
!lefthand
F
#Head␣Correction␣for␣METEK␣USA-1:␣(0,1,3)
!HC
0
#Licor␣CO2:␣0V␣and␣5V␣equal␣[mmol/m?]␣if␣LI-7500␣in␣mV,␣or␣[ummol␣mol-1]␣if
    ␣LI-7000/LI-6262␣in␣mV
!calib_data%co2
0.,␣1.

#Licor␣H2O:␣0V␣and␣5V␣equal␣[mmol/m?]␣if␣LI-7500␣in␣mV,␣or␣[mmmol␣mol-1]␣if
    ␣LI-7000/LI-6262␣in␣mV
!calib_data%h2o
0.,1.
!calib_data%pt150
17.5,100.,146.84,0.00366
!calib_data%kh20
0.00,␣0.0000,␣␣0.0000,␣-0.0450

!apply_spike_test␣#Apply␣MAD␣spike␣test␣(Mauder␣et␣al.,␣2013)
T
#values␣exceeding␣median+-'7'*std␣equivalent␣are␣spikes
3.5

####################␣REFERENCE␣FILE␣################################
#Reference␣option?
#0␣=␣no␣reference␣measurements␣for␣pressure,␣temperature␣and␣humidity
#1␣=␣reference␣measurements␣in␣same␣data␣file␣as␣turbulent␣data␣(e.g.␣from␣
    HMP45)
#2␣=␣reference␣measurements␣in␣second␣data␣file␣(e.g.␣A6__M001.csv)
!ref_option
0

#consistency␣limits
#Temperatur␣reference␣(degC)
!input%temp
0.,50.
#Humidity␣reference␣(g/m3)
```

```
!input%hum
0.,50.
#Pressure reference (hPa)
!input%pressure
800.,1100.

#-----------------------------------------------------------------
############################ Trouble Shooting
    ################################
!ascii #ASCII Output of raw data(T/F),with flags (T) or without (F)
F,F

!invalid_data
T

################## Calculation parameters ##########################
!load_statistics #files with Covariances already exist?
F
!calc_data%t_interval1 # Calculation time intervals in minutes
30
!calc_data%bad_max # maximum allowed number of missing/bad values in
    averaging interval in % (REAL)
1
#format of the covariance output file
#0 = LITFASS-2003 standard exchange format
#1 = Mikrometeo with Sonic Nvalue (incl. wind direction, <w'e'>)
#2 = Mikrometeo and detailed Nmiss
#5 = Mikrometeo with Sonic Nvalue plus MBR psychrometers
#6 = Mikrometeo and detailed Nmiss, incl. N2O
#7 = like 2 plus random errors   (allows for error calculation)
#8 = like 7, plus CH4, and N2O   (allows for processing CH4 and N2O data)
!format_cov
0

!errors #calculate random errors and instrumental noise (Mauder et al.,
    2013)
T

!x_max #perform cross correlation to maximise covariances of additional
    sensors with w
F
!combine #combine short-term moments for longer time periods(T/F), only
    useful if no high-frequency data are available
F
!calc_data%t_interval2 #short-term averaging interval [min]
5
!calc_data%t_interval3 #Interval between two subsequent averaging intervals
```

```
    ,␣only␣applies␣if␣combine␣=␣T,␣else␣enter␣'0'
0

#-------------------------------------------------------------------
####################␣Correction␣of␣Fluxes␣#################################
!planar_correct␣#Planar␣fit␣method␣(Wilczak␣et␣al.,2001)
T
!read_pf␣#read(T)␣or␣calculate(F)␣coefficients␣of␣multiple␣regression
F
!bk␣#b-coefficients,␣default␣0.,0.,0.␣means␣no␣tilt␣correction,␣only␣
    rotation␣into␣mean␣wind
0.,0.,0.
!mean_wind␣#perform␣rotation␣into␣mean␣wind␣direction
T
!scalar_fluxes␣#transformation␣of␣scalar␣fluxes
T
!double_rotation␣#apply␣the␣double␣rotation␣method␣(T/F),␣should␣only␣be␣
    applied␣if␣!planar_correct␣=␣F
F

!tanner_correct␣#Tanner␣oxygen␣Correction
F

!moore_correct␣#Moore␣correction
F
!sa␣#sensor␣separation␣w␣-␣a␣[m]
0.30
!sc␣#sensor␣separation␣w␣-␣CO2␣[m]
0.30
!n0␣#cut-off␣frequency␣for␣CO2,␣H2O,␣CH4,␣N2O␣[Hz]
20,20,20,20
!sTp␣#sensor␣separation␣w␣-␣Tp␣[m]
0.01
!sn2o␣␣#sensor␣separation␣w␣-␣N2O␣[m]
0.01
!sch4␣␣#sensor␣separation␣w␣-␣CH4␣[m]
0.01
!Tptau␣#time␣constant␣of␣add.␣fast␣temperatur␣sensor␣[s]
0.01
!lateral␣#spatial␣separation␣only␣for␣lateral␣wind␣component(T)␣only␣or␣
    total␣(F)
T
!drctn␣#direction␣of␣H2O/CO2␣measurement␣[degree]␣against␣N
348.
!drctn_CH4␣␣#direction␣of␣CH4␣measurement␣[degree]␣against␣N
0
```

```
!liu_correct␣#Schotanus/Liu␣correction
F

!wpl_correct␣#WPL␣correction
F

#-------------------------------------------------------------------
##############################␣QA/QC␣###################################
!stat␣#Perform␣stationarity␣test␣␣(Foken␣et␣al.,␣2012)
T
!itc␣#Test␣on␣developed␣turbulent␣conditions␣with␣integral␣turbulence␣
    characteristics
T
#␣coefficients␣for␣sigma_u/u*␣parameterizations␣according␣to␣Rannik␣et␣al.␣
    (2003)␣or␣Biermann␣(2008)
!within_canopy_u␣#␣a_i,␣alpha_i,␣beta_i,␣gamma_i
2.01,8.97,1.37,0.29
#␣coefficients␣for␣sigma_w/u*␣parameterizations␣according␣to␣Rannik␣et␣al.␣
    (2003)␣or␣Biermann␣(2008)
!within_canopy_w␣#␣a_i,␣alpha_i,␣beta_i,␣gamma_i
1.13,0.9,1.2,-0.63

#Check␣for␣interdependence␣of␣quality␣flags␣due␣to␣corrections:␣ustar␣>␣LvE
    ␣and␣HTs/HTp␣>␣NEE␣(Mauder␣et␣al.,␣2013)
!chk_interdependence
T

#Check␣for␣w-offset␣(Mauder␣et␣al.,␣2013)
!chk_wind
T

#Quality␣Flags
#(1)after␣Foken␣et␣al.␣2004␣(1-9)␣or
#(2)after␣Rebmann␣et␣al.␣2004␣(2)␣for␣CARBOEUROPE␣(1-5)␣or
#(3)according␣the␣scheme␣found␣on␣the␣1st␣CARBOEUROPE␣IP␣Meeting␣in␣Spoleto
    ␣(Mauder␣et␣al.,␣2013)␣(0-2)
!howto_combine
3

#Use␣ITC␣of␣temperature␣for␣the␣sensible␣heat␣flux␣flag,␣only␣applies␣for␣!
    howto_combine␣=␣1␣or␣2
#if␣!howto_combine␣=␣3,␣the␣ITC␣of␣temperature␣is␣not␣used␣anyways
!use_itc_T
F


#-------------------------------------------------------------------
```

```
############################ Footprint ##############################
#Perform footprint analysis according to Kormann and Meixner (2001)
!footprint
F
#File name of input file with landuse information, required for footprint
    analysis, in ESRI compatible ASCII grid (*.asc)
#The target landuse has to be labelled as '1'; a second target landuse can
    be labelled as '2'
!map_name
'fendt_extended.asc'
#Sensor location in UTM coordinate system [REAL]
!m_easting
654210.060
!m_northing
5299781.402

!footprint_out #output of footprint distribution as ESRI compatible ASCII
    grid (*.asc)
F
#-----------------------------------------------------------------------
############################ output ################################
#time information in filename
!timeinfo
T
#append result to existing file
!append
F
!ogive_on
F
!spectra_on
F
!stor_flux
F
!3rd_moments
F
```

Bibliography

Atlaskin, E., and T. Vihma, Evaluation of NWP results for wintertime nocturnal boundary-layer temperatures over Europe and Finland, *Quarterly Journal of the Royal Meteorological Society*, *138*(667), 1440–1451, doi:10.1002/qj.1885, 2012.

Campbell Scientific, *CS100 Barometric Pressure Sensor*, Campbell Scientific, Inc., 2010a.

Campbell Scientific, *RM Young's Wind Monitor Series*, Campbell Scientific ,Inc., 2010b.

Campbell Scientific, *CNR1 Net Radiometer*, Campbell Scientific, Inc., 2011.

Campbell Scientific, *CSAT3 Three Dimensional Sonic Anemometer*, Campbell Scientific, Inc., 2015.

Derbyshire, S. â., Nieuwstadt's stable boundary layer revisited, *Quarterly Journal of the Royal Meteorological Society*, *116*, 127–158, 1990.

Eigenmann, R., et al., Surface energy balance and turbulence network during the Convective and Orographically-induced Precipitation Study (COPS), *Quarterly Journal of the Royal Meteorological Society*, *137*(SUPPL. 1), 57–69, doi:10.1002/qj.704, 2011.

Esau, I., and S. Zilitinkevich, On the role of the planetary boundary layer depth in the climate system, *Advances in Science & Research*, *4*, 63–69, doi:10.5194/asr-4-63-2010, 2010.

Foken, T., *Micrometeorology*, 306 pp., Springer-Verlag Berlin Heidelberg, 2008.

Foken, T., and B. Wichura, Tools for quality assessment of surface-based flux measurements, *Agricultural and Forest Meteorology*, *78*(1-2), 83–105, doi:10.1016/0168-1923(95)02248-1, 1996.

Foken, T., G. Skeib, and S. H. Richter, Dependence of the integral turbulence characteristics on the stability of stratification and their use for Doppler-Sodar measurements, *Z.Meteorol.*, *41*(June), 311–315, 1991.

Foken, T., L. Leuning, S. R. Oncley, M. Mauder, and M. Aubine, Corrections and Data Quality Control, in *M. Aubinet et al. (eds.), Eddy Covariance: A Practical Guide to Measurement and Data Analysis*, chap. 4, pp. 85–131, Springer Atmospheric Sciences, Dordrecht, Heidelberg, London, New York, doi:10.1007/978-94-007-2351-14, 2012.

Galperin, B., S. Sukoriansky, and P. S. Anderson, On the critical Richardson number in stably stratified turbulence, *Atmospheric Science Letters*, *8*, 65–69, doi:10.1002/asl.153, 2007.

Göckede, M., et al., Quality control of CarboEurope flux data - Part 1: Coupling footprint analyses with flux data quality assessment to evaluate sites in forest ecosystems, *Biogeosciences*, *5*(2), 433–450, doi:10.5194/bg-5-433-2008, 2008.

Grachev, A. A., C. W. Fairall, P. O. G. Persson, E. L. Andreas, and P. S. Guest, Stable boundary-layer scaling regimes: The SHEBA data, *Boundary-Layer Meteorology*, *116*(2), 201–235, doi:10.1007/s10546-004-2729-0, 2005.

Grachev, A. A., E. L. Andreas, C. W. Fairall, P. S. Guest, and P. O. G. Persson, The Critical Richardson Number and Limits of Applicability of Local Similarity Theory in the Stable Boundary Layer, *Boundary-Layer Meteorology*, *147*(1), 51–82, doi:10.1007/s10546-012-9771-0, 2013.

Grachev, A. A., et al., SHEBA flux-profile relationships in the stable atmospheric boundary layer, *Boundary-Layer Meteorology*, *124*, 315–333, doi:10.1007/s10546-007-9177-6, 2007.

Högström, U., Non-Dimensional Wind and Temperature Profiles in the Atmospheric Surface Layer: A Re-Evaluation, in *Topics in Micrometeorology. A Festschrift for Arch Dyer*, edited by B. B. Hicks, pp. 55–78, Springer Netherlands, Dordrecht, doi:10.1007/978-94-009-2935-7_6, 1988.

Högström, U., Review of Some Basic Characteristics of the Atmospheric Surface Layer, *Boundary-Layer Meteorology*, *78*, 215–246, 1996.

Holtslag, A. A. M., et al., Stable Atmospheric Boundary Layers and Diurnal Cycles: Challenges for Weather and Climate Models, *Bulletin of the American Meteorological Society*, *94*(11), 1691–1706, doi:10.1175/BAMS-D-11-00187.1, 2013.

Jakobson, L., T. Vihma, E. Jakobson, T. Palo, A. Männik, and J. Jaagus, Low-level jet characteristics over the Arctic Ocean in spring and summer, *Atmospheric Chemistry and Physics*, *13*(21), 11,089–11,099, doi:10.5194/acp-13-11089-2013, 2013.

Lange, T. D., Radiation measurement system UNIS version, *Tech. Rep. May*, Geophysical Institue, University of Bergen, 2011.

Liu, H., G. Peters, and T. Foken, New Equations For Sonic Temperature Variance And Buoyancy Heat Flux With An Omnidirectional Sonic Anemometer, *Boundary-Layer Meteorology*, *100*(3), 459–468, 2001.

Mahrt, L., J. Sun, W. Blumen, T. Delany, and S. Oncley, Nocturnal boundary-layer regimes, *Boundary-Layer Meteorology*, *88*, 255–278, 1998.

Mäkiranta, E., T. Vihma, A. Sjöblom, and E.-M. Tastula, Observations and Modelling of the Atmospheric Boundary Layer Over Sea-Ice in a Svalbard Fjord, *Boundary-Layer Meteorology*, *140*, 105–123, doi:10.1007/s10546-011-9609-1, 2011.

Malhi, Y. S., The significance of the dual solutions for heat fluxes measured by the temperature fluctuation method in stable conditions, *Boundary-Layer Meteorology*, *75*, 389–396, 1995.

Mauder, M., and T. Foken, Documentation and instruction manual of the eddy covariance software package TK3 (update), *Universität Bayreuth, Abt. Mikrometeorol.*, *3*, 2015.

Mauder, M., T. Foken, R. Clement, J. A. Elbers, W. Eugster, T. Grünwald, B. Heusinkveld, and O. Kolle, Quality control of CarboEurope flux data - Part 2: Inter-comparison of eddy-covariance software, *Biogeosciences*, *5*(2), 451–462, doi:10.5194/bg-5-451-2008, 2008.

Mauder, M., M. Cuntz, C. Drüe, A. Graf, C. Rebmann, H. P. Schmid, M. Schmidt, and R. Steinbrecher, A strategy for quality and uncertainty assessment of long-term eddy-covariance measurements, *Agricultural and Forest Meteorology*, *169*, 122–135, doi:10.1016/j.agrformet.2012.09.006, 2013.

Mayer, S., M. O. Jonassen, A. Sandvik, and J. Reuder, Profiling the Arctic Stable Boundary Layer in Advent Valley, Svalbard: Measurements and Simulations, *Boundary-Layer Meteorology*, *143*, 507–526, doi:10.1007/s10546-012-9709-6, 2012.

Monin, A. S., and A. M. Obukhov, Basic laws of turbulent mixing in the surface layer of the atmosphere, *Tr. Akad. Nauk SSSR Geophiz. Inst.*, *24*(19604), 163–187, 1954.

Nieuwstadt, F. T. M., The Turbulent Structure of the Stable, Nocturnal Boundary Layer, *Journal of the Atmospheric Sciences*, *41*(14), 2202–2216, doi:10.1175/1520-0469(1984)041<2202:TTSOTS>2.0.CO;2, 1984.

Persson, P. O. G., Measurements near the Atmospheric Surface Flux Group tower at SHEBA: Near-surface conditions and surface energy budget, *Journal of Geophysical Research*, *107*(C10), 8045, doi:10.1029/2000JC000705, 2002.

Rotronic, *HygroClip*, Rotronic, 2 ed., 2002.

Sodemann, H., and T. Foken, Empirical evaluation of an extended similarity theory for the stably stratified atmospheric surface layer, *Quarterly Journal of the Royal Meteorological Society*, *130*, 2665–2671, doi:10.1256/qj.03.88, 2004.

Song, T., Y. Sun, and Y. Wang, Multilevel measurements of fluxes and turbulence over an urban landscape in Beijing, *Tellus B*, *65*(20421), doi:10.3402/tellusb.v65i0.20421, 2013.

Sorbjan, Z., and A. A. Grachev, An Evaluation of the Flux-Gradient Relationship in the Stable Boundary Layer, *Boundary-Layer Meteorology*, *135*(3), 385–405, doi:10.1007/s10546-010-9482-3, 2010.

Stull, R. B., *An Introduction to Boundary Layer Meteorology*, 1 ed., Springer Netherlands, Dordrecht, doi:10.1007/978-94-009-3027-8, 1988.

Svensson, N., and A. Rutgersson, Stable atmospheric conditions over the Baltic Sea: model evaluation and climatology, *Boreal Enviroment Research*, *6095*(21), 387–404, 2016.

Tastula, E.-M., B. Galperin, S. Sukoriansky, A. Luhar, and P. Anderson, The importance of surface layer parameterization in modeling of stable atmospheric boundary layers, *Atmospheric Science Letters*, *16*(1), 83–88, doi:10.1002/asl2.525, 2015.

Thomas, C., and T. Foken, Re-evaluation of Integral Turbulence Characteristics and their Parameterisations, in *15th Symposium on Boundary Layers and Turbulence*, pp. 129–132, American Meteorological Socciety, Wageningen, The Netherlands, 2002.

Tjernström, M., et al., Modelling the Arctic boundary layer: An evaluation of six ARCMIP regional-scale models using data from the SHEBA project, *Boundary-Layer Meteorology*, *117*(2004), 337–381, doi:10.1007/s10546-004-7954-z, 2005.

Uttal, T., et al., Surface Heat Budget of the Arctic Ocean, *Bulletin of the American Meteorological Society*, *83*(2), 255–275, doi:10.1175/1520-0477(2002)083<0255:SHBOTA>2.3.CO;2, 2002.

Vihma, T., et al., Advances in understanding and parameterization of small-scale physical processes in the marine Arctic climate system: a review, *Atmospheric Chemistry and Physics Discussions*, *14*(17), 9403–9450, doi:10.5194/acp-14-9403-2014, 2014.

Walesby, K. T., and R. J. Beare, Parameterizing the Antarctic stable boundary layer: synthesising models and observations, *Quarterly Journal of the Royal Meteorological Society*, doi:10.1002/qj.2830, 2016.

Wilczak, J., S. Oncley, and S. Stage, Sonic anemometer tilt correction algorithms, *Boundary-Layer Meteorology*, *99*(1), 127–150, doi:10.1023/A:1018966204465, 2001.

Young, *Young Model 41342*, R.M. Young Company, 2004.

Zilitinkevich, S., and P. Calanca, An extended similarity theory for the stably stratified atmospheric surface layer, *Quarterly Journal of the Royal Meteorological Society*, *126*(126), 1913–1923, doi:10.1256/smsqj.56617, 2000.

Zilitinkevich, S. S., and I. N. Esau, Similarity theory and calculation of turbulent fluxes at the surface for the stably stratified atmospheric boundary layer, *Boundary-Layer Meteorology*, *125*(2), 193–205, doi:10.1007/s10546-007-9187-4, 2007.

Zilitinkevich, S. S., I. Esau, N. Kleeorin, I. Rogachevskii, R. D. Kouznetsov, and A. M. Obukhov, On the Velocity Gradient in Stably Stratified Sheared Flows. Part 1: Asymptotic Analysis and Applications, *Boundary-Layer Meteorology*, *135*, 505–511, doi:10.1007/s10546-010-9488-x, 2010.